UNIVERSIDADE
BEIRA INTERIOR

Numerical Analysis of the Ebro River Meander Flow Field, Upstream of the Bridge Pavilion

(versão final após defesa)

César Augusto Vaz Santos

Dissertação para obtenção do Grau de Mestre em
Engenharia Civil
(ciclo de estudos integrado)

Orientadora: Prof. Doutora Cristina Maria Sena Fael
Coorientador: Prof. Doutor Juan Pedro Martín-Vide

Dezembro de 2022

Declaração de Integridade

Eu, César Augusto Vaz Santos, que abaixo assino, estudante com o número de inscrição 34474 de/o curso de Engenharia Civil da Faculdade de Engenharia, declaro ter desenvolvido o presente trabalho e elaborado o presente texto em total consonância com o **Código de Integridades da Universidade da Beira Interior**.

Mais concretamente afirmo não ter incorrido em qualquer das variedades de Fraude Académica, e que aqui declaro conhecer, que em particular atendi à exigida referenciação de frases, extratos, imagens e outras formas de trabalho intelectual, e assumindo assim na íntegra as responsabilidades da autoria.

Universidade da Beira Interior, Covilhã 14 / 12 / 2022

(assinatura conforme Cartão de Cidadão ou preferencialmente assinatura digital no documento original se naquele mesmo formato)

Dedicatória

À minha Mãe...

Agradecimentos

Começo por agradecer aos meus orientadores por todo o apoio prestado. Agradeço, em especial, à Professora Doutora Cristina Maria Sena Fael, que ao longo dos últimos anos me acompanhou no desenvolvimento deste e de outros trabalhos, durante os bons e maus momentos, mas que, sobretudo, sempre foi exigente comigo e, por conseguinte, fez-me ser exigente comigo próprio. Obrigado!

Agradeço à equipa do Projecto ASHES, pelas discussões enriquecedoras e por criarem um ambiente onde me senti à vontade para fazer perguntas e continuar sempre a aprender. Obrigado!

Aos meus amigos, que têm estado sempre presentes, mesmo não estando perto. Que continuemos a partilhar momentos por muitos mais anos. Na linha da amizade, não poderia deixar de agradeçer a um grande amigo, que se tornou como um irmão para mim e me conhece como ninguém. Esta dissertação não seria a mesma coisa sem as nossas discussões sobre CFD. Obrigado!

Agradeço à minha família incrível, por me transmitir os valores de união e atenciosidade que se traduzem em fortes relações familiares, apesar de sermos uma familia grande. Às minhas tias, em especial, à Deolinda, pelo carinho e apoio incondicional. Obrigado!

Por fim, não por ser menos importante, mas porque sei que não há palavras para fazer jus à mãe que tenho. Presente, batalhadora, mão firme quando foi preciso, mas carinhosa também. O que sou hoje, tenho ela a agradecer. Muito obrigado!

Resumo

A construção de infraestruturas com componentes dentro de cursos de água sempre foi um desafio para os engenheiros. No caso de pilares de pontes em leitos aluvionares, em particular, são constantes as preocupações sobre erosões localizadas e alterações morfológicas induzidas pelo pilar. Com os recentes avanços computacionais, as ferramentas numéricas têm desempenhado um papel fundamental na compreensão da hidrodinâmica dos escoamentos. Assim, este trabalho faz uso do programa ANSYS Fluent para analisar o campo de escoamentos do meandro do Rio Ebro e os efeitos causados pelo pilar complexo do Pavilhão-Ponte de Zaragoza. A sua forma, dimensão e posicionamento enviesado em relação ao escoamento fazem com que a interação estrutura-escoamento tenha um comportamento único. Inicialmente, um modelo invíscido é aplicado para uma compreensão qualitativa do campo de escoamento, ao longo de um domínio de $5000\,\mathrm{m}$ de comprimento, $200\,\mathrm{m}$ de largura e com uma profundidade máxima de escoamento de $8\,\mathrm{m}$. Para este caso, a topografia real do meandro é considerada. A seguir, um modelo reduzido à escala 1/62.5 é utilizado para modelar a turbulência, considerando uma geometria representativa do meandro. As equações RANS são resolvidas com recurso ao modelo de turbulência Standard $k-\varepsilon$. Após a validação numérica, os resultados obtidos são comparados com trabalhos experimentais e de campo. Os resultados mostram que ao longo da curva, as velocidades mais elevadas estão concentradas no extradorso. No vão direito da ponte, verifica-se um aumento da velocidade de 50%. No vão esquerdo, o aumento da velocidade não é tão pronunciado. A jusante do pilar, é detetada a esteira e o par de vórtices também está presente. A energia cinética turbulenta exibe valores de pico próximos do leito, sob o vão direito do pilar. As tensões de corte no leito mostram um aumento generalizado de pelo menos o dobro na zona próxima ao pilar e, um aumento de 5 vezes no lado direito. Também são detetadas correntes secundárias ao longo da curva, com intensidades de até 12% do valor da velocidade longitudinal na secção correspondente a 115°. A seguir, a sua intensidade diminui em direção à saída da curva. Ao longo do troço reto, o escoamento secundário decai rapidamente, até ser substituído por um fluxo de baixa intensidade em direção à margem interna.

Palavras-chave

Dinâmica de Fluidos Computacional; Escoamento Secundário; Erosão Localizada; Pilar Complexo.

Abstract

The construction of infrastructures inside water channels has always been challenging for engineers. Concerning bridge piers, concerns about local scour and morphology changes induced by the pier are ever-present. With the recent computational advancements, numerical tools have played a fundamental role in understanding flow hydrodynamics. As such, this work resorts to the ANSYS Fluent software to analyse the Ebro River meander flow field and the effects caused by the large and complex pier of the Zaragoza Bridge Pavilion. The shape, size, and skewed position of the pier relative to the flow make the flow-structure interaction unique to this case. Initially, an inviscid model is used to provide qualitative insight into the flow field over the $5000\,\mathrm{m}$ long and $200\,\mathrm{m}$ wide domain, with a maximum water depth of $8\,\mathrm{m}$. For this case, the natural bed topography is considered. Afterwards, a 1/62.5 scaled model is used for the turbulence modelling, considering a representative geometry of the meander. The RANS equations are solved using the Standard $k-\varepsilon$ turbulence model. The results are compared with previous experimental work and field surveys after the numerical validation. The results show that the core of high velocities along the bend is directed toward the outer bank. Under the right span of the bridge, a velocity increase of up to 50% is seen. On the left side, the velocity increase is less pronounced. Downstream of the pier, the wake region is detected, and the vortex pair is also present. Turbulence kinetic energy results show peak values close to the bed, under the right span of the pier. Bed shear stress results show a twofold general increase in the vicinity of the pier and a five times increase on the right side. Secondary currents are detected along the bend, with intensities up to 12% of the streamwise velocity at the 115° section. Then, the intensity starts to decrease toward the bend exit. The secondary current rapidly decays along the straight reach until a weak flux toward the inner bank replaces it.

Keywords

Computational Fluid Dynamics; Secondary Flow; Local Scour; Complex Pier

Contents

List of Figures

List of Tables

Lista de Acrónimos

CFD	Computational Fluid Dynamics
EWT	Enhanced Wall Treatment
FVM	Finite Volume Method
LES	Large Eddy Simulation
RANS	Reynolds Averaged Navier-Stokes
RSM	Root Mean Square
RSM	Reynolds Stress Model
SSL	Separated Shear Layer
2D	Two-dimensional
3D	Three-dimensional

Notation

A	Cross-section area
$\overrightarrow{A}$	Surface area vector
$\overrightarrow{A}_f$	Area vector of face f
B	Channel width
$C_{1\varepsilon}, C_{2\varepsilon}, C_{3\varepsilon}, C_\mu, C_1, C_2, E$	Empirical constants
D	Hydraulic diameter
De	Dean number
d	Pier diameter
f	Cell face
f_{VS}	Vortex-shedding frequency
Fr	Froude number
G_b	Generation of k due to buoyancy
G_k	Generation of k due to mean velocity gradients
g	Gravitational acceleration
H	Flow depth
k	Turbulence kinetic energy
k_P	Turbulence kinetic energy at the wall-adjacent cell centroid
L	Characteristic length
N_{faces}	Number of faces enclosing a given cell
P	Cell centroid
p	Pressure
P_h	Wetted perimeter
Q	Flow rate
R	Curvature radius
Re	Reynolds number
$\overrightarrow{r}$	Vector from the upstream cell centroid to the face centroid
S	Modulus of the mean rate-of-strain tensor
S_k, S_ε	User-defined source terms
St	Strouhal number
$S\varphi$	Source of φ per unit volume
t	Time
U	Velocity at the inlet section
U_c	Critical entrainment velocity
U_M	Velocity magnitude
U_P	Mean velocity at the wall-adjacent cell centroid

u	Streamwise velocity
u_τ	Friction velocity
$u^+, U*$	Non-dimensional velocity
V	Cell volume
v	Spanwise velocity
$\overrightarrow{v}$	Velocity vector
Y_M	Contribution of the fluctuating dilatation to the overall dissipation rate
y_P	Distance from the centroid of the wall-adjacent cell, to the wall
y^+, y^*	Dimensionless wall distance
w	Vertical velocity
x	Longitudinal spatial coordinate
y	Spanwise spatial coordinate
$\alpha_k, \alpha_\varepsilon$	Turbulent Prandtl numbers
Γ_φ	Diffusion coefficient for
δ_{ij}	Kronecker delta
ε	Turbulence kinetic energy rate of dissipation
ε_P	ε at wall-adjacent cells
κ	von Kármán constant
μ	Dynamic viscosity
μ_t	Turbulent viscosity
ν	Kinematic viscosity
ρ	Fluid density
φ	General scalar
$\bar{\varphi}$	Mean value of a general scalar
φ'	Oscillation of a general scalar
φ_f	Value of φ convected through face f
τ_M	Shear stress magnitude
τ_w	Wall shear stress
τ_0	Mean bed shear stress at the inlet
ω_z	Vertical vorticity

Chapter 1

Introduction

"Scientists study the world as it is; engineers create the world that has never been."

Theodore von Kármán

In this chapter the motivation and objectives of the current dissertation are described. Additionally, a brief introduction to the interest of this particular case-study is presented. In the outline subsection, the structure of the dissertation is summarised.

1.1 Motivation and Objectives

Experimental studies have been, for many decades, the pillars on which Civil Engineering rests and, in river hydraulics, were imperative for understanding the complex phenomena intrinsic to the matter. However, in recent years, the reliance on numerical studies has become increasingly more common owing to computational capacity advancements. This is because numerical studies offer relatively quick and reliable results without requiring expensive laboratory setups. Nevertheless, numerical simulations have their limitations, the main one being the computational demand. Indeed, that is the main reason for the scarce number of real-scale numerical simulation studies, although more recent numerical methods have been developed to overcome the said limitation.

Regarding river hydraulics research, understanding the hydro-geomorphological processes characteristic of the phenomena involved has always been a central issue. Not only is the comprehension of these mechanisms academically interesting, but it is also of great practical importance. Its interest is not only restricted to hydrodynamic concepts but also to the need to meet engineering and ecological requirements.

Given that when dealing with alluvial channels, the natural erosion process poses a genuine concern, whether because there is a need to ensure the integrity of infrastructures with components inside the channel or because of the problems that excessive sediment transport may cause downstream, it becomes clear just how important the study of this phenomenon is. As such, experimental and numerical studies are used. There is, however, an understandable gap in real-scale hydrodynamic numerical studies of river meanders.

When studying meandering river hydrodynamics, the role of secondary flow, transversal circulation currents, is of unquestionable importance in understanding the underlying mechanisms involved. As such, numerous in-depth laboratory-scale studies have been done on the role and implications of the secondary flow in meanders.

For this dissertation, the Ebro river meander is studied, particularly the section located in Zaragoza, Spain. The section of interest is depicted in Figure 1.1.

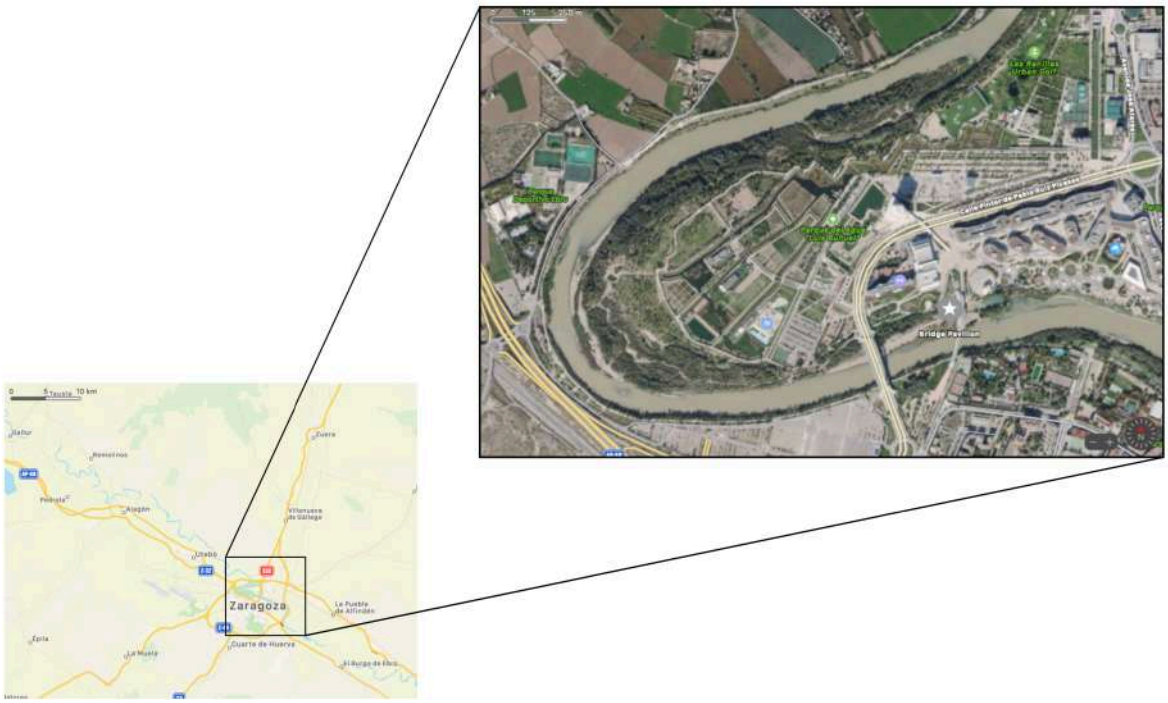

Figure 1.1: Ranillas meander and location of the Bridge Pavilion, Zaragoza. [1]

The study of this section of the meander is not without its reasons. The Bridge Pavilion, whose construction was concluded in 2008, is both a footbridge and an exhibition pavilion. Seeing that the bridge has its pier inside the meander, this obstacle is expected to influence the flow field.

Initially, the pier was built on top of a small, probably, ephemeral natural island that had formed in the channel (Figure 1.2). This indicates that the accretion of material at that particular location is a natural tendency of the meander. However, its size and form directly result from the meander's flow conditions, and the pier is expected to play a significant role in the dynamics of the channel. Also, note how one side of the stream is more obstructed than the other (Figure 1.2). It was observed that the difference between the two sides became more pronounced over the years, especially due to a big flood event in 2015 [2]. Remediation operations have been attempted to stabilise the section near the pier, including dredging the left side and modifying the alluvial bar (Figure 1.3). It remains unclear, however, if this imbalance results from the pier or the proximity of the meander's curvature. Perhaps, both. Thus, this dissertation intends to shed some light on the meander's hydrodynamics with the anal-

ysis of the flow field, hoping to detect the well-known secondary flow phenomenon. Some parameters of interest include the velocity, pressure and shear fields. The area around the pier will deserve particular care in order to understand the degree to which the meander's dynamics might affect the bridge's structural integrity.

Figure 1.2: Alluvial bar prior to the construction of the pier [3].

Furthermore, a series of simplifications are explored to reduce the computational demand without calling into question the reliability and quality of the results. As such, this dissertation relies on an extensive literature review to validate the results obtained here.

Figure 1.3: Alluvial bar around the bridge, after one of the interventions. [4]

1.2 Outline

This dissertation comprises six chapters. In the first one, an introduction to the theme is made, including the motivation and objectives of this work.

The second chapter conducts a thorough literature review on the subjects pertaining to this case study. An initial theoretical framework on meander hydrodynamics and flow around piers is presented, followed by the particularities of the Bridge Pavilion.

Chapter 3 covers concepts of computational fluid dynamics and explains the algorithm used by ANSYS Fluent.

In Chapter 4, the numerical procedure is described, along with the methodology used to approach the problem.

In the fifth chapter, the results are presented and discussed. A comparison is made between the simulated cases and the results from the literature.

Finally, in Chapter 6, the conclusions of this work are presented, and suggestions for future works are made.

This dissertation also includes an Appendix with the published articles resulting from the present investigation work.

Chapter 2

Literature Review

"Who questions much, shall learn much, and retain much."

Francis Bacon

This chapter analyses the state of the art in meander hydrodynamics. Furthermore, based on previous works, a breakdown of the particularities of the Zaragoza Bridge Pavilion is presented. At the end of the chapter, a compilation of the most relevant studies is shown.

2.1 Theoretical Framework

It is widely known that rivers are dynamic systems. When exposed to natural dynamic hydrologic conditions, they readjust themselves with respect to size and shape to reach an equilibrium state by an ongoing natural process of erosion, and deposition [5, 6]. As for the river banks, it is known that they are subject to erosion, particularly in sharp bend meanders, owing to the high bed shear stresses at the outer bank [7]. These mechanisms lead to the formation of deposition and scour zones, which results in the natural meander migration, that may negatively impact structures like bridge piers and abutments and, of course, bank stability [8]. As a result, one of the most critical tasks in river engineering is the prediction of momentum and sediment transport in curved channels.

In bends, the combination of centrifugal forces and pressure gradients results in transverse circulations, also known as secondary flow. This three-dimensional helical flow plays an important influence on flow behaviour, and river morphology [7, 9]. Despite being known for over a century, there is still much to understand about this transverse circulation phenomenon, partly owing to the complexity of accounting for turbulence effects [10].

Furthermore, the meander's geometry itself has a significant influence on the flow behaviour, given that parameters such as the curvature ratio (ratio between the bend radius, R, and the channel width, B) and the aspect ratio (ratio between the channel width and the water depth, H) affect the intensity of the transverse circulation cells and thus, have a direct impact on the meander's hydrodynamics and morphodynamics [11]. A feedback effect becomes evident: the secondary flow enables erosion and sedimentation processes and alters

the meander's geometry. At the same time, this readjusted geometry matches a distinct flow pattern. Further information on the influence of the meander's geometry is summarised in Table 2.3. Additionally, in Table 2.2 and Table 2.4 a compilation of two other research works is showcased. These were selected because the experimental setup, methods, and results are relevant to this dissertation.

Consider Figure 2.1, which represents the relevant processes in meander bends. Two circulation cells can be seen: a larger one, occupying most of the cross-section, hereafter designated as the centre-region cell, and a smaller counter-rotating circulation cell, hereafter designated as the outer-bank cell. For simplification purposes, we shall consider the cylindrical coordinate system shown in Figure 2.1, where the curvilinear s-axis points downstream along the channel axis, the transversal n-axis points toward the inner bank, and the vertical z-axis is pointing upward from the horizontal (s, n)-plane. Also, v is the velocity component in the considered direction.

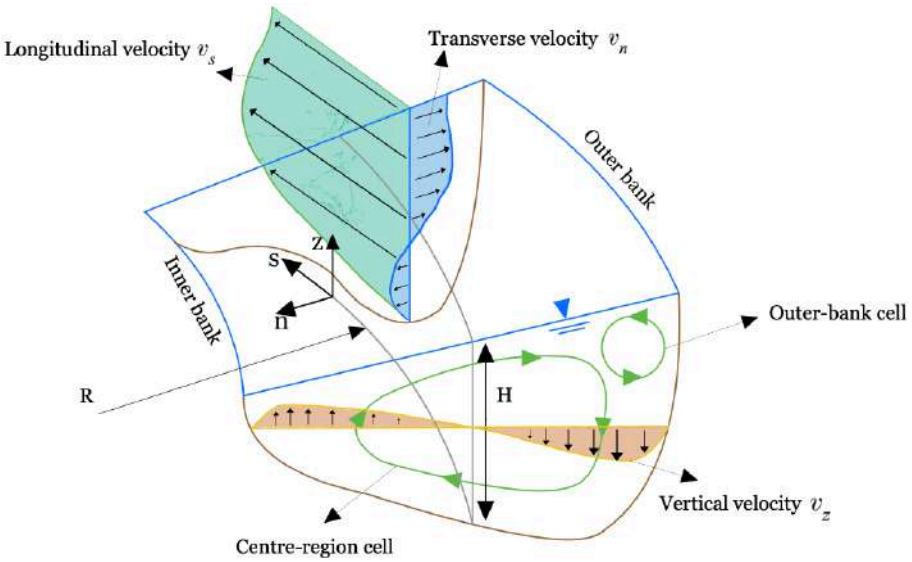

Figure 2.1: Conceptual sketch of the relevant processes in meander bends. Adapted from [7].

The cross-stream motion (v_n, v_z), is expressed by the transverse and vertical momentum equations. The local imbalance between the cross-stream pressure gradient and centrifugal force causes the centre-region cell to form. This process starts with the deformation of the v_s-profile, resulting from the advective momentum transport by the centre-region cell. This causes a decrease in the velocity in the upper part of the water column and an increase in the lower part. The consequence of this deformation is the reduction of the vertical gradient of the centrifugal force, allowing the cross-stream circulation to take place [7, 12].

Before discussing the outer-region cell, we must first introduce the Dean number, De, defined as the product between the Reynolds number, Re, and the square root of (B/R). Its significance, from a physical standpoint, is the ratio between the centrifugal effect and the dissipative effect, owing to viscosity. It was found that an increase of De to a critical value

causes the outer-bank cell to form [13, 14, 15]. This might explain why the outer-bank cell is often more observable in sharp bend channels rather than in mild bend ones.

When considering the case of curved turbulent flow, which is relevant in the context of this dissertation, de Vriend [16] concluded that the isolated actions of the centrifugal force and turbulence could not explain the outer-bank cell. As such, per Christensen et al. [17], it was concluded that the turbulent vorticity generation plays a just as important role as the centrifugal force; hence, it is the combination of both that contributes to the generation of the outer-bank cell.

The importance of the outer-bank cell comes from the fact that the centre-region cell redistributes the stream-wise velocity, causing it to increase toward the outer bank. The outer-bank cell counters this velocity progression and keeps it away from the outer bank by making the core of the maximum velocity to remain at a certain distance from the bank [5]. Thus, it creates a buffer layer that protects the outer bank from the influence of the centre-region cell, which in turn helps minimise the outer bank erosion [11, 18]. Additionally, numerous parameters are involved in meandering rivers' hydrodynamic mechanisms. As such, to better understand these phenomena, we must first introduce these parameters. The Reynolds number translates the ratio between the inertial and viscous forces and is given by

$$Re = \frac{\rho U L}{\mu} \quad \textbf{(2.1)}$$

The cross-stream motion (v_n, v_z), is expressed by the transverse and vertical momentum equations. The local imbalance between the cross-stream pressure gradient and centrifugal force causes the centre-region cell to form. This process starts with the deformation of the v_s-profile, resulting from the advective momentum transport by the centre-region cell. This causes a decrease in the velocity in the upper part of the water column and an increase in the lower part. The consequence of this deformation is the reduction of the vertical gradient of the centrifugal force, allowing the cross-stream circulation to take place [7, 12].

Before discussing the outer-region cell, we must first introduce the Dean number, De, defined as the product between the Reynolds number, Re, and the square root of (B/R). Its significance, from a physical standpoint, is the ratio between the centrifugal effect and the dissipative effect, owing to viscosity. It was found that an increase of De to a critical value causes the outer-bank cell to form [13, 14, 15]. This might explain why the outer-bank cell is often more observable in sharp bend channels rather than in mild bend ones.

When considering the case of curved turbulent flow, which is relevant in the context of this dissertation, de Vriend [16] concluded that the isolated actions of the centrifugal force and turbulence could not explain the outer-bank cell. As such, per Christensen et al. [17], it was concluded that the turbulent vorticity generation plays a just as important role as the centrifugal force; hence, it is the combination of both that contributes to the generation of

the outer-bank cell.

The importance of the outer-bank cell comes from the fact that the centre-region cell redistributes the stream-wise velocity, causing it to increase toward the outer bank. The outer-bank cell counters this velocity progression and keeps it away from the outer bank by making the core of the maximum velocity remain at a certain distance from the bank [5]. Thus, it creates a buffer layer that protects the outer bank from the influence of the centre-region cell, which in turn helps minimise the outer bank erosion [11, 18]. Additionally, numerous parameters are involved in meandering rivers' hydrodynamic mechanisms. As such, to better understand these phenomena, we must first introduce these parameters. The Reynolds number translates the ratio between the inertial and viscous forces and is given by

where ρ is the fluid density, U is the approach velocity, μ is the fluid's dynamic viscosity, and L is a characteristic length, which in this case, is defined as the water depth. Another important dimensionless parameter is the Froude number which is defined by the ratio of the flow inertia to the external force field, given by

$$Fr = \frac{U}{\sqrt{gL}} \quad (2.2)$$

where g is the gravitational acceleration. As referred by Leeder & Bridges [19], the Froude number influences flow separation. As such, its importance becomes evident as flow separation results in shear layers that may induce scouring.

Regarding the meander's geometry, the curvature ratio is noteworthy since it reflects the sharpness of the bend and hence, the weight of the centrifugal force, which according to Blanckaert & de Vriend [7], is the driving mechanism for the cross-stream circulation. Furthermore, in sharp bend meanders, the stream-wise velocities are advected towards the outer bank at a higher rate than in mild bends. As a result, the cross-stream circulations are stronger, and the outer bank erosion is higher. As for the aspect ratio, it was found that an increase in its value tends to break down the centre-region cell into two clockwise-rotating cells [11].

In short, the flow structure in natural rivers results from complex interactions of numerous variables. It is influenced by topographic steering effects (resulting in secondary currents), large-scale irregularities of the banks [20], and large-scale bed roughness [21]. Figure 2.2 illustrates the flow separation effect.

Flow separation is affected by parameters such as the curvature ratio and the Froude number. Typically, in tight bends, the inertial forces are much more dominant than the viscous forces. Upon encountering the bend, the flow cannot remain "attached" to the inner bank and, thus, separates. This creates a region of a faster stream at the outer bank and lower velocities in the inner bank. Per Sukhodolov et al. [22], when lateral velocity gradients are large enough

to allow for a notable exchange of momentum and mass, lateral shear layers evolve at the interfaces between fast and slow currents.

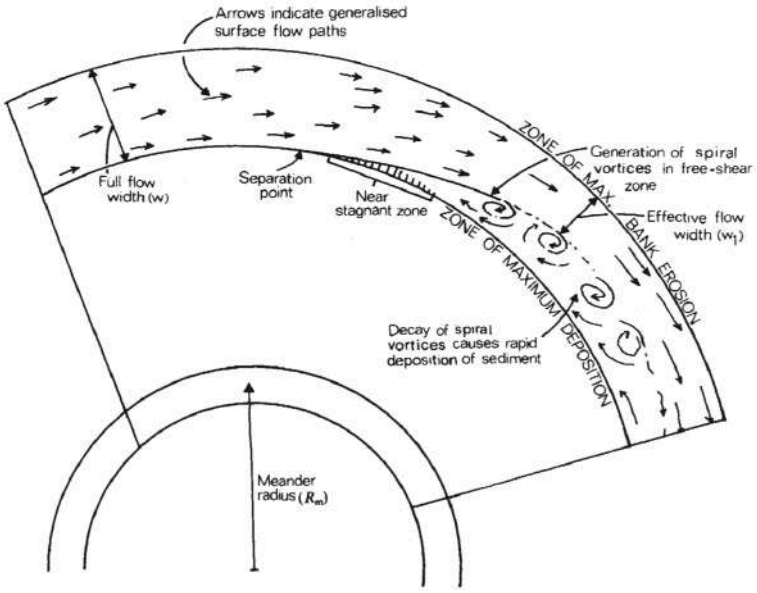

Figure 2.2: Conceptual sketch of the main characteristics of separated flows [19].

According to Leeder & Bridges [19], the separation zone seen in Figure 2.2 is highly unstable, where, periodically, the boundary between the main downstream flow and this more erratic fluid deforms into spiral vortices. These vortices gradually decay as the separation zone merges back with the main downstream flow at the inflection point. The decay and inward movement of the associated eddies is the reason behind the high sediment deposition in inner banks. Moreover, flow separation reduces the effective width of the downstream flow, which causes the high-velocity flow to be directed towards the outer bank and, thus, increases the bank erosion effect [8].

The formation of these eddies was also reported by Constantinescu et al. [23]. They found that strong Separated Shear Layers (SSLs) form between these eddies and the main flow. This results in the production of high shear-driven turbulence within the shear layer that causes the formation and shedding of energetic turbulent eddies downstream of the SSLs, as seen in Figure 2.3. Occasionally, the eddies separating from SSLs may approach the high-velocity flow at the outer bank and induce the ejection of patches of high-vorticity fluid, thus resulting in significant pressure fluctuations, intensification of the outer wall shear stress and the convection of large-scale eddies downstream-wise.

This means that bank stability should not be analysed only by the mean values of the bed shear stress since instantaneous values might play a relevant role. Thus, analysing the pressure Root Mean Square (RMS) fluctuations and the values of instantaneous bed shear stress is fundamental for bank stability since they can significantly increase the erosion potential of the turbulent flow [23]. Finally, in Figure 2.4, the typical meander migration pattern is depicted.

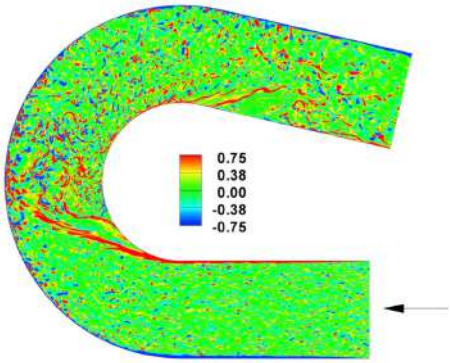

Figure 2.3: Normalised vertical vorticity, $\omega_z D/U$, at the free surface in one of the instantaneous flow fields [23].

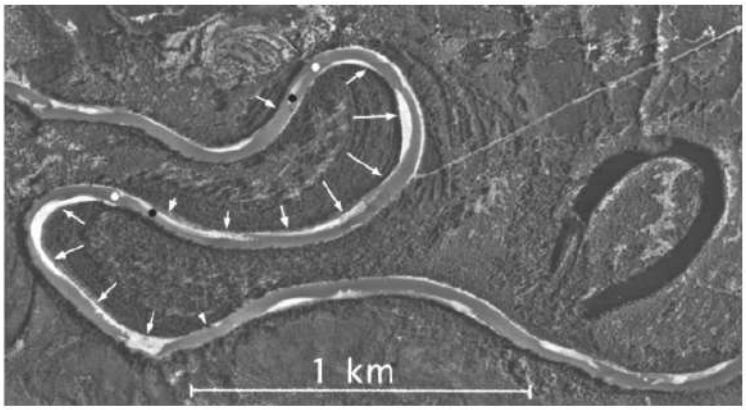

Figure 2.4: Typical meander migration pattern [24].

As previously mentioned, the curvature of the meander greatly influences the local flow field. Given the flow's high inertia, the effects of the curvature are expected to be felt even downstream of the bend. Edwards & Smith [24] analysed three natural meanders employing an explicit equation of motion. They found that the bend can influence the flow's local velocity profile between 100 and 1000 meters downstream. Apart from the meander's downstream migration, a lateral migration also occurs due to the previously mentioned sediment erosion and deposition process. Over time the meander stretches and shrinks, which eventually culminates in the formation of an oxbow lake. This perpetual cycle describes the natural meander migration observed in nature.

As mentioned, meanders are subject to a natural scour process resulting from cross-circulation currents. However, erosion can also be induced by the presence of obstacles within the channel, which is termed local scour. Since many structures, like bridges, can have piers founded in watercourses, understanding the flow-structure interactions is of the utmost importance since many bridge failures result from foundation scouring, which can be aggravated under flood conditions [2].

The presence of a pier acts as an obstacle to the flow, causing a change to the velocity field around it. Four main features (depicted in Figure 2.5) can be identified in the flow pattern around a pier: the downflow upstream of the pier, the horseshoe vortex at the base of the

pier, the surface roller ahead of the pier and the wake vortices downstream of the pier.

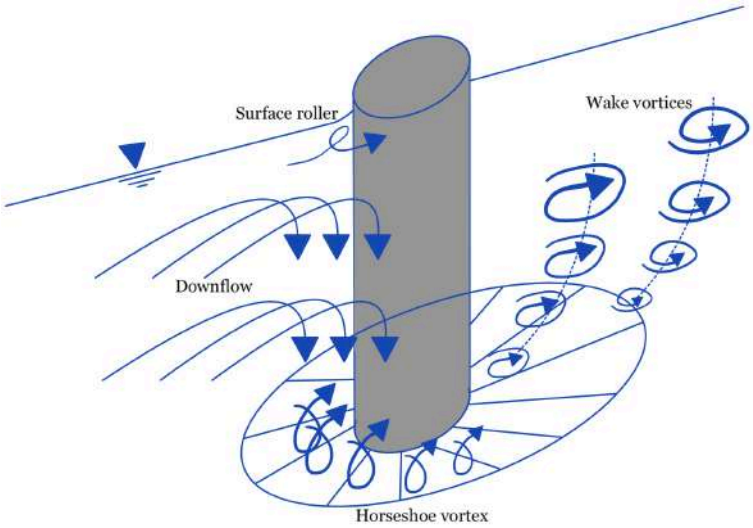

Figure 2.5: Flow pattern around a cylindrical pier. Adapted from [25].

As the flow approaches the pier, the velocity decreases and takes a zero value at its upstream face. The resulting stagnation zone at this location induces a pressure increase, ΔP, given by

$$\Delta P = \frac{\rho\,[u(z)]^2}{2} \quad (2.3)$$

where $u(z)$ is the flow velocity at depth z from the channel bed. Seeing that velocities decrease with depth, the ensuing pressure gradient generates a downward flow that is partially deflected upstream when it collides with the bed [26, 27]. Some authors consider that the downflow impinging on the bed, which acts as a vertical jet, is responsible for starting the erosion process [26, 28]. In the resulting scour hole, local avalanches of sediment into the erosion zone ensure that the slope of the scour hole stays at the repose angle of the sediment as it develops. An interesting phenomenon occurs in the near-bead upstream region of the pier. As the approaching flow reaches the rim of the scour hole, it separates. The combination of the separated flow and the deflected downflow generates the so-called horseshoe vortex. Per Raudikivi [27], although effective in transporting sediments away from the scour hole, the horseshoe vortex is a consequence of scouring and not its cause. As it circumvents the pier, the horseshoe vortex is stretched. It dissipates further downstream, contributing to the ambient turbulence of the flow [28].

A few key concepts must be introduced to further discuss the flow behaviour around the pier. When studying fluid dynamics, there is a fundamental distinction concerning the fluid: ideal fluids, which are inviscid and incompressible, and real fluids. In ideal fluids, there are only normal forces (pressure) between adjacent fluid layers. In spite of disregarding tangential forces (shear stresses), ideal flows give a satisfactory description of real flows in many cases,

especially for very high Reynolds number flows [29, 30]. However, the theory of ideal fluids is not suitable for problems where determining the drag of a body is required, as it predicts that the body will experience no forces as a consequence of the fluid motion. In real fluid flows, in addition to normal forces, there are also tangential forces both between fluid layers and between the fluid and the walls, the latter resulting from the imposition of the no-slip condition. These tangential forces are a result of the viscosity of the fluid. Note that the use of ideal fluids is widespread, given that considerable simplifications of the equations of motion are reached through this assumption [29].

As mentioned, the Reynolds number translates the ratio between the inertial and the viscous forces. Practically speaking, most flows are high Reynolds number flows, i.e., flows where viscosity effects are negligible. However, due to the no-slip condition at boundaries, a singularity is introduced into the flow equations: the velocity must transition from a finite value close to the wall to the value of zero directly at the wall. According to Prandtl [31], this transition occurs in a thin layer close to the wall, in the so-called boundary layer. As a result of the boundary layer concept, at a high Reynolds number, the flow can be divided into two regions: in the first one, the bulk flow region, viscosity effects are negligible, and, as such, the flow behaves as an inviscid one; and the second region, the very thin boundary layer at the wall, where the viscosity must be considered. Note that the boundary layer can be a laminar or a turbulent boundary layer, depending on flow conditions [29]. Finally, in order to explain the boundary layer separation phenomenon, consider Figure 2.6.

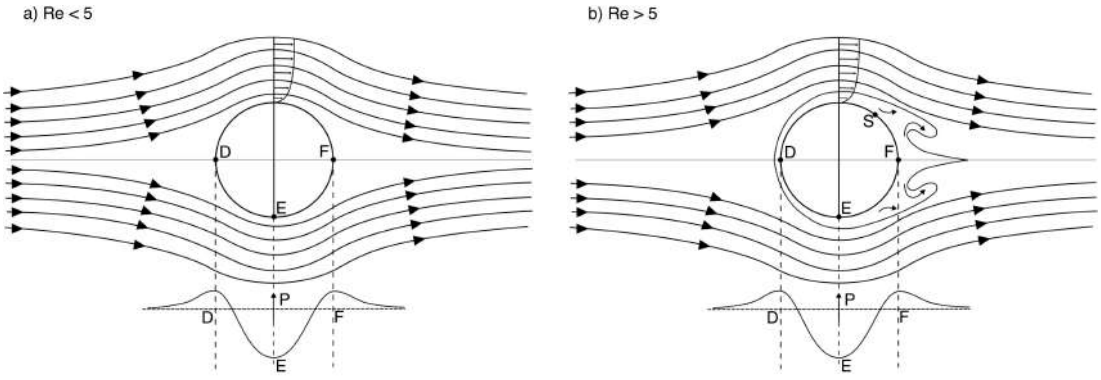

Figure 2.6: Boundary layer separation around a cylinder. Adapted from [29].

Consider a fluid particle in the outer flow (outside of the boundary layer), moving from D to E. Here, the previously mentioned pressure increase that occurs in D is converted into kinetic energy, causing the fluid particles to accelerate between D and E, with a consequential pressure decrease. Then, from E to F, the kinetic energy is transformed into pressure, resulting in an increase in pressure. However, for a particle close to the wall within the boundary layer, a great deal of its kinetic energy is lost owing to the strong frictional forces in this layer, meaning that such a particle cannot describe the path of the increasing pressure from E to F. The particle comes to a halt and is then pushed backwards by the pressure distribution of the outer flow. As a result of the back-flow, a vortex forms at the back of the cylinder and eventually separates from the body and moves downstream [29, 31]. This vortex's characteristics

depend on the Reynolds number, as shown in Table 2.1.

Table 2.1: Flow regimes at a cylinder as a function of the Reynolds number. Adapted from [29] and [32].

Reynolds number	**Flow regime**	**Flow pattern**	**Observations**
< 5	Steady, no separation.	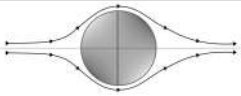	The flow does not separate, thus, there is no wake.
5 < Re < 40	Vortex pairs in wake.	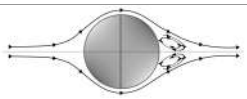	A symmetric separation takes place, resulting in a pair of vortices. Their size increases with Re.
40 < Re < 150	Onset of Karman vortex street.		Alternating shedding of clockwise and counterclockwise rotating vortices. At these values of Re, the vortex street is laminar.
150 < Re < 300	Transition to the turbulent vortex street.	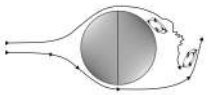	The transition to the turbulent vortex street takes place, marking the onset of the first three-dimensional instabilities.
300 < Re < 3×10^5	Fully turbulent wake.		The vortex street is completely turbulent, whereas the boundary layer on the cylinder remains laminar.
3×10^5 < Re < 3×10^6	Transition to the turbulent boundary layer.	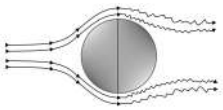	The vortex street becomes narrower and loses coherence, and the boundary layer transitions to turbulent.
> 3×10^6	The vortex street is reestablished.	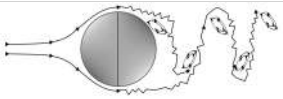	Turbulent separation takes place and a fully turbulent vortex street is reestablished.

As mentioned, the boundary layer can be a laminar one or a turbulent one. As such, the separation phenomena for each type of boundary layer have distinct characteristics. For turbulent boundary layers, the separation point is moved further downstream because of the turbulent mixing motion, which energises the turbulent boundary layer and, thus, delays separation. Moreover, after the boundary layer has separated and left the body, it forms the wake. Sometimes the shedding of regular patterned clockwise and counterclockwise rotating vortices occurs. This is known as the Kármán vortex street. The vortex-shedding frequency, f_{VS}, can be determined by means of the Strouhal number, $St = f_{\mathrm{VS}} \cdot d/U$, where d is the cylinder's diameter. Finally, the occurrence of the separation phenomena also depends on the geometry of the body, as more streamlined bodies are less prone to flow separation [29, 30, 33].

Having introduced the concepts of boundary layer separation and wake vortices, it is easily understandable that the local scour at bridge piers comprises multiple mechanisms. Given their low pressure, the wake vortices rip the bed sediments by a suction effect and carry them downstream [26, 28]. Furthermore, even if the pier is relatively streamlined, its alignment with the flow is directly linked to flow separation. Given that the scour depth is a function of

the pier width normal to the flow, the angle of attack of the pier is an important factor [27]. It becomes clear, then, that the presence of a meander upstream to the pier, which causes a certain deviation of the flow, can significantly influence the scour process at a bridge pier, as has been discussed by Martín-Vide et al. [2].

As mentioned, the pier's shape is also a factor in the scour process. Piers can be divided into simple piers, which have constant width throughout their depth, and complex piers, which include pilled foundations, slab footings and tapered piers. According to Melville [26], a downward-tapering pier induces deeper scouring than a circular pier of the same width. Another critical factor is the pier size. As the size of the pier increases, the larger the scour volume and the longer the time for the scour depth to develop. Other influencing factors in the local scour at bridge piers include sediment size, grading, and flow depth [27].

Seeing that this dissertation analyses the effects of a large pier that stands skewed relative to the straight channel reach where it is located, and given the existence of a meander upstream, a complex interaction between the variables is expected.

2.2 The Zaragoza Bridge Pavilion

Located in Zaragoza (Spain), the Bridge Pavilion was built in 2008 and became a city landmark. The bridge serves as a footbridge and an exhibition pavilion. One of the particularities of this bridge is the dimension of its goblet-like pier, which sits inside the Ranillas meander. For the 500-year return period (flow rate, Q, of $5222\,\mathrm{m^3\,s^{-1}}$), the downward-tapering pier obstructs the flow width at $80\,\mathrm{m}$ out of $240\,\mathrm{m}$ at the water surface and $28\,\mathrm{m}$ out of $170\,\mathrm{m}$ at the bed elevation.

As in any bridge scour prediction process, the use of clear-water conditions (no sediment feed) for scaled models provides reasonably accurate scour estimations [34, 35]. Given that long-term local scour depth at a bridge pier reaches its maximum value when the flow velocity is equal to the critical entrainment velocity, U_c, by selecting the appropriate bed material size, local scour can be maximised. Thus, countermeasures on the safe side can be implemented. This led to the common practice of using clear-water conditions to estimate local scour at bridge piers. However, discrepancies have been found between scour predictions of clear-water models and live-bed models in the case of unusually large and complex piers [36, 37].

In the case of the Bridge Pavilion, a thorough experimental analysis of the local scour was carried out by Martín-Vide et al. [3]. A physical model of the pier at a scale of 1/62.5 was used to evaluate the maximum local scour depth and design a riprap apron as a scour countermeasure. The pier model is shown in figure 2.7. For more details on the experimental study, see [3].

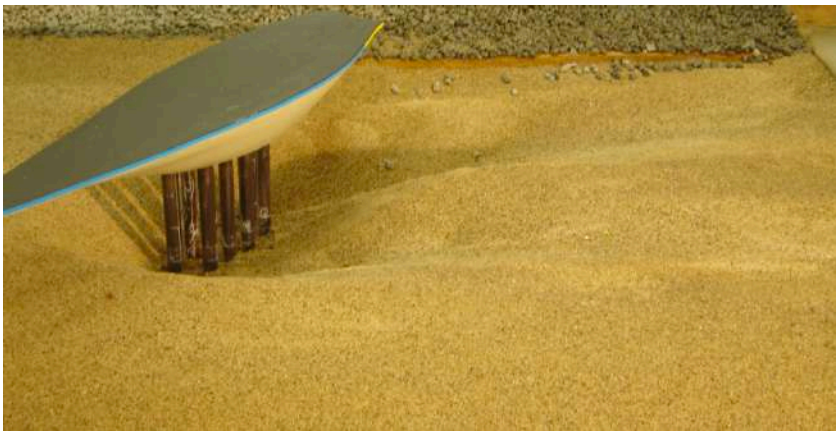

Figure 2.7: Physical model of the Bridge Pavilion's pier [2].

Despite a major flood event that occurred in 2015, the riprap protection held on and prevented local scouring at the pier. However, important morphological changes around the bridge were reported. A significant accumulation of alluvial material on the left span of the bridge was observed, which caused the $3.6\,\mathrm{m}$ deep river arm to become filled. Furthermore, the bar downstream of the pier expanded approximately $75\,\mathrm{m}$ and an $8.5\,\mathrm{m}$ deep scour hole downstream of the right span was discovered in a post-flood survey, as shown in Figure 2.8.

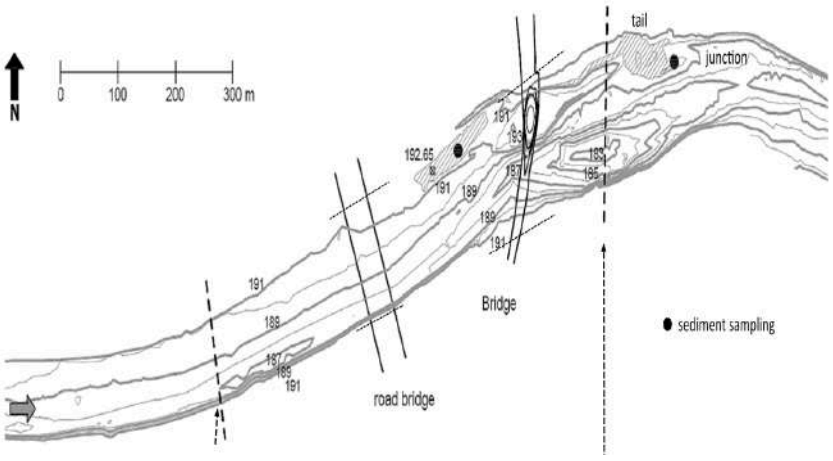

Figure 2.8: Field survey around the bridge, after the 2015 flood [2].

The point made in [2] is that given its size, the pier acts as a bifurcation splitting the flow and sediment load in two. The asymmetrical division of flow rates and sediment load in bifurcations is well-known. Additionally, the presence of the meander upstream introduces secondary currents so that the velocity vector deviates at a certain angle. The bedload material also has a deviation angle, which can be greater than the flow angle at the bed [38], which makes the pier's left side prone to aggradation.

The interaction between all of these factors is complex, as the scouring and aggradation trends appear to sustain each other. There is an increased flow rate to the right arm owing to the aggradation of the left arm, sustaining the scour. In contrast, greater velocities on the

right arm mean lower velocities on the left one, thus, sustaining the aggradation. The system is a delicate one in the sense that any measure to counter the scouring (dredging or filling) would change flow conditions and result in morphology changes elsewhere in the system [2].

Thus, the present work builds on the extensive laboratory and field studies previously done to introduce a numerical perspective on the analysis of the intricate flow dynamics of the Bridge Pavilion, aiming to provide greater insight into the matter.

Table 2.2: Summary 1 - Secondary flow in sharp open-channel bends [7]

Authors: Koen Blanckaert and Huib de Vriend (2004)			
Experiment	Methods	Results	Notes
• $Re = 42000$ • $Fr = 0.36$ • $R = 2m$ • $R/B = 5$ • $R/H = 17.9$ • $B/H = 3.6$	• Experimental: laboratory flume, $0.4m$ wide, $2m$ straight approach and $120°$ bend • Velocity profiles measured with ADVP	• Normalised downstream velocity isolines • Normalised depth-averaged downstream velocity • Normalised unit discharge • Downstream vertical velocity profiles • Normalised downstream vorticity isolines • Normalised turbulent normal and normal shear stresses • Normalised terms in downstream vorticity equations • Normalised kinetic energy fluxes	• Balance between the driving centrifugal term and the dissipating shear stress term in the downstream vorticity equation dominates centre-region cell • Centrifugal force and cross-stream turbulent stresses contribute to the formation of the outer-bank cell

Table 2.3: Summary 2 - Influence of Channel Aspect Ratio and Curvature on Flow, Secondary Circulation, and Bed Shear Stress in a Rectangular Channel Bend [11]

Authors: Shalini Kashyap et al. (2012)			
Experiment	Methods	Results	Notes
• R/B=1.5; 3.0; 5.0; 8.0; 10.0 • B/H=5.0; 6.67; 9.09; 12.50	• Velocity profiles measured with ADV • Numerical: RANS solver with a standard RSM closure; rigid lid assumption Experimental setup to validate numerical results	• Non-dimensional streamwise and cross-section velocity contours and 2D streamlines • Non-dimensional stream-wise unit discharge • Non-dimensional bed shear distributions	• Sharp bends generally have higher peak values of bed shear stresses • In sharper bends, the outer bank cell can be just as expressive as the centre-region cell The aspect ratio influences the location of maximum bed shear stresses Shallower channels tend to originate two clockwise-rotating centre-region cells • Multiple clockwise-rotating streamwise-orientated circulation cells is a characteristic of flow in high curvature bends with $R/B \leq 3$ • Faster decay of circulation past the section at which the peak cross-stream circulation occurs, for higher curvature channels

Table 2.4: Summary 3 - 3D Numerical Modelling of Flow and Sediment Transport in Laboratory Channel Bends [9]

Authors: Ali Khosronejad et al. (2007)			
Experiment	Methods	Results	Notes
• S-shape channel, with identical reverse bends connected by a straight section • Rectangular cross-section, with rigid vertical walls and deformable bed • Bends of 90° and 135° • $Q = 0.023m^3/s$; $U = 0.3m/s$; $R = 1.25m$; $H = 0.15m$	• Based on the finite volume method (FVM) • RANS solved for the flow field properties • Low-Reynolds number $k-\omega$ and standard $k-\varepsilon$ turbulence models • Numerical results validated by comparison between numerical and experimental results of other researches Water surface treated as a rigid lid. • Velocity-pressure coupling: SIMPLE • Experimental setup to validate numerical results	• Downstream velocity profile • Transverse velocity profile • Computed bed topography evolution	• The selected models are reasonably accurate in predicting secondary currents • Numerical methods are accurate in predicting sediment transport and bed topography evolution, with mean error values between 11 and 13%

Chapter 3

Computational Fluid Dynamics

"The machine does not isolate man from the great problems of nature but plunges him more deeply into them."

Antoine de Saint-Exupery

This chapter presents the governing equations and the implemented turbulence model while also covering essential Computational Fluid Dynamics (CFD) concepts. Furthermore, in the last part of this chapter, the numerical model is explained, allowing greater insight into the solver's algorithm.

3.1 Mathematical Model

The governing equations are the pillars on which the entire process of problem modelling is based. For fluid dynamics, the Navier-Stokes equations are the governing equations, which for this dissertation will be solved recurring to ANSYS Fluent. Thus, the mathematical model is presented herein to allow for a better understanding of the software's algorithm.

3.1.1 Governing Equations

The Navier-Stokes equations have long been established as the governing equations concerning fluid dynamics. However, solving the equations for turbulent flows means solving the multiple scales present in the flow, from the largest to the smallest eddies. Thus, accurately modelling turbulence, which is a random three-dimensional phenomenon, can be a demanding process, both from a computational and formulation point of view.

For that matter, and for the case of this dissertation, the Reynolds Averaged Navier-Stokes (RANS) equations are numerically solved to estimate the flow properties. The solution variables in the instantaneous Navier-Stokes equations are considered to be the sum of their mean value (time-averaged or ensemble-averaged) and their fluctuation, as shown bellow

$$\varphi = \bar{\varphi} + \varphi' \quad (3.1)$$

where φ is a flow property, $\bar{\varphi}$ is its mean value, and φ' is its fluctuation. Next, the continuity and RANS equations are presented, written in a Cartesian tensor form. For an incompressible fluid, it follows that the continuity equation is given by

$$\frac{\partial u_i}{\partial x_i} = 0 \quad (3.2)$$

where x_i and u_i are, respectively, the spatial coordinates and the velocity in the i direction. Equation 3.2 can be expanded into

$$\frac{\partial u}{\partial x} + \frac{\partial v}{\partial y} + \frac{\partial w}{\partial z} = 0 \quad (3.3)$$

where u, v and w are the velocity components in the x, y and z directions, respectively. The momentum equation (incompressible fluid) is given by

$$\frac{\partial (u_i)}{\partial t} + \frac{\partial (u_i u_j)}{\partial x_j} = -\frac{1}{\rho}\frac{\partial p}{\partial x_i} + \nu \frac{\partial^2 u_i}{\partial x_j \partial x_j} - \frac{\partial (\overline{u_i' u_j'})}{\partial x_j} + g_i \quad (3.4)$$

where t, p, ν, and g_i are, respectively, the time, pressure, kinematic viscosity, and gravitational acceleration vector. The same expansion process can be applied to the momentum equation. Breaking down equation 3.4, on the left-hand side, the first term corresponds to the temporal term and the second to the convective term. On the right-hand side, the first term is the pressure term, the second is the viscous term (diffusive term), the third is the Reynolds stress term, and the final term represents the gravitational field force.

Naturally, the Reynolds stress term needs to be modelled in order to solve the RANS equations and, typically, the Boussinesq hypothesis, which relates the turbulent stresses to the mean velocity gradients, is applied [39]. In the mentioned hypothesis, the Reynolds stress term is given by

$$-\rho \overline{u_i' u_j'} = \mu_t \left(\frac{\partial u_i}{\partial x_j} + \frac{\partial u_j}{\partial x_i} \right) - \frac{2}{3}\rho k \delta_{ij} \quad (3.5)$$

where μ_t is the turbulent viscosity, k the turbulence kinetic energy and δ_{ij} the Kronecker delta. μ_t and k can be determined recurring to turbulence models.

3.1.2 The Inviscid Approach - Euler Equations

Given that the main challenge that numerical simulations face is the computational demand, which may render the case study unfeasible, simplifications can and must be adopted to reduce the computational time but, of course, without jeopardising the quality of the results. As mentioned, the accurate modelling of turbulence is a demanding process. When concerning small scales, as is the case of laboratory-size studies, this does not pose a decisive factor as simulations can still be done in an acceptable time.

However, when dealing with real-scale studies with notably complex geometries and Reynolds numbers of such magnitude, as is the case of this dissertation, the level of mesh refinement required to credibly model turbulence effects would render the simulation impractical; thus, the inviscid approach. At first, it might seem like an unreasonable assumption, so consider the following

$$\lim_{\mu \to 0} Re = \lim_{\mu \to 0} \frac{\rho U L}{\mu} = \infty \quad (3.6)$$

Evidently, there is no such thing as an infinite Reynolds number. Therefore, what this means is that the inertial forces are much more dominant than the viscous forces. Such an effect can be observed by performing the non-dimensionalisation of the Navier-Stokes equations, recurring to a characteristic length (L, that can be the flow depth, for instance), and thus, be written as

$$\frac{\partial u^*}{\partial t^*} + (u^* \cdot \nabla^*) u^* = -\nabla^* p^* + \frac{1}{Re} \nabla^{*2} u^* + \frac{1}{Fr^2} \cdot \hat{g} \quad (3.7)$$

where u^*, t^*, P^* are the dimensionless variables of velocity, time and pressure, respectively. Note that in equation 3.7, u^* denotes the velocity vector, while the ∇ operator denotes the gradient. The dimensionless variables are obtained according to: $u^* = u/U$, $t^* = tU/L$, $p^* = p/(\rho U^2)$, $\nabla^* = \nabla L$ and $r^* = r/L$. Mind that r^* is not explicitly written in equation 3.7, but it is present inside the gradients, and it refers to the non-dimensional spatial coordinate.

Looking at equation 3.7, it can be noted that as the Reynolds number increases, the viscous term is drawn to zero. Indeed, the deduction of the RANS equation shows that turbulence effects appear to be related to the convective term as opposed to, strictly, the viscous term. This is because the mathematical simplifications to the Navier-Stokes equations in order to obtain the RANS equations cause the Reynolds stresses to originate from the convective term. Furthermore, equation 3.7, designated as the non-dimensionalised Navier-Stokes equation, is of significant importance as it allows for greater insight into the weight of each term in the equation.

Indeed, when considering a real-scale meander, the viscous forces, although important when analysing scouring effects, are not preponderant when evaluating the general mean flow behaviour. However, it is worth mentioning that when using this approach, the values of velocity obtained will naturally be higher than the actual values. This simplification, essential when studying real-scale cases, is very much valid considering that the Reynolds number is of a such high order, as referenced by Bird [40] and White [30]. As such, equation 3.4 can be rewritten for an incompressible flow as

$$\frac{\partial u_i}{\partial t} + (u_i \cdot \nabla) u_i = -\frac{1}{\rho} \nabla P + g_i \quad (3.8)$$

which is typically referred to as the Euler momentum equation.

3.1.3 Turbulence Modelling

A turbulence model is a semi-empirical model with various constants obtained from experimental investigations. The current dissertation uses the common $k-\varepsilon$ turbulence model, which is a two-equation model, to numerically solve the RANS equations. The reason behind a two-equation model selection is that in complex flow fields involving separated flows, unsteadiness and highly irregular geometries, lower order turbulence models, like zero-, half-, or one-equation models, become ineffective [39]. Thus, turbulence models are responsible for calculating variables that allow the modelling of the Reynolds stress tensor.

For the $k-\varepsilon$ turbulence model, partial differential equations are derived for the turbulence kinetic energy (k) and its rate of dissipation (ε). It is one of the most popular turbulence models, with proven accuracy in a wide range of flow conditions, allowing for reliable results in a relatively short amount of time [41]. Nevertheless, given that important turbulence phenomena occur in millimetre scales, while the whole flow domain may extend over several hundred meters, it is understandable that this may instantly render the simulation impracticable.

The $k-\varepsilon$ turbulence model proposes the following equations for the turbulence kinetic energy and the turbulence kinetic energy rate of dissipation, respectively, given by

$$\frac{\partial}{\partial t}(\rho k)+\frac{\partial}{x_i}(\rho k u_i)=\frac{\partial}{\partial x_j}\left[\left(\mu+\frac{\mu_t}{\sigma_k}\right)\frac{\partial k}{\partial x_j}\right]+G_k+G_b-\rho\varepsilon-Y_M+S_k \quad (3.9)$$

and

$$\frac{\partial}{\partial t}(\rho\varepsilon)+\frac{\partial}{\partial x_i}(\rho\varepsilon u_i)=\frac{\partial}{\partial x_j}\left[\left(\mu+\frac{\mu_t}{\sigma_\varepsilon}\right)\frac{\partial \varepsilon}{\partial x_j}\right]+C_{1\varepsilon}\frac{\varepsilon}{k}(G_k+C_{3\varepsilon}G_b)-C_{2\varepsilon}\rho\frac{\varepsilon^2}{k}+S_\varepsilon \quad (3.10)$$

where G_k represents the generation of turbulence kinetic energy due to the mean velocity gradients and is given by

$$G_k=-\rho\overline{u_i'u_j'}\frac{\partial u_j}{\partial x_i} \quad (3.11)$$

G_b is the generation of turbulence kinetic energy due to buoyancy, and Y_M represents the contribution of the fluctuating dilatation in compressible turbulence to the overall dissipation rate. Given the assumption of the Boussinesq hypothesis, the production of turbulence kinetic energy is evaluated as $G_k=\mu_t S^2$, where S is the modulus of the mean rate-of-strain tensor, defined as $S=\sqrt{2S_{ij}S_{ij}}$.

$C_{1\varepsilon}, C_{2\varepsilon}$ and $C_{3\varepsilon}$ are constants, and σ_k and σ_ε are the turbulent Prandtl numbers for k and ε, respectively. $C_{3\varepsilon}$ is disregarded since it only applies to compressible flows. In this model, the constants adopt the following values

$$C_{1\varepsilon}=1.44 \;\;;\;\; C_{2\varepsilon}=1.92 \;\;;\;\; \sigma_k=1.0 \;\;;\;\; \sigma_\varepsilon=1.3$$

These constants were experimentally determined for fundamental turbulent flows and shear flows like boundary layers, mixing layers and jets. Studies show that these constants work fairly well for a wide range of wall-bounded and free-shear flows [41]. S_k and S_ε are user-defined source terms.

The μ_t term shown in equation 3.5 is calculated through k and ε according to the following equation

$$\mu_t = \rho C_\mu \frac{k^2}{\varepsilon} \quad (3.12)$$

where $C_\mu = 0.09$ is a constant. It should be noted that the $k - \varepsilon$ turbulence model is an isotropic turbulence model. As such, it may not detect the counter-rotating outer-bank cell, as it is primarily driven by turbulence anisotropy [42, 23]. In this regard, higher-order turbulence models such as the Reynolds Stress Model (RSM) or Large Eddy Simulation (LES) are much more accurate but, at the same time, are far more computationally demanding.

3.1.4 Wall Treatment

The correct understanding of the boundary layer structure, mainly the y^+ wall distance, is fundamental for the correct modelling of turbulence effects because turbulence models were designed to be employed within certain parameter values, as is the case of the y^+ wall distance. Hence, to ensure the validity of the results, these parameters must be kept within established values [43].

First, consider the commonly defined zones within a turbulent boundary layer, as shown in figure 3.1, where u^+ and y^+ are, respectively, the non-dimensional velocity and space coordinate.

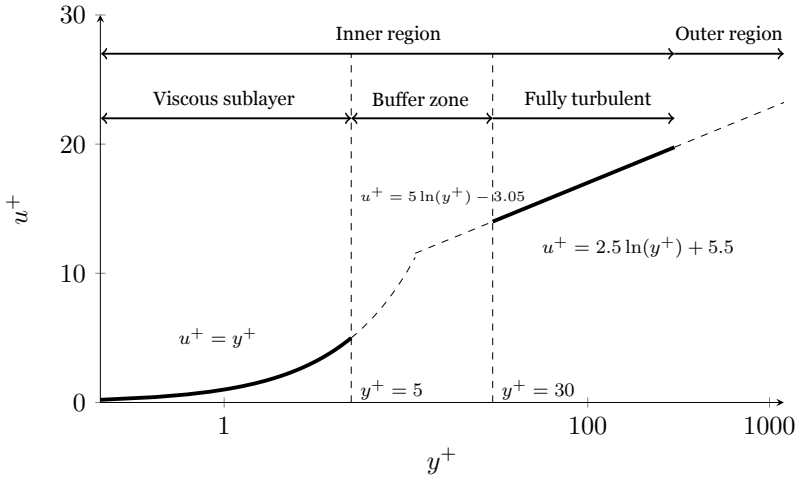

Figure 3.1: Typical non-dimensional velocity profile for a turbulent flow over a flat plate. Adapted from [43].

Analysing Figure 3.1, we can note that the boundary layer is defined by two main regions: the outer and inner zones. In the inner zone, at a very small layer close to the wall, designated as the laminar (or viscous) sublayer, viscous shear is dominant and, in the fully turbulent zone, turbulent shear (terms such as $\overline{u_i' u_j'}$) is dominant. In the buffer zone, a region that connects the two previously mentioned ones, both the viscous and turbulent shear are dominant. In the outer layer, the mean flow properties are dominant.

Given the distinct features of each region, at least two length scales must be associated with the turbulent flow. The first one concerns the laminar sublayer, the very thin region adjacent to the walls where the gradients are large, with a near linear velocity profile. The second one concerns the outer region, where the velocity exhibits a near-constant behaviour with distance from the wall.

If we consider $\overline{u}$ to be the mean velocity (for the outer region), and u_τ to be the velocity scale for the viscous sublayer, through dimensional analysis, the two can be related according to

$$\frac{\partial \overline{u}}{\partial y} = C_1 \frac{u_\tau}{y} \quad (3.13)$$

where C_1 is an experimentally determined constant. As such, the following dimensionless quantities are defined

$$y^+ \equiv \frac{y u_\tau}{\nu} \quad (3.14)$$

$$u^+ \equiv \frac{\overline{u}}{u_\tau} \quad (3.15)$$

that are related through the well-known log-law, given by

$$u^+ = C_1 \ln(y^+) + C_2 \quad (3.16)$$

where C_2 is also an experimentally determined constant. Furthermore, in equation 3.14, u_τ is the friction velocity given by

$$u_\tau = \left(\frac{\tau_w}{\rho} \right)^{\frac{1}{2}} \quad (3.17)$$

and τ_w is the wall shear stress, defined as

$$\tau_w = \mu \left(\frac{\partial u}{\partial y} \right)_w \quad (3.18)$$

As mentioned, near-wall modelling is one of the most problematic areas in turbulence modelling, not only from a computational standpoint but also because an adequate selection of the modelling method is required. Of equal importance is the resolution of the mesh and only the coupling of these two factors allows us to achieve good predictions. However, the

selected model and the mesh resolution are not independent of each other, meaning that the mesh resolution must be such that it matches the selected model's criteria.

Furthermore, it is important to mention that the Standard $k-\varepsilon$ turbulence model selected for this dissertation is not without its limitations. It is essentially a high-Reynolds model, meaning that y^+ must be employed away from solid boundaries. Thus, a wall treatment is required to integrate through the viscous sublayer. Additionally, this model lacks some sensitivity to adverse pressure gradients, and in some conditions, it overestimates the shear stress and, thus, delays separation [41].

Hence, ANSYS Fluent features a set of tools to approach the near-wall region to counter said limitations. The selected ones, in this case, are semi-empirical formulas termed wall functions, used to solve the region between the wall and the fully turbulent zone. Taking into account the concepts previously introduced, it is important to mention that in ANSYS Fluent, for $k-\varepsilon$ models, the law of the wall is based on the wall unit, y^*, rather than y^+. The reason for this notation change is explained next.

If we consider the separation effect, characterised by wall shear tending to zero, then, looking at equation 3.17, the frictional velocity is also zero, which according to equation 3.15, the whole scaling breaks. Accordingly, ANSYS Fluent proposes a scale based on the turbulence kinetic energy given by

$$u^* = C_\mu^{\frac{1}{4}} k^{\frac{1}{2}} \quad (3.19)$$

that ultimately yields the law of the wall, as shown

$$U^* = \frac{1}{\kappa} \ln(Ey^*) \quad (3.20)$$

where $U^\star$ is the dimensionless velocity, defined as

$$U^* \equiv \frac{U_P C_\mu^{\frac{1}{4}} k_P^{\frac{1}{2}}}{\tau_w/\rho} \quad (3.21)$$

The dimensionless distance from the wall, $y^\star$, is defined as

$$y^* \equiv \frac{\rho C_\mu^{\frac{1}{4}} k_P^{\frac{1}{2}} y_P}{\mu} \quad (3.22)$$

In the previously displayed equations, U_P and k_P are, respectively, the mean velocity of the fluid and the turbulence kinetic energy at the wall-adjacent cell centroid, P, and y_P is the distance from the centroid of the wall-adjacent cell, to the wall. Furthermore, κ is the von Kármán constant, and E and C_μ are empirical constants of values 0.4187, 9.793 and 0.09, respectively.

In ANSYS Fluent, the log-law is employed when $y^* > 11.225$ and when the mesh is such

that $y^* < 11.225$ at the wall-adjacent cells, the laminar stress-strain relationship, $U^* = y^*$ is applied [41].

As previously stated, near-wall modelling is one of the most critical tasks in CFD. Figure 3.2 depicts the two ways to approach this subject. In the first one, the viscous sublayer and the buffer layer are not resolved. Rather, wall functions are employed to bridge the region between the wall and the fully turbulent region. The second approach consists of modifying the turbulence models to allow the viscosity-affected region to be resolved all the way to the wall.

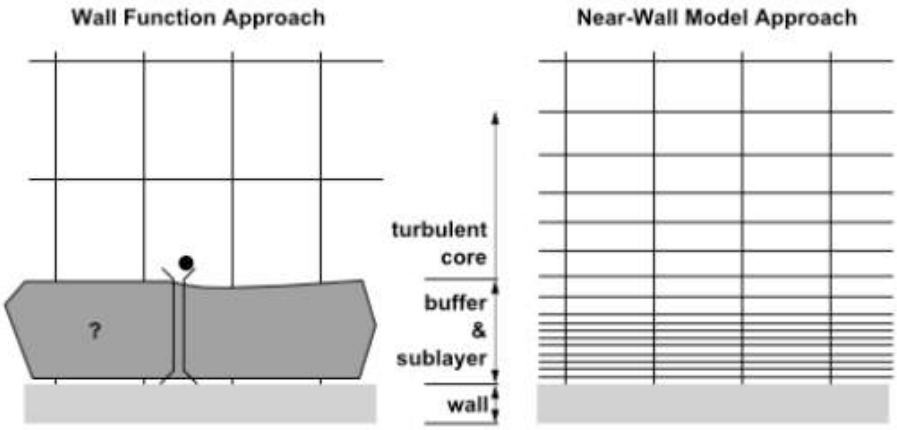

Figure 3.2: Near-wall treatments. [41].

These wall functions are not without limitations (except for the Scalable Wall Function). Namely, when the mesh is refined in the wall-normal direction, the quality of the results declines. y^+ values less than 15 will result in errors in wall shear stress. As such, advanced wall formulations were developed to allow consistent grid refinement without deteriorating the results. ω-equation-based turbulence models are examples of y^+-independent formulation.

For ε-equation-based models, y^+-independence is achieved by applying the Menter-Lechner and Enhanced Wall Treatment (EWT) wall functions. The Spallart-Allamaras turbulence model is also y^+-independent. As such, for ε-equation-based models, y^+ should be kept in the range of 30 to 300, while for ω-equation-based models, the values should be between 0 and 1 [41].

Additionally, the overall boundary layer resolution must be ensured. It is recommended that the boundary layer have at least 10 cells, but a value of 20 is preferable. After the solution is obtained, the boundary layer thickness can be recognised by analysing the turbulent viscosity since it displays a maximum value in the middle of the boundary layer. Thus, it should be ensured that the region located within twice the distance (from the wall) to the maximum turbulent viscosity value has at least 10 cells [41].

Since a $k - \varepsilon$ model is used in this dissertation, a wall function approach is needed to model

the near-wall region. There are several wall functions, but only the Standard Wall Functions and the Scalable Wall Functions will be presented for this work. The Standard Wall Functions are based on the work of Launder and Spalding [43].

Standard Wall Functions

Note that the means for determining the momentum were presented by equations 3.20, 3.21 and 3.22. Furthermore, heat transfer phenomena are not considered. Thus, the last part is the means for determining turbulence quantities.

Turbulence

In $k-\varepsilon$ models, the k equation is solved in the whole domain (even at wall-adjacent cells), while the ε equation is not. Instead, a local equilibrium hypothesis of equal production of turbulence kinetic energy (G_k) and its dissipation rate (ε) is assumed in the wall-adjacent control volume. Thus, G_k and ε are computed, respectively, from

$$G_k \approx \tau_w \frac{\partial U}{\partial y} = \tau_w \frac{\tau_w}{\kappa \rho C_\mu^{1/4} k_P^{1/2} y_P} \quad (3.23)$$

and

$$\varepsilon_P = \frac{C_\mu^{3/4} k_P^{3/2}}{\kappa y_P} \quad (3.24)$$

Although standard wall functions work fairly well for a broad range of wall-bounded flows, if flow cases deviate from the ideal conditions in which they were conceived, it may impact the quality of the predictions. Such is the case for near-wall flows subjected to severe pressure gradients [41].

Scalable Wall Functions

As previously mentioned, there might be a deterioration of the standard wall functions under grid refinement. Scalable wall functions can be used to avoid said deterioration. By including a limiter in the $y^\star$ calculations given by

$$\tilde{y^*} = MAX(y^*, y^*_{\text{limit}}) \quad (3.25)$$

it forces the employment of the log law along with the standard wall functions approach. In this formulation, $y^*_{\text{limit}} = 11.225$. Note that the formulation of the standard and scalable wall functions is identical. Thus, for this approach, one can replace y^* in the standard wall functions formulas for $\tilde{y^*}$ [41].

3.2 Numerical Model

In this section, the numerical model is presented. The first part describes the method for evaluating the partial differential equations. Lastly, the most relevant concepts behind ANSYS Fluent solver are covered, including how the equations are discretised so they can be numerically solved.

3.2.1 Finite Volume Method

Through the Finite Volume Method (FVM), partial differential equations are represented and solved in the form of algebraic equations. The method consists in dividing the domain into discrete control volumes using a computational grid. Then, the governing equations are integrated into the individual control volumes, resulting in algebraic equations for the discrete dependent variables and conserved scalars. Finally, the discretised equations are linearised, and the resulting linear equation system is solved, yielding the updated values of the dependent variables (e.g., velocities and pressure).

The FVM employs the Gauss Theorem to convert volume integrals in a partial differential equation that contains a divergence term into surface integrals. Considering a given vector field and a given volume within the field, the theorem states that the surface integral of the vector field over the closed surface (flux) is equal to the volume integral of the divergence over the region within the surface. If there are no sources in the volume (zero divergence), it gives that the inward flux is the same as the outward flux, and thus, the net flux is zero. Naturally, it results in the sum of all sources within the volume being equal to the net flux across the boundary of the considered volume.

Furthermore, in the FVM, the variables are determined at the cell centre and are considered to be constant throughout the cell, except for the cell's faces (edges). There, the values are interpolated from the cell centre values. As such, the method is conservative, seeing that the properties are transported from one cell to another through edge fluxes.

3.2.2 Solver Theory

The accounts herein presented are the most relevant concepts for one to understand the numerical algorithm behind the solver. Specifically, this subsection contains the typical inputs present in the solver's User Interface so that one may execute a successful simulation. The information is based on the ANSYS Fluent Theory Guide [41].

Pressure-Based Solver

The pressure-based solver employs an algorithm named the projection method, wherein by solving a pressure (or pressure correction) equation, the constraint of continuity of the velocity field is achieved. The pressure equation is derived from both the continuity and the momentum ones so that the velocity field, corrected by the pressure, satisfies the mass conservation (continuity). The solution process is iterative, seeing that the governing equations are repeatedly solved until the solution converges. ANSYS Fluent [41] provides two pressure-based solver algorithms: a segregated one and a coupled one.

In the segregated algorithm, the governing equations are solved sequentially and separately (decoupled). This algorithm is memory-efficient, given that the discretised equations are stored in the memory one at a time. On the other hand, the solution convergence is slower since the equations are solved in a decoupled manner. Thus, each iteration consists of the steps described below:

1. Update fluid properties (e.g. density, viscosity), including turbulent viscosity based on the current solution. If it is the start of the calculations, the properties of the fluid are given by the initialisation conditions.

2. Solve the momentum equations, one after the other, using the values of pressure and face mass fluxes updated in the previous step.

3. Solve the pressure correction equation using the recently attained values of the velocity field and mass fluxes.

4. Using the pressure correction recently obtained, the face mass fluxes, pressure and velocity field are corrected.

5. Solve the equations for additional scalars, such as turbulent quantities, using the current values of the solution variables.

6. Check if the equations have converged. If the convergence criteria are met, the process ends; otherwise, it returns to step 1.

Contrarily, the coupled algorithm solves a system of equations composed of the momentum equations and the pressure-based continuity equation. Hence, a single step replaces steps 2 and 3 of the segregated algorithm, in which the coupled system of equations is solved. As for the remaining equations, they are solved in a decoupled manner, as in the segregated algorithm.

Thus, choosing an algorithm is a matter of preference, although it should be noted that in the coupled one, the rate of solution convergence is significantly faster. However, at the

same time, computational memory requirements can be up to 2 times higher than that of the segregated algorithm. Figure 3.3 depicts the flowchart for each of the pressure-based algorithms.

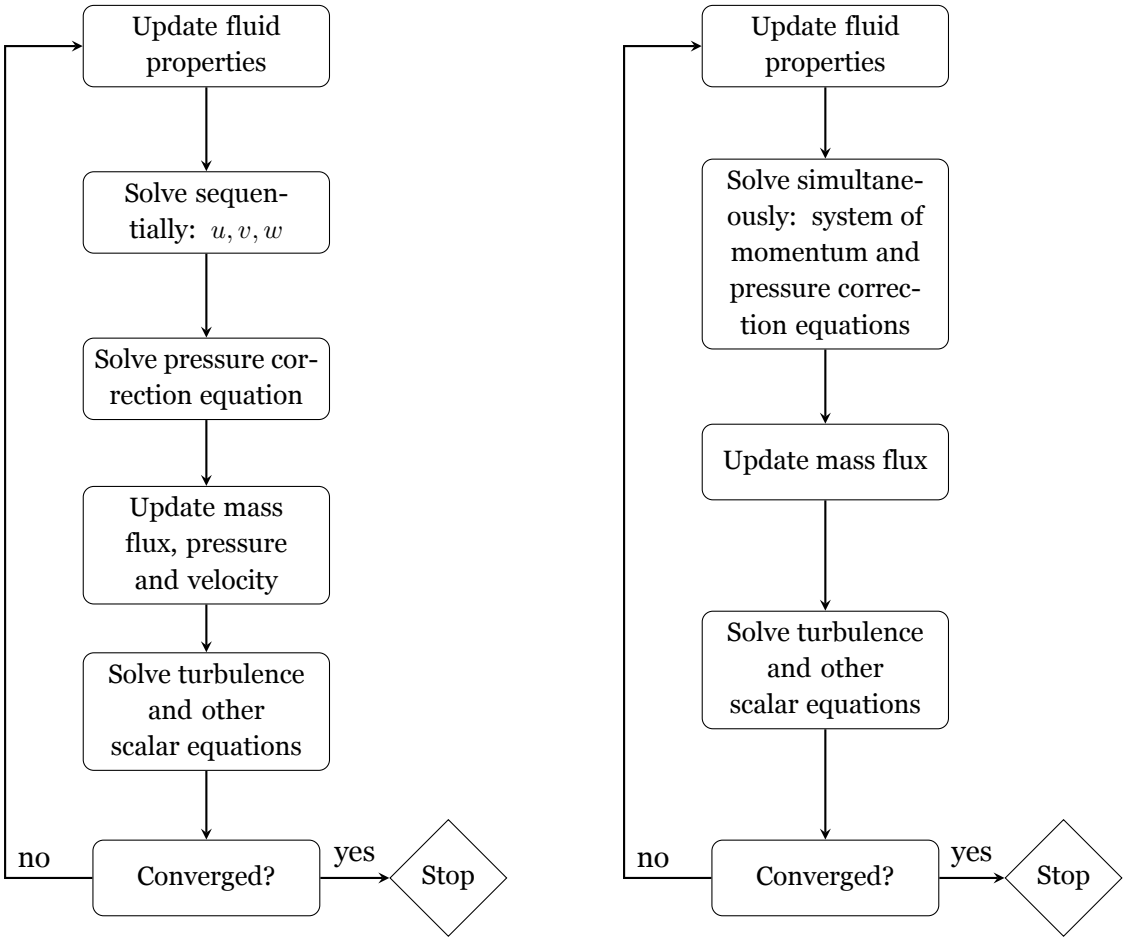

Figure 3.3: Flowchart of the pressure-based segregated (left) and coupled (right) algorithms. Adapted from [41].

For this dissertation, the coupled algorithm is chosen, owing to its faster convergence and seeing that the computational resources allow the increased memory usage.

Spatial Discretisation

Seeing that differential equations cannot be numerically solved in a direct manner, they first need to be converted into algebraic ones that can be solved. This process, called discretisation, employs a control-volume-based technique consisting of integrating a general transport equation inside each control volume, resulting in a discrete equation that expresses the conservation law on a control volume basis. The transport of a general scalar φ is written in the integral form as:

$$\int_V \frac{\partial \rho\varphi}{\partial t} dV + \oint \rho\varphi \overrightarrow{v} \cdot d\overrightarrow{A} = \oint \Gamma_\varphi \nabla\varphi \cdot d\overrightarrow{A} + \int_V S_\varphi dV \quad (3.26)$$

where $\overrightarrow{v}$ is the velocity vector ($u\hat{i}+v\hat{j}+w\hat{k}$, in 3D), $\overrightarrow{A}$ the surface area vector, Γ_φ the diffusion coefficient for φ, ∇_φ the gradient of φ and S_φ the source of φ per unit volume. Equation 3.26, which is applied to each control volume, is then discretised, yielding the following one

$$\frac{\partial \rho\varphi}{dt}V + \sum_{f}^{N_{\text{faces}}} \rho_f \overrightarrow{v}_f \varphi_f \cdot \overrightarrow{A}_f = \sum_{f}^{N_{\text{faces}}} \Gamma_\varphi \nabla\varphi_f \cdot \overrightarrow{A}_f + S_\varphi V \quad (3.27)$$

where N_{faces} is the number of faces enclosing a given cell, φ_f is the value of φ convected through face f, $\rho_f \overrightarrow{v}_f \varphi_f \cdot \overrightarrow{A}_f$ the mass flux through the face, $\overrightarrow{A}_f$ the area vector of face f, $\nabla\varphi_f$ the gradient of φ at face f and V the volume of the cell [41].

Note that the first term on the left-hand side of equation 3.26 is the temporal term, and it also undergoes a discretisation process, which will be described later. To better understand the spatial discretisation process, consider Figure 3.4, where a control volume example is depicted.

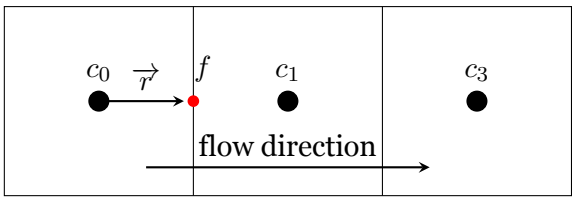

Figure 3.4: Control volume example.

It is worth noting that the solver used in this work stores the discrete values of the scalar φ at the cell centres (i.e., c_0, c_1, c_2), and yet, looking at equation 3.27, one can see that the face values φ_f are required for the convective terms and are, therefore, interpolated from the cell centre values. Thus, an upwind scheme is used for this task.

Considering the case in figure 3.4, this means that the face value φ_f is determined from quantities in the cell upstream (or "upwind") relative to the direction of the normal (to the face) velocity. If a first-order upwind scheme is selected, the face quantities are considered equal to the cell quantities (which is a cell-average value and is constant in the entire cell). Thus, the face value φ_f equals the cell centre value of φ in the upstream cell.

As for the second-order upwind scheme, the cell face values are computed with the expression $\varphi_{f,SOU} = \varphi + \nabla\varphi \cdot \overrightarrow{r}$, where φ and $\nabla\varphi$ are the cell-centred value and its gradient in the upstream cell, and $\overrightarrow{r}$ is the vector from the upstream cell centroid to the face centroid. Taking into account the flow case depicted in Figure 3.4, in order to compute the cell face value to the left of $c1$, the previous expression would consider the displacement vector $\overrightarrow{r}$ between c_0 and f, and the gradient in the cell containing c_0 [41].

Temporal Discretisation

If the simulations are transient, the governing equations must be discretised in space and time. Note that the spatial discretisation for the time-dependent equation is identical to steady-state cases. As such, the temporal discretisation is accomplished by integrating every term in the differential equations over a time step Δt. Hence, the time evolution of a variable φ is given by

$$\frac{\partial \varphi}{\partial t} = F(\varphi) \quad (3.28)$$

where the spatial discretisation is incorporated in the function F. Thus, the first-order accurate temporal discretisation is given by

$$\frac{\varphi^{t+\Delta t} - \varphi^{t}}{\Delta t} = F(\varphi) \quad (3.29)$$

where t is the value at the current time level. Note that a question remains regarding what time level values of φ to use when evaluating F. The solver provides a few methods for this, such as the first-order implicit time integration, where $F(\varphi)$ is evaluated at the future time level as

$$\frac{\varphi^{t+\Delta t} - \varphi^{t}}{\Delta t} = F(\varphi^{t+\Delta t}) \quad (3.30)$$

The implicit designation arises from the fact that $\varphi^{t+\Delta t}$ in a given cell is related to $\varphi^{t+\Delta t}$ in neighbouring cells through $F(\varphi^{t+\Delta t})$

$$\varphi^{t+\Delta t} = \varphi^{t} + \Delta t F(\varphi^{t+\Delta t}) \quad (3.31)$$

The implicit equation is solved iteratively at each time level before moving to the next time step [41].

Evaluation of Gradients

Looking at equation 3.26, one can note the presence of gradients in the convection and diffusion terms. One way to compute the gradients is the Green-Gauss Cell-Based method, where in the example depicted in Figure 3.4, the gradient at the cell centre c_0 is given by

$$(\nabla_{\varphi})_{c0} = \frac{1}{V} \sum_{f} \bar{\varphi}_f \overrightarrow{A}_f \quad (3.32)$$

where V is cell volume, and $\bar{\varphi}_f$ is the arithmetic average of the values at the neighbouring cell centres and is thus given by

$$\bar{\varphi}_f = \frac{\varphi_{c_o} + \varphi c_1}{2} \quad (3.33)$$

The summation in equation 3.32 is applied over all the faces surrounding the cell [41].

The Mesh

The mesh generation process is an integral part of any numerical simulation because it directly impacts the quality of the simulations. The flow domain is comprised of smaller subdomains called elements or cells, where the governing equations are discretised and solved. In a 2D analysis, mesh elements can be quadrilaterals and triangles, while 3D mesh elements can be hexahedra, tetrahedra, square pyramids, and extruded triangles. The collection of all elements is called mesh.

Meshes can be classified based on the connectivity of their elements, as a structured mesh or as an unstructured mesh. Structured meshes display more regular connectivity and are made of quadrilateral (2D) and hexahedral (3D) elements, and each mesh node is a common vertex for four adjacent cells. Unstructured meshes, on the other hand, display irregular connectivity and are computationally more demanding but, at the same time, are easily adaptable to complex geometries. Figure 3.5 depicts an example of a structured and unstructured mesh.

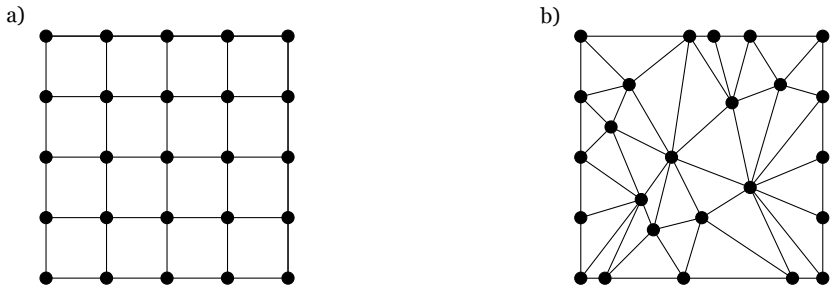

Figure 3.5: Example of a a) structured and b) unstructured mesh.

It is worth noting that a mesh may have structured portions and unstructured portions. Additionally, note that 3D meshes have exposed 2D elements at their boundaries. As such, some meshing software resort to a method known as surface meshing, which starts by meshing the bounding surfaces of a domain and then generating the interior elements. This method is employed by the Pointwise [44] software used in this dissertation.

Boundary Conditions

A Boundary Condition (BC) is a set of additional constraints exerted on differential equations in specified boundaries. Dirichlet-type BCs prescribe the value of the function on a surface. For Neumann-type BCs, the normal derivative of the function is prescribed on the surface.

Following the meshing, it becomes necessary to define the conditions of the boundaries surrounding the flow field. Only the boundary conditions relevant to this dissertation will be mentioned. Thus, these conditions can be flow inlet and exit boundaries and walls. The accounts herein presented are based on the Fluent manual [41].

Inlet and exit boundary conditions

- **Velocity inlet BC -** the velocity and scalar properties of the flow are defined at the inlet.

- **Mass flow inlet BC -** a mass flow rate is prescribed at the inlet, along with other inlet scalars, if needed. It allows the total pressure to vary according to the interior solution. This opposes the pressure inlet boundary condition, where the total pressure is specified, and the mass flow varies to ensure the imposed pressure.

- **Pressure outlet BC -** the exit BC is specified as a pressure outlet. The static pressure is determined based on the pressure specification method. For this work, a gauge pressure of 0 Pascal was imposed at the outlet. The outlet should be located in a region where the flow is close to a fully developed condition to facilitate convergence.

Wall boundary conditions

- **Walls -** for viscous flows, a no-slip boundary condition is imposed by default, but a slip wall can be modelled by specifying shear. A range of inputs can be specified, e.g., the wall motion condition (stationary or moving), shear conditions, wall roughness and others. For the turbulence kinetic energy (k), a zero normal gradient is applied $\left(\frac{\partial k}{\partial n} = 0\right)$, where n is the local coordinate normal to the wall.

Chapter 4

Numerical Procedure

"No methodology can guarantee success. But a good methodology can provide a feedback loop for continual improvement and learning."

Ash Maurya

This chapter covers the numerical procedure applied to the case study. First, the problem formulation is presented, followed by the geometry simplifications considered for the flow domain. Then, the meshing process is described, including the steps taken to ensure the construction of a structured mesh. Additionally, seeing that the numerical validation is a critical task, the mesh independence study and $y+$ wall distance validation are performed. Lastly, a summary of this chapter is shown.

4.1 Problem Formulation

The analysed section of the meander presents the typical configuration of natural meanders, with shallower inner banks and deeper outer banks. The reason behind this configuration has been previously covered. The section in Figure 4.1 is approximately $5000\,\mathrm{m}$ long, $200\,\mathrm{m}$ wide (average), and has a maximum water depth of $8\,\mathrm{m}$.

a) b)

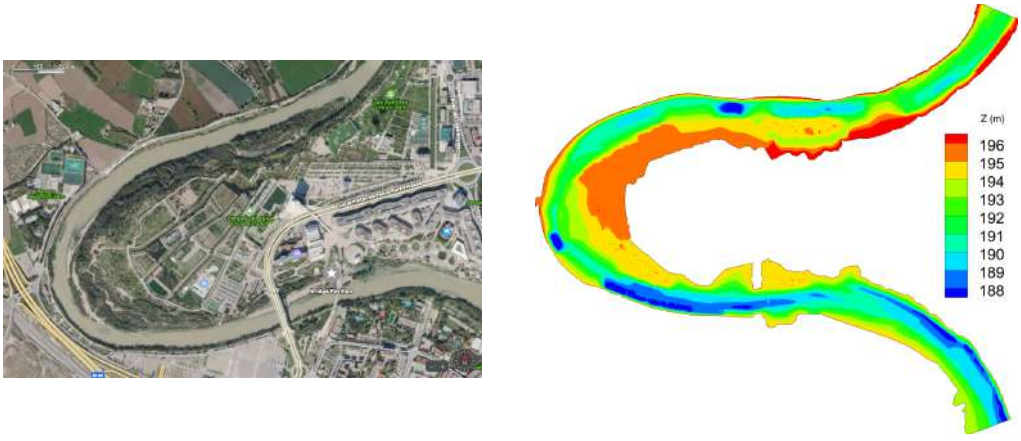

Figure 4.1: Section upstream of the Bridge Pavilion: a) Satellite image and b) bed topography.

Note that the satellite image in the figure above may be slightly different from the topographic survey, given that meanders are constantly changing systems. Given that a complex geometry tends to hinder the residuals' convergence, resulting in longer simulation times, the problem requires a careful approach. Of course, the size of the domain presents a particular challenge as well. Since turbulence models demand appropriate care at the near-wall region, as will be later explained in this chapter, one could imagine the excessive number of cells required to ensure a layer in the order of millimetres over a $5000\,\mathrm{m}$ extension. It would simply render the simulation impractical, if even possible.

As such, many studies have resorted to a set of simplifications, whether treating the problem as bidimensional (depth-averaged) or even considering a simplified meander geometry in the form of prismatic cross sections. Considering the interest in studying the secondary flow, the problem will be approached from a three-dimensional standpoint. However, a simplified cross-section will be considered for the turbulence model simulations.

Seeing that a free surface is present in open channel flows, the problem is, in principle, multiphase (water and air). Nevertheless, since simulating multiphase flows requires considerably more computational effort, a single-phase model will be adopted. Several studies have adopted this solution, as it has been shown that it results in accurate predictions of flow behaviour [9, 11, 23, 45]. This is known as the "rigid lid" approximation. Note that the free surface treated as a rigid lid is a valid approximation when the water depth variations are small ($< 10\%$) compared with the water depth itself [45] or when the Froude number is smaller than 0.5 [11]. This assumption may, however, suppress the generation of secondary currents [9]. To counteract this, a slope will be imposed on the free surface at the bend region, with a smooth transition to zero-slope at the straight channel reach.

Hence, the simulations will consist of three computational domains. One with the actual size and real bed topography of the meander, the other with a simplified geometry of the meander at a 1/62.5 scale, and the last with a straight channel of rectangular geometry. The last two models are used to understand the effects of the meander on the flow field. The proposed ratio of 1/62.5 is the same as the one adopted in the physical model of Martín-Vide [3]. Table 4.1 summarises the domains that will be considered.

Table 4.1: Simulated domains.

Designation	**Geometry**	**Scale**
Domain Type 1 (DT1)	Actual topography	1/1
Domain Type 2 (DT2)	Simplified	1/62.5
Domain Type 3 (DT3)	Rectangular (4 m x 0.141 m)	1/62.5

Geometry simplification procedure

The data used for the geometry simplification procedure comes from the work of Martín-Vide et al. [2]. In order to define representative cross-sections for the meander, seven locations

along the channel were analysed. Three locations of interest were considered (see Figure 4.2): the end of the meander bend, located approximately $450\,\mathrm{m}$ upstream of the 3rd Millennium Bridge (A - A'); a second location $200\,\mathrm{m}$ downstream of the 3rd Millennium Bridge; and the location of the Pavilion Bridge. These are representative locations for the transitions of the bed slope and the free surface slope along the meander. Finally, note that the right bank remains approximately straight (along the red line in Figure 4.2), while the left bank widens at an angle of $2°$.

Figure 4.2: Regions of interest for the geometry simplification procedure [1].

Thus, representative cross-sections of the meander were obtained for the constant flow rate of $2500\,\mathrm{m^3\,s^{-1}}$, which corresponds to a 2015 flood event. A linear transition of the bed slope and the free surface was used to connect each section. The resulting cross-sections are shown in Figure 4.3.

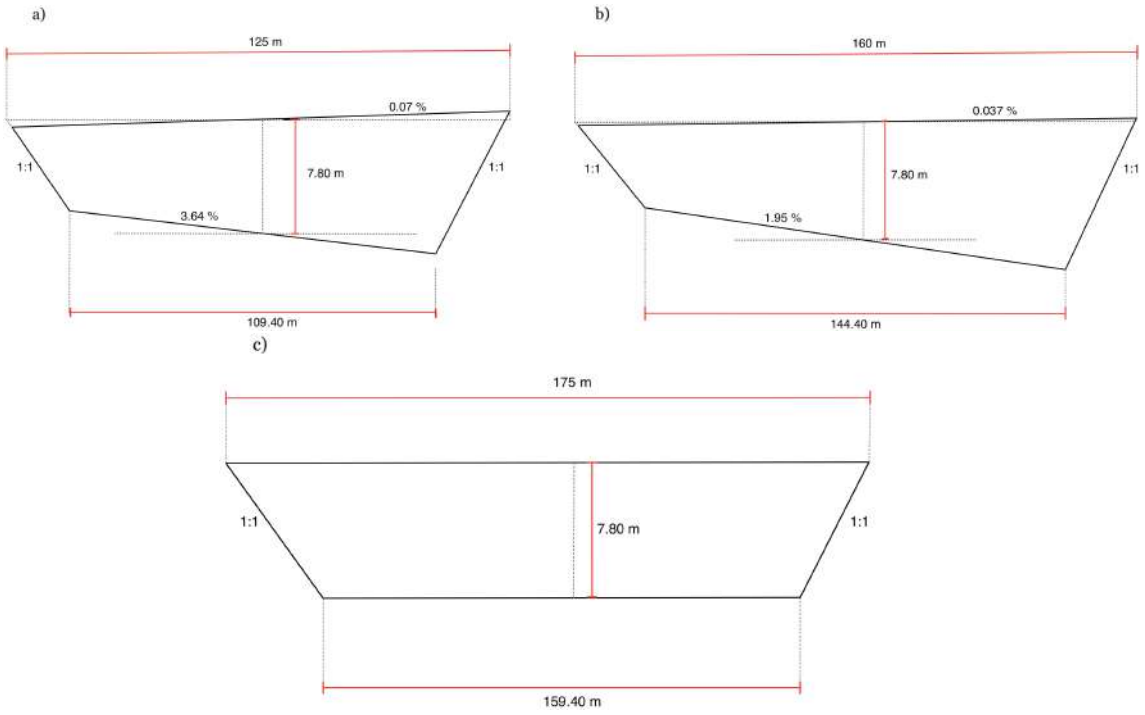

Figure 4.3: Representative cross-sections at a) meander bend exit, b) downstream of the 3rd Millennium Bridge and c) at the Bridge Pavilion. Figure not to scale.

Using satellite images of the meander, a Cartesian coordinate system was defined to obtain the coordinates along the axis of the channel. This data would later be imported into Fluent meshing and used to generate the meander's geometry.

The resulting domain comprises the cross-section of Figure 4.3 a) between the meander entrance up to A-A', a uniform transition of the previous cross-section and the one in b) between A-A' and $200\,\mathrm{m}$ downstream of the 3rd Millennium Bridge and, finally, a transition of the previous cross-section and the one in c) occurring at the Bridge Pavilion.

Flow similarity of the scaled model

As previously stated, DT 2 is a $1/62.5$ scaled-down model of the meander. A similarity of the effects is required for the results to be comparable to the real meander. This means that the scaled model has to reproduce phenomena as they are at full scale. A few key aspects are required for the similarity of scaled models [46, 47]:

- The use of only one geometric scale to avoid the model's distortion and better understand the results.
- Employment of an appropriate Froude similarity for gravity-dominated free surface flows.
- A turbulent developed flow in the model ($Re > 4000$).

Using the data from the flood event of 2015, with a flow rate of $2500\,\mathrm{m^3\,s^{-1}}$, the mean velocity at the inlet for the full-scale domain was $2.71\,\mathrm{m\,s^{-1}}$. By applying a Froude number similarity, the mean velocity at the inlet for the scaled model was $0.34\,\mathrm{m\,s^{-1}}$.

4.2 Computational Domain and Meshing

The computational domain consists in the field in which the simulations will be carried out. Its geometry, size and complexity directly impact the software's efficiency in producing accurate results, considering, of course, that the mesh is appropriate for the problem in question. Given that the maximum domain length that can be supported by the ANSYS [41] meshing software is $800\,\mathrm{m}$, the meshing of the DT1 was performed with the Pointwise [44] software. As previously mentioned, it is easier for unstructured meshes to adapt to complex geometries such as this one.

For DT1, the topographic data consisted of 1-meter contour lines of the meander's bed elevation. Thus, by linking the contour lines, the surface boundaries of the meander were created, which in Pointwise are designated as domains. Quality parameters of the surface mesh, such

as the aspect ratio and the equiangle and equiarea skewness of the elements, must be monitored to ensure the quality of the 3D elements. The aspect ratio of a cell should be as close to 1. As for the equiangle and equiarea skewness, which ranges from 0 to 1, the Pointwise manual [44] recommends that the values be kept lower than 0.8. Finally, all the domains were selected to assemble a block, which was then initialised to generate the interior cells. The centroid skewness of the cells was examined to determine if the values were below 0.8 (0.9 in some cases), as recommended. Smoothing parameters were also used to improve the overall quality of the mesh. This process yielded the computational domain depicted in Figure 4.4. Note the similarities with Figure 4.1.

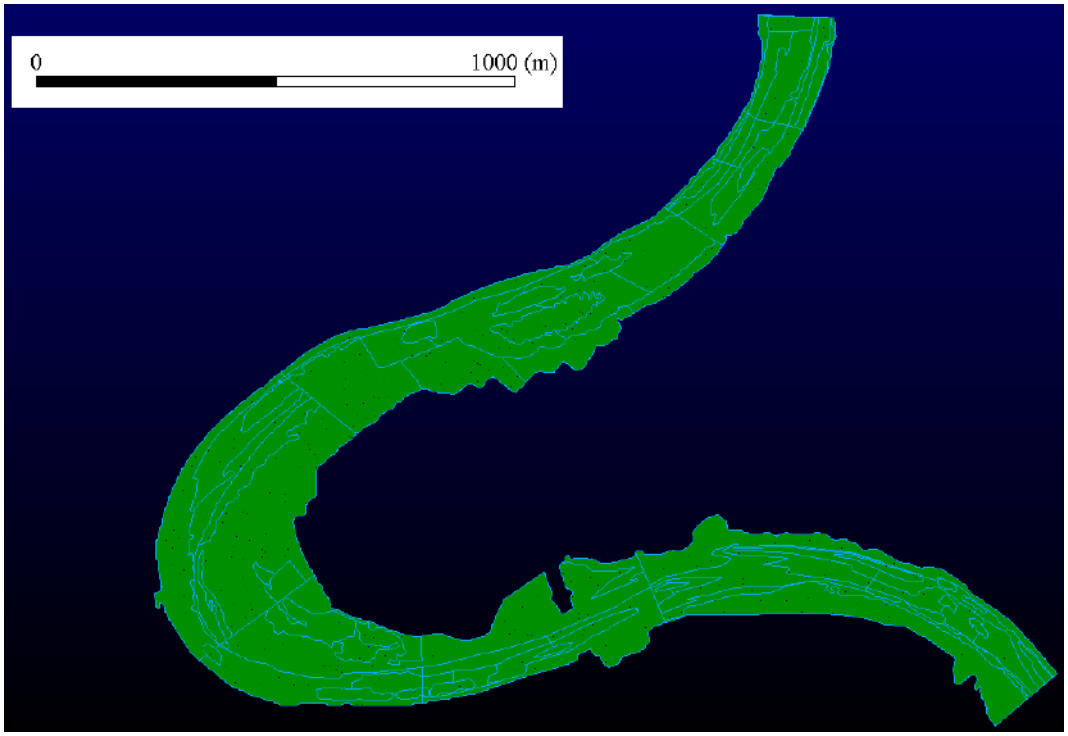

Figure 4.4: Mesh generated in Pointwise.

For DT2, the process started by generating the meander's geometry in Design Modeler. The cross-sections in Figure 4.3 were extruded along a path that described the curvature of the meander. Then, an initial mesh was generated by the solver. Because a structured mesh is preferable, various edge sizings were defined based on the number of divisions to facilitate mesh generation. Bias factors were selected accordingly to allow for a finer grid in the near-wall region without significantly increasing the number of elements. The domain was divided in half to aid the mesh generation and keep its distortion low, given that the meander has a somewhat high curvature.

The loft tool was used to generate the volume between the end of the curvature and the location of the Bridge Pavilion, ensuring a uniform transition to the bed's zero-slope and the top lid's zero-slope. This process resulted in five bodies, which were combined to form a Part. Figure 4.5 shows the resulting mesh.

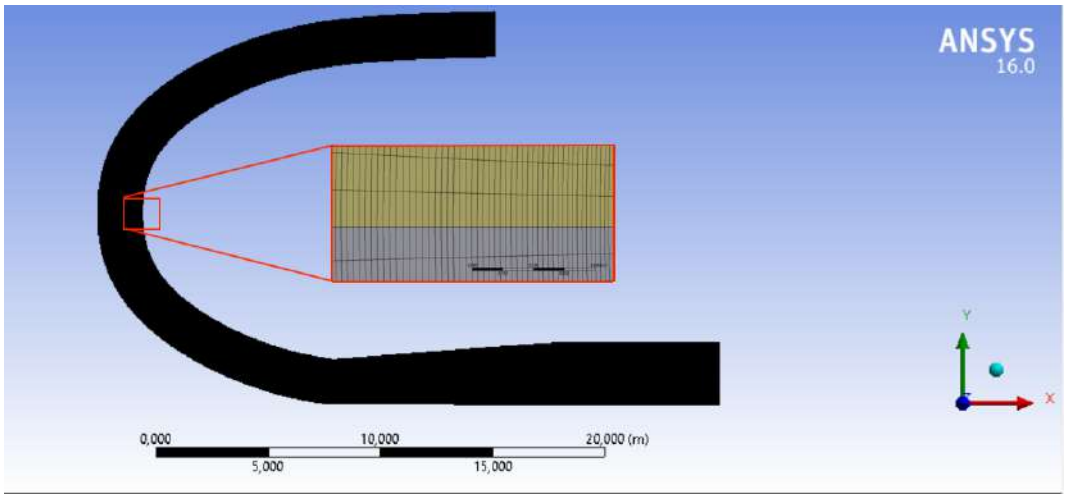

Figure 4.5: Mesh generated in Fluent meshing.

Since structured meshes generally yield better-quality elements than unstructured meshes, the more relevant quality parameter, in this case, was the aspect ratio of the elements. Considering that the near-wall region requires special attention, from a 2D standpoint, if the quadrilateral element has a very small height compared to its width, this would produce a high aspect ratio cell and would, thus, be a poor-quality element. Figure 4.6 depicts the zones of interest of the computational domain.

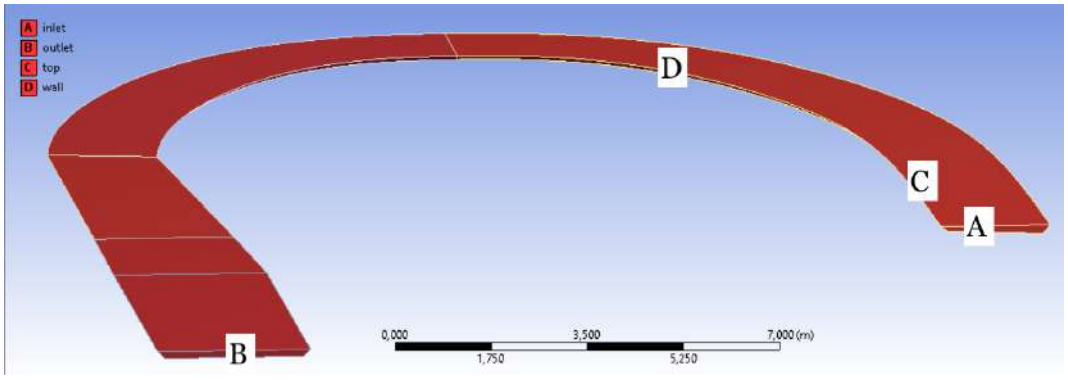

Figure 4.6: Bird's eye view of the boundary conditions of the computational domain.

Domain containing the bridge pier

The meshing of the domain containing the Bridge Pavilion's pier was somewhat similar but with a few extra steps. As can be seen in Figure 2.7, the pier is a goblet-like body. The outline of the pier was created from an AutoCAD® file containing the schematics of the pier. Then, a loft was applied between the base and the top outlines to generate the body. Its dimensions are shown in Table 4.2.

The resulting mesh is shown in Figure 4.7. Note that the mesh is structured in a cylindrical region near the pier. To achieve this, the body was split into four to facilitate mesh generation along the curvature of the pier. Special care was taken to ensure a smooth transition between

this region and the adjacent ones. Furthermore, an inflation of the mesh was made near the pier to ensure proper y^+ values.

Table 4.2: Bridge pier dimensions.

	Pier	Scale 1/62.5	Scale 1/1
Base	Major axis	0.45 m	27.9 m
	Minor axis	0.22 m	13.7 m
Top	Major axis	1.49 m	93.2 m
	Minor axis	0.32 m	20.1 m

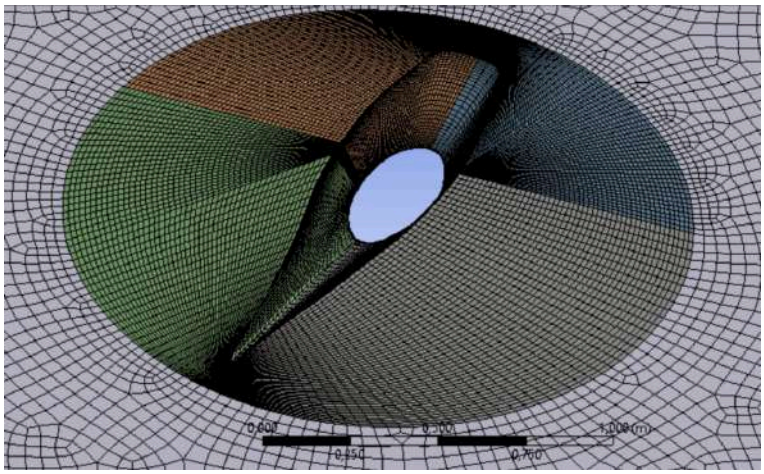

Figure 4.7: Detail of the mesh near the pier.

As previously stated, the meshing process is one of the most critical tasks in CFD. Greater mesh resolution means better quality results, but only up to a point, meaning that increasing the mesh resolution has a residual impact on the results. However, the computational effort, on the other hand, becomes just too great. Note that higher mesh resolution is required only at specific locations, such as in the proximity of walls. Hence, the meshing process comes down to ensuring a good quality grid while maintaining a reasonable computation time.

4.3 Numerical Validation

4.3.1 Mesh Independency Study

The mesh independence study is an essential step in any numerical analysis, as it ensures that the results are independent of the size of the mesh elements. For this purpose, a mesh with smaller cells is used, and the results are compared with the ones of the coarser mesh. This process is repeated until two consecutive meshes yield similar results. Table 4.3 shows the considered meshes.

One of the goals of this process is to define an optimal mesh so that the obtained results are accurate while at the same time having quick simulation run times. The procedure was

applied to DT2; the results are shown in Figure 4.8. It can be seen that the refinement of the mesh produces negligible differences in the velocity values.

Table 4.3: Mesh independence analysis for DT2.

Case	**Number of cells** [millions]	**Simulation time [mn]**
Mesh 1	1.05	15
Mesh 2	2.11	40
Mesh 3	4.22	100

The same analysis was performed in other sections and for different flow variables, and the results remained unchanged. As such, Mesh 2 is deemed appropriate and will be used for the simulations. The wake region was also studied for the domains containing the bridge pier.

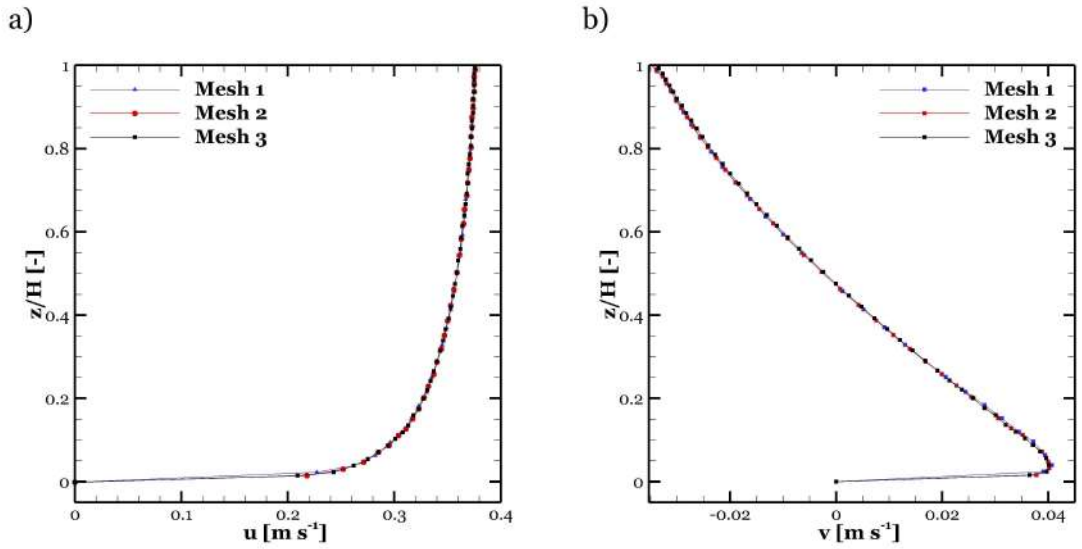

Figure 4.8: Profiles of a) streamwise velocity and b) spanwise velocity at Section A, under different mesh refinement. Data for DT2. Refer to Figure 5.3 for the location.

4.3.2 y^+ Wall Distance Validation

Given that the values of y^+ are used to compute de wall shear stress, it is necessary to ensure that it is within the range appropriate for the selected turbulence model. For the $k-\varepsilon$ turbulence model, the values should be kept between 30 and 300 [41]. Furthermore, under mesh refinement, the values of y^+ tend to decrease. As such, an analysis was made to ensure that the wall shear stress was not sensitive to these variations.

Figure 4.9 presents the contour of y^* at the walls. The reason for the notation change from y^+ to y^* was covered in subsection 3.1.4.

Only the domain containing the bridge pier is shown since it required greater care. However, the same verification was made for all other domains.

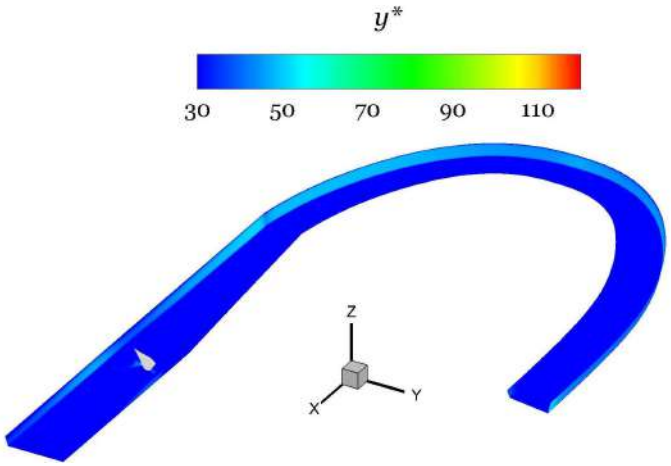

Figure 4.9: Wall $y*$ contour.

4.4 Summary

According to the concepts previously introduced, the summary of the simulation conditions for Domain Type 1 is shown in Table 4.4.

Table 4.4: Summary of the simulation conditions for DT1.

Solver	• Pressure-based • Transient
Model	• Standard $k - \varepsilon$
Boundary conditions	• Inlet - mass flow inlet • Outlet - pressure outlet • Walls - no-shear walls • Free surface - no-shear wall
Solution Methods	• Pressure-velocity coupling - Coupled • Gradient - Least squares cell based • Pressure - Second order • Momentum - Second order upwind • Transient formulation - First order implicit

For Domains Type 2 and 3, the simulation conditions are shown in Table 4.5.

Table 4.5: Summary of the simulation conditions for DT2 and DT3.

Solver	• Pressure-based • Steady
Model	• Standard $k - \varepsilon$ • Scalable wall functions
Boundary conditions	• Inlet - velocity inlet • Outlet - pressure outlet • Walls - no-slip walls • Free surface - wall with zero shear
Solution Methods	• Pressure-velocity coupling - Coupled • Gradient - Least squares cell based • Pressure - Second order • Momentum - Second order upwind • Turbulent kinetic energy - Second order upwind • Turbulent dissipation rate - Second order upwind

Finally, the imposed boundary conditions are summarised in Table 4.6.

Table 4.6: Boundary conditions for the simulated cases.

Boundary	**DT 1**	**DT 2**	**DT 3**
Inlet	$Q = 2500\,\mathrm{m^3\,s^{-1}}$	$U = 0.34\,\mathrm{m\,s^{-1}}$	$U = 0.34\,\mathrm{m\,s^{-1}}$
Outlet	Pressure outlet		
Walls	No slip		No shear
Free surface	No shear		

Chapter 5

Results & Discussion

"Discussion and argument are essential parts of science; the greatest talent is the ability to strip a theory until the simple basic idea emerges with clarity."

Albert Einstein

5.1 First Approach - Inviscid Assumption

The validity of the inviscid assumption has been covered in previous chapters. This simplification allows for an expedited and relatively accurate representation of the global behaviour of the flow field. Following the work of Santos et al. [48], a deeper analysis of the results obtained with the inviscid flow assumption is herein presented.

For this approach, DT1 is used, and the simulation conditions are summarised in Table 4.4. The simulation was performed with a flow rate of $2500\,\mathrm{m^3\,s^{-1}}$. The mean velocity and the hydraulic diameter at the inlet section were, respectively, $2.54\,\mathrm{m\,s^{-1}}$ and $15.7\,\mathrm{m}$, which results in a Reynolds number $Re = 4.5 \times 10^7$ and a Froude number $Fr = 0.2$. The flow domain was approximately $5000\,\mathrm{m}$ long, $250\,\mathrm{m}$ wide at the inlet section, and with a maximum flow depth of $9\,\mathrm{m}$. Owing to the complex topography, an unstructured mesh comprising 2.5 million cells was used. The analysis was carried over 3600 time-steps of 1 second each, resulting in a simulated flow time of 1 hour. These values were selected after ensuring mesh- and time-step-independence. Furthermore, a 1-hour flow time proved to be sufficient to capture the periodic phenomena within the flow field and to obtain an accurate estimation of the mean flow parameters. Figure 5.1 shows the contours of the mean velocity magnitude and mean static pressure at the river bed.

Note that non-zero velocity values at the bed result from the inviscid assumption. It can provide useful information about the locations prone to scouring. Despite the highly irregular topography, Figure 5.1 b) shows a trend for higher values of pressure on the outer bank and lower ones at the inner bank. This pressure gradient, in concurrence with the literature [7, 9, 49], results in the well-known secondary currents. Furthermore, several separation zones can be seen in Figure 5.1 a), which makes these locations prone to aggradation. Consider Figure 5.2, where the velocity vectors near the location of the Bridge Pavilion are shown.

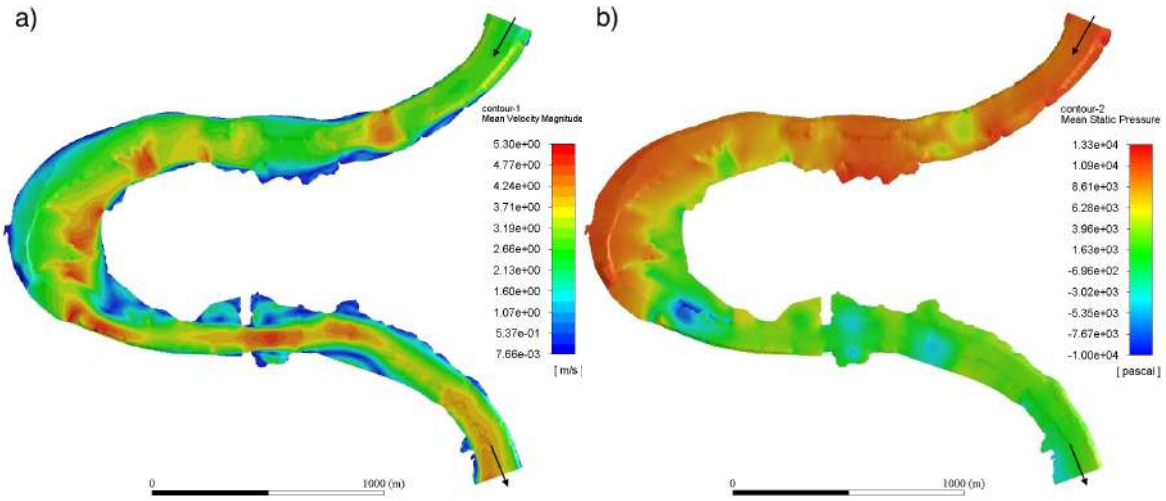

Figure 5.1: Contours of a) mean velocity magnitude and b) mean static pressure at the bed.

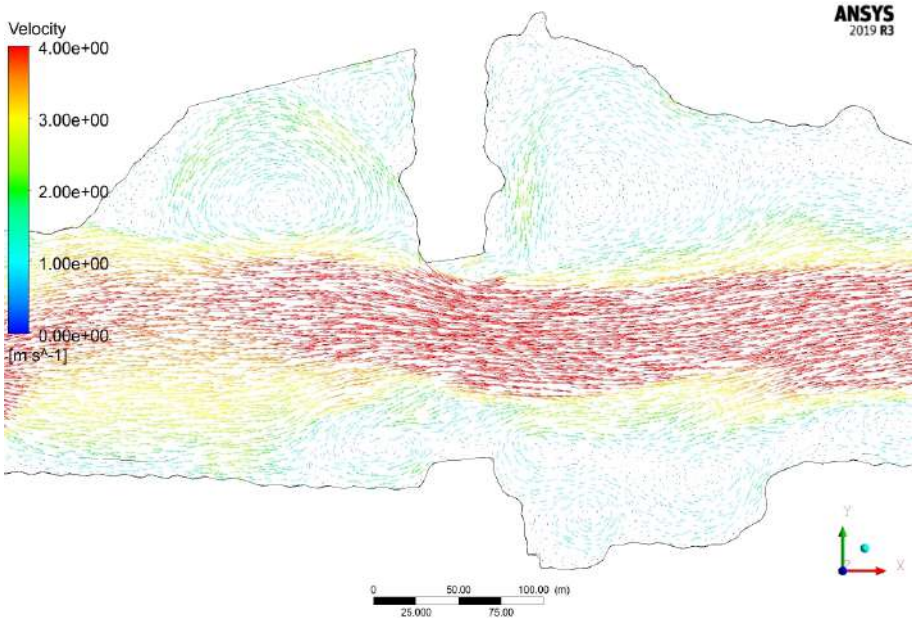

Figure 5.2: Velocity vectors near the location of the Bridge Pavilion.

As expected, the contraction of the flow width results in a region of high velocities. Two recirculation zones can be seen immediately downstream of the contraction, where several vortices are present. Another recirculation zone can be detected upstream of the contraction at the inner bank. These regions are highly prone to sediment deposition since particles have difficulty escaping from these low-velocity zones. Indeed, looking at Figure 4.1, in the section of the meander shown in Figure 5.2, the sediment accumulation in the inner bank is evident. This was also reported by Martín-Vide et al. [2]. Downstream of the Bridge Pavilion, the flow separates at the beginning of the right-hand curve, originating a low-velocity region susceptible to aggradation.

Note that given the inviscid flow assumption, actual velocity values are expected to be lower than the ones presented in this section. Although the results should be taken with caution, this approach has proven reliable for a qualitative assessment of the mean flow behaviour.

5.2 Second Approach - Turbulence Modelling

In this section, the results obtained with the turbulence modelling are presented. For this purpose, the $k - \varepsilon$ turbulence model was used to simulate a series of cases. For the first one, the computational domain consisted of a 1/62.5 scaled model of the meander without the bridge pier and with a simplified geometry according to the procedure described in the previous chapter. The mean velocity at the inlet was $0.34\,\mathrm{m\,s^{-1}}$, resulting in $Re = 4.2 \times 10^4$ and $Fr = 0.3$. In the simulated conditions, the curvature ratio is $R/B \approx 4$, which constitutes a mild bend, according to Kashyap et al. [11], and the channel's aspect ratio is $B/H \approx 17$. For the second case, the simulated conditions match the experimental work of Martín-Vide et al. [2], where the considered flow rate was $169.1\,\mathrm{L\,s^{-1}}$, and the water depth was $0.141\,\mathrm{m}$. The channel width was $4\,\mathrm{m}$, resulting in a mean inlet velocity of $\approx 0.34\,\mathrm{m\,s^{-1}}$. For further details on the experimental work, see Martín-Vide [3]. Finally, the same flow conditions and domain used in the first case were considered for the last case, but with the addition of the bridge pier. Hereafter, refer to Figure 5.3 for the location of the sections under study.

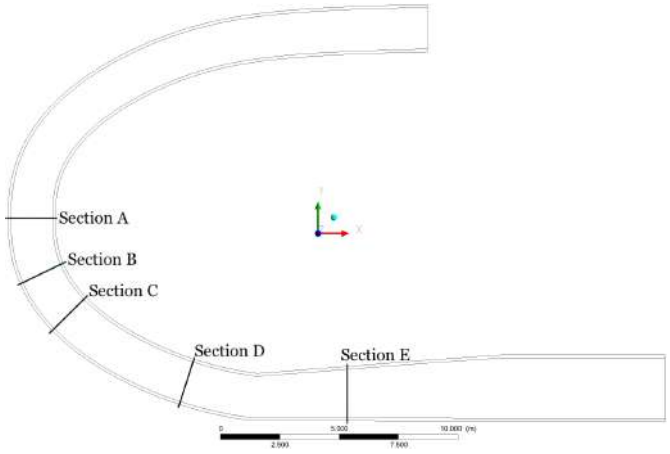

Figure 5.3: Location of the sections under analysis.

5.2.1 Effects of the meander

An initial analysis of the meander's flow field is conducted without the presence of the bridge pier. In Figure 5.4, the contour of the velocity magnitude, U_M, normalised by the mean inlet velocity, U, and the contour of pressure at the free surface are depicted. Within the bend reach, the velocity is lower at the inner bank. Near the bend exit, the core of high velocities is

located closer to the outer bank, with increases of up to 30%. Note that secondary currents are responsible for redistributing streamwise velocities [11, 50, 51], causing the advection of high velocities closer to the inner bank at the bend entrance to the outer bank at the bend exit.

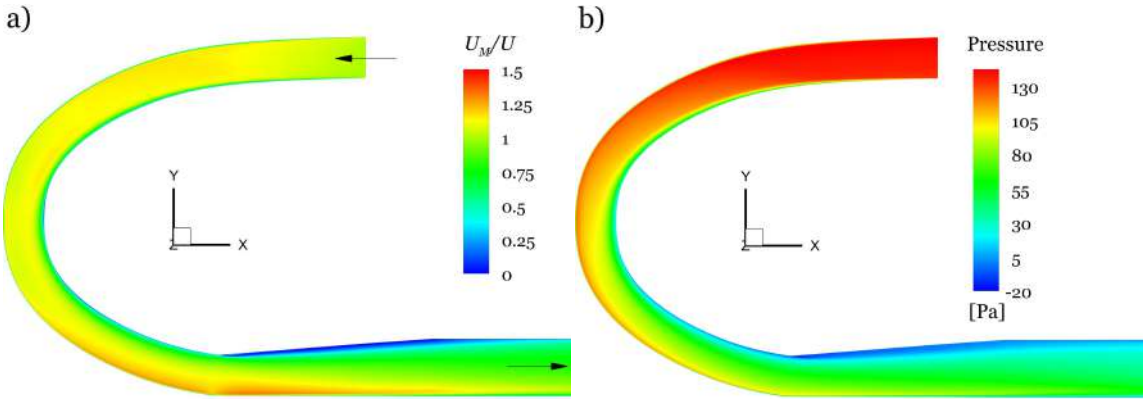

Figure 5.4: Contours of a) normalised velocity magnitude and b) pressure at the free surface.

From the pressure contour of Figure 5.4 b), it can be observed that the pressure gradient starts to decrease toward the bend exit, meaning that the secondary current will be increasingly weaker. This will be later shown in the analysis of cross-sections along the meander bend. Furthermore, a separation zone is formed at the inner bank as the channel expands after the bend exit. This region of low velocities is prone to higher sedimentation rates. Figure 5.5 shows the contour of wall shear stress magnitude, τ_M, normalised by the mean bed shear stress at a region close to the inlet, τ_0.

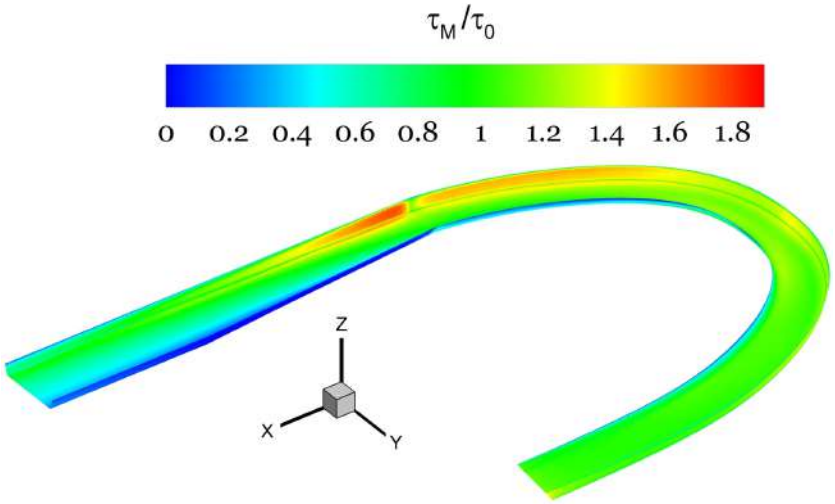

Figure 5.5: Normalised wall shear stress magnitude.

Note that the peak values of shear stress occur at the outer bank, where an increase of up to 80% is seen. This results from the flow velocities being advected toward the outer bank. In the straight reach downstream of the bend, shear stress values are low, which indicates that sediment deposition is likely. Consider Figure 5.6, where the contours of the normalised

spanwise velocities, v/U, and 2D streamlines are shown. As can be seen from the streamlines, the cross-circulation currents are well-defined at the sections within the bend. The flow is directed toward the inner bank near the bed and toward the outer bank at the surface.

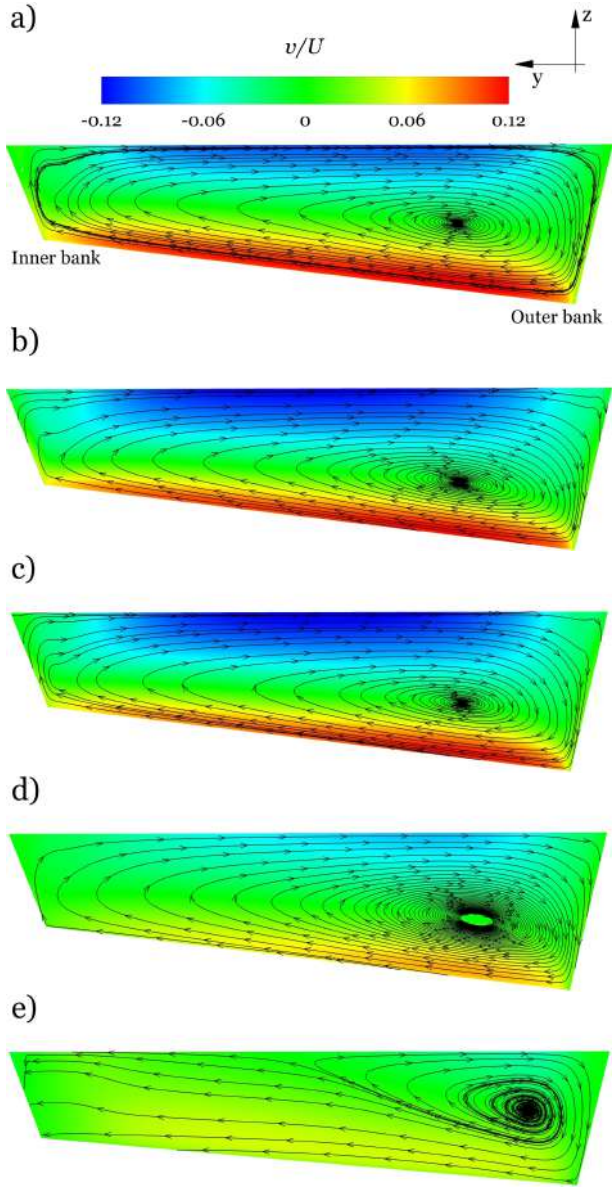

Figure 5.6: Normalised spanwise velocity, v/U, and 2D streamlines at a) Section A, b) Section B, c) Section C, d) Section D, and e) Section E.

The clockwise-rotating centre-region cell occupies most of the channel width and is stronger at Section B, attaining values up to 13% of the streamwise velocity. Near the bed, the flux is stronger closer to the outer bank, exacerbating the outer bank erosion. An analysis of the vertical velocity shows that the peak values (6% of U) occur at the inner and outer banks as the flow is forced upward or downward by the physical boundary. Moving toward the bend exit, the secondary current becomes increasingly weaker. At the beginning of the straight reach, its strength starts to decrease significantly, and at Section E, the cell occupies the region closer to the outer bank. Further downstream, it disappears and is replaced by a weak flux directed toward the inner bank.

Thus, as a result of the upstream meander, the flow is directed toward the inner bank at the location where the bridge pier would be present. This shows that a higher sediment load on the left span of the bridge is a natural tendency. Note that despite the high aspect ratio of the channel ($B/H \approx 17$), no cells are detected at the inner and outer banks. This can be attributed to RANS models suppressing their formation, as shown by Kashyap et al. [11] and Koken et al. [52].

5.2.2 Effects of the bridge pier in a straight channel reach

In order to better understand the effects of the bridge pier on the flow field, first, an analysis in a straight channel is required. The flow domain and conditions are described in the experimental works of [2, 53]. Thus, qualitative validation of the results is possible, although limited, given that the previous works used a deformable bed condition. Note that the unique shape of the pier and its skewed position relative to the flow renders comparisons of flow around uniform-shaped piers inadequate. As such, a tentative interpretation of the results is henceforth presented, based on the previously mentioned experimental works, coupled with a greater insight into the flow variables provided by the simulations. Figure 5.7 shows the normalised velocity magnitude at the free surface.

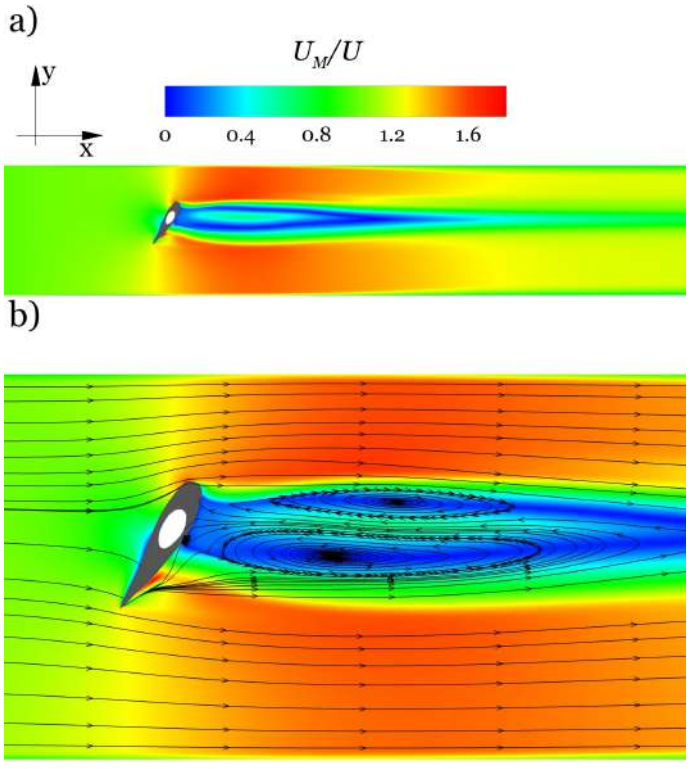

Figure 5.7: a) Velocity magnitude at the free surface and b) 2D streamlines and velocity magnitude near the pier.

The wake of the pier is clearly visible. Seeing that the pier acts as an obstruction to the flow, a velocity increase takes place as the flow goes around it. At the downstream side of the pier,

the vortex pair is visible (Figure 5.7 b), and a strong backflow (60% of U) takes place. The streamlines indicate that the flow near the right side of the pier is directed toward the left side as it goes around it.

As such, it is expected that sediment entrained from this area is prone to be directed towards the left side of the pier. Indeed, this behaviour was verified in the experimental work of Martín-Vide et al. [53]. Consider Figure 5.8, where the normalised spanwise velocity and 2D streamlines along two sections in the $x - z$ plane are shown.

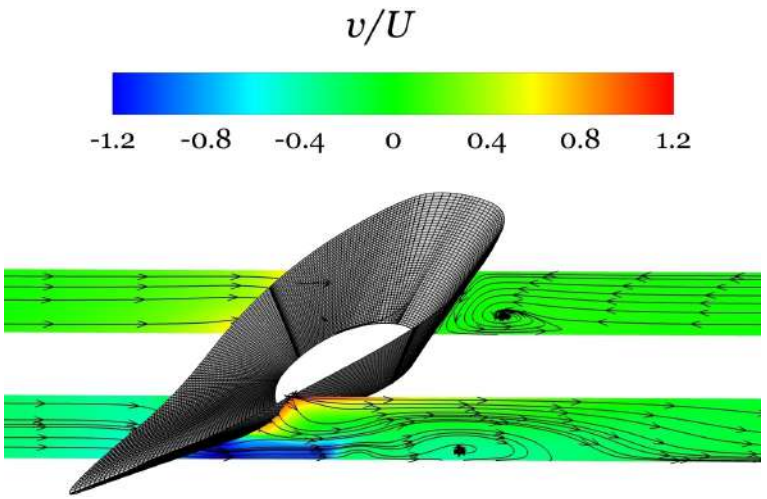

Figure 5.8: Normalised spanwise velocity and along sections in the $x - z$ plane.

Valuable insight into the flow pattern around the bridge pier is provided. The vortices on the left and right sides have alternating rotation. Since the pier is non-symmetric, different behaviour is expected on each side. In fact, its geometry plays a direct role in the flow field.

Looking at the section on the right side of the pier in Figure 5.8, the elongated shape results that the flow at the upstream face, which is diverted downwards, has a much narrower area available, causing a significant velocity increase.

As seen from the spanwise velocity contours, near the bed, the flow is quickly diverted outwards with a velocity that is 20% higher than the mean streamwise velocity. Thus, this region is expected to have severe erosion potential.

On the other hand, the left side of the pier shows a distinct behaviour. Given that the shape is not as elongated, there is less vertical obstruction, and the increase in velocity is not as high. Now, consider Figure 5.9, where the contour of the normalised turbulence kinetic energy, k/U^2, and the streamlines along a section at the centre of the pier are depicted. Turbulence kinetic energy (TKE) provides valuable information on the mean kinetic energy associated with the eddies present in the turbulent flow.

Upstream of the pier, the horseshoe vortex can be observed, with peak values of TKE occur-

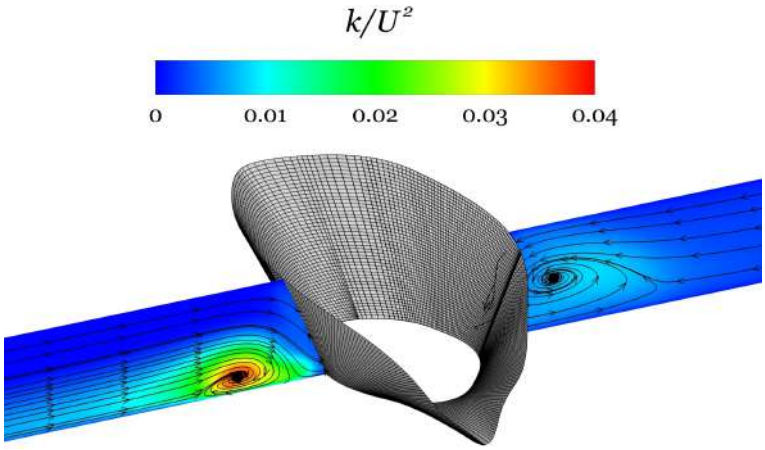

Figure 5.9: Normalised TKE along a section in the $x - z$ plane at the centre of the pier.

ring at its core. On the downstream side, a counterclockwise-rotating vortex develops higher up on the water column. Further insight into TKE is provided in Figure 5.10.

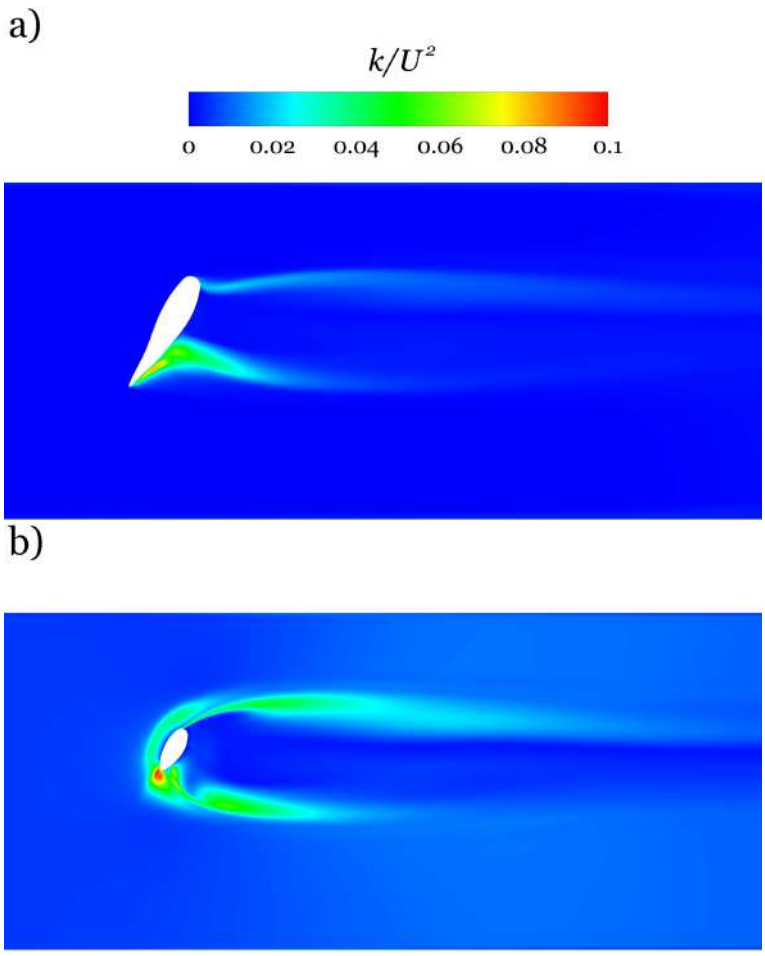

Figure 5.10: Normalised turbulent kinetic energy at a) the free surface and b) at $z/H = 0.1$.

In both images, the wake generated by the pier is clearly visible, extending a considerable distance downstream-wise. Near the pier, the flow is highly turbulent. Closer to the bed, peak values of TKE occur on the right side of the pier. Toward the free surface, values of TKE present a general increase owing to higher flow velocities but start to decrease again near the free surface. The peak values of TKE near the bed mean that strong fluctuations of the velocity field occur, which can increase the erosion potential.

Finally, the normalised wall shear stress magnitude is shown in Figure 5.11. The results focus on the region near the pier since it is where bed shear stress peak values occur.

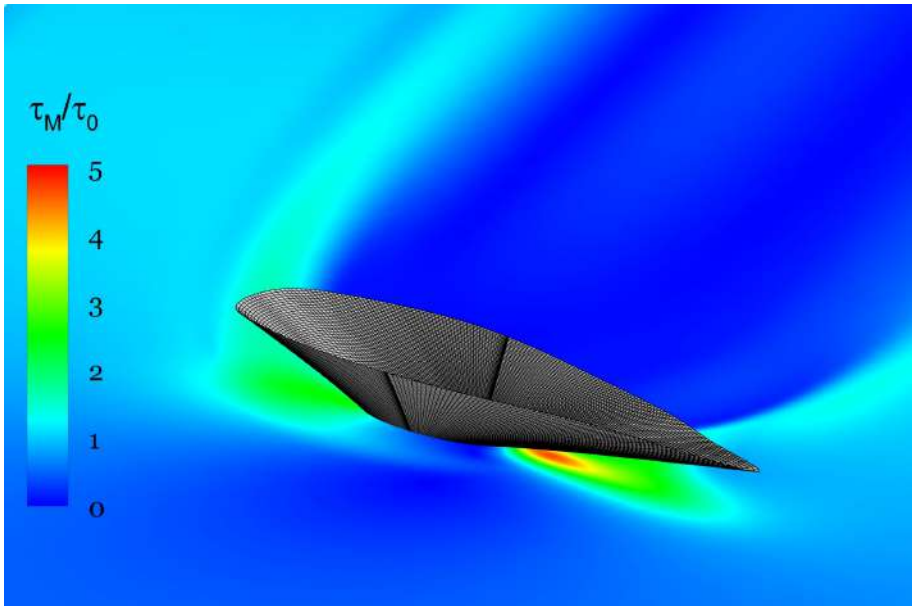

Figure 5.11: Normalised wall shear stress magnitude, τ_M/τ_0.

At this location, the bed shear stress increases, on average, two-fold. The results at the right side of the pier are particularly interesting. Here, the shear stress increases up to five-fold. As previously discussed, the elongated shape of the pier can explain these results. Looking at Figure 5.12, it can be noted that the bed shear stress results are consistent with the scour hole shape obtained experimentally in [2, 53].

Furthermore, higher scouring occurred on the right side of the pier, which coincides with the location of the peak values of bed shear stress obtained in the simulations. The region of relatively low turbulence and bed shear stress within the area of the wake indicates that sediment accumulation is likely. This is concurrent with the results observed in the lab and on the field, where a bar formed downstream of the bridge pier.

Figure 5.12: Equilibrium state following local scour tests.

5.2.3 Effects of the bridge pier in a meandering bend

As mentioned before, an analysis of each case was required to separate the effects of the meander on the flow field from the ones caused by the bridge pier. Thus, in this subsection, a cross-comparison of the previous results is made, with the aim of providing a better understanding of the complex flow dynamics that arise from the combination of the meander and the bridge pier. The normalised velocity magnitude is presented in Figure 5.13 a).

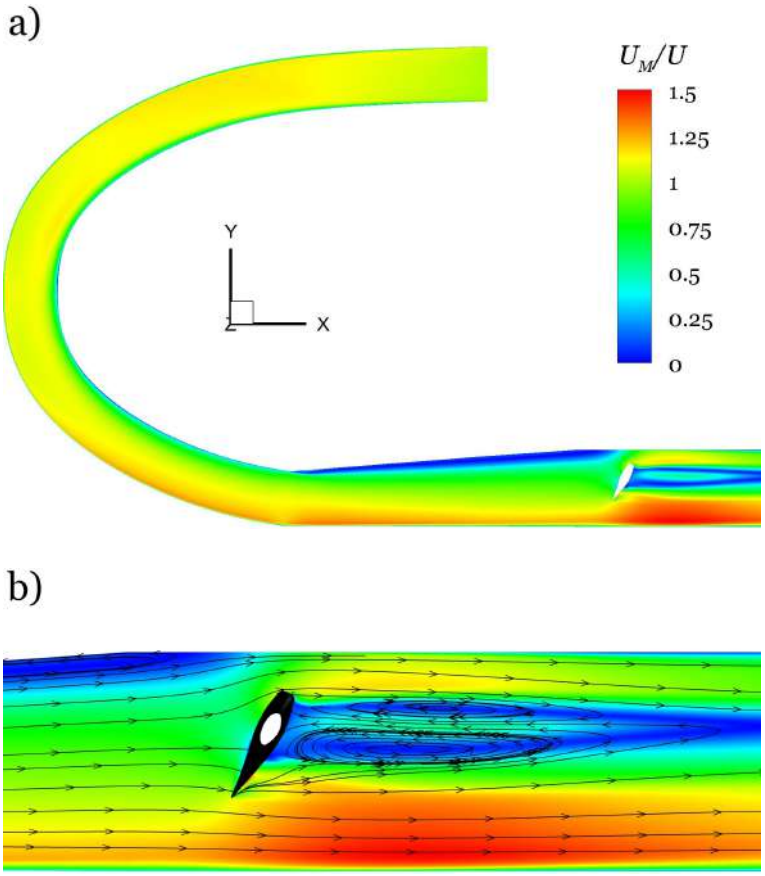

Figure 5.13: Normalised velocity magnitude, U_M/U, at a) the free surface and b) streamlines near the pier.

Looking at the region along the meander bend, the pier did not produce significant changes in the velocity field (see Figure 5.4). The most noticeable changes occur near the pier. The flow rapidly accelerates on the right side, resulting from the bulk of the flow already being directed to the outer bank (by the upstream meander) and the obstruction caused by the pier. Here, the velocity increases up to 50%. Note that this behaviour was not displayed in the straight channel reach case, where the velocity increase was equal on both sides of the pier (Figure 5.7). Upstream, the flow still separates at the inner bank expansion, where a low-velocity zone is visible. On the downstream side, the vortex pair can be seen. Close to the bed, the velocity increases by 20% at the right side of the pier. As previously mentioned, this region is prone to significant erosion.

Figure 5.14 shows the normalised spanwise velocity along two sections on both sides of the pier. Comparing the results with the ones in Figure 5.8, it can be seen that although the spanwise velocities are high (values close to the streamwise velocity), the increase is not as sharp, on both sides of the pier, as in the straight channel case. On the right side, particularly, this can be attributed to the flow being concentrated at the outer bank, and thus, the pier does not obstruct the flow as much as in the straight channel case.

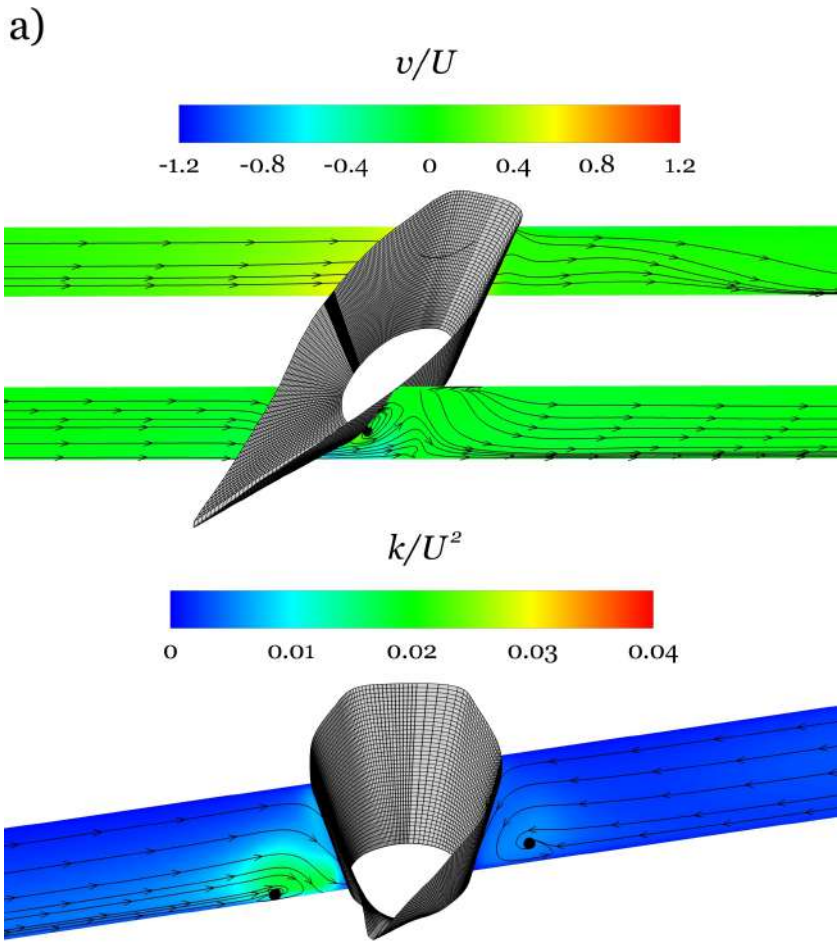

Figure 5.14: a) Normalised spanwise velocity and b) normalised TKE along sections in the $x - z$ plane.

An analysis of the TKE shows a similar pattern as in Figure 5.10, although with less intensity. As demonstrated by Figure 5.14 b), the turbulence generated at the pier is weaker in the presence of the meander. The horseshoe vortex still forms on the upstream side, but TKE values decrease by 50%, compared to Figure 5.8. Furthermore, the vortex on the downstream side is weaker, and its core is closer to the bed.

Consider Figure 5.15, where the shear stress magnitude at the bed is shown. As expected, the highest values occur closer to the pier. Again, on the right side is where the peak values occur, with values increasing up to 7 fold. This behaviour is consistent with the physical model surveys, where the deepest scour hole developed on the right side of the pier [2, 53]. Finally, note the existence of a region of low velocities, turbulence and shear stress downstream of the pier. This indicates that this region could be prone to sediment deposition. Indeed, as data showed, the islet on which the pier was built grew over the years as a result of sediment deposition [2].

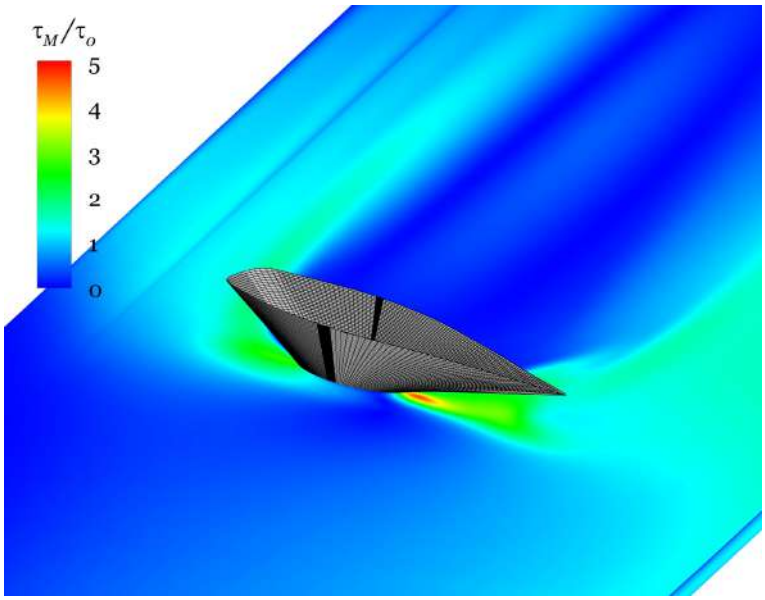

Figure 5.15: Normalised wall shear stress magnitude.

Since no significant changes to the velocity field were produced upstream of the pier, the pattern and strength of the secondary currents are similar to the ones in Figure 5.6. Hence, the figure will not be presented. It is worth mentioning, however, that the most relevant changes occur downstream of Section E. In the case where the pier was not present, the circulation cell dissipates at a faster rate. In the case with the pier, the cell remains coherent, almost up to the pier's location. In a sense, the pier slows the decaying of the main cell, even as the bend ends.

Chapter 6

Conclusions & Future Work

"Remember to look up at the stars and not down at your feet. Try to make sense of what you see and wonder about what makes the universe exist. Be curious. And however difficult life may seem, there is always something you can do and succeed at. It matters that you don't just give up."

Stephen Hawking

6.1 Conclusions

In the present work, the numerical analysis of the Ebro River meander flow field was performed. Ever since its construction, the large bridge pier of the emblematic Bridge Pavilion (Zaragoza) has raised concerns about exacerbated local scour in the vicinity of the pier. Over the years, bed aggradation over the left bridge span and deep scour over the right were observed. The morphological changes that resulted from a subsequent flood event made clear the need for a deeper understanding of the meander's hydrodynamics. As such, this work aimed to do just that by coupling the existing experimental work with a greater insight into the flow's variables provided by numerical simulations.

In order to isolate the influence of the meander from the influence of the pier, a series of cases were tested. The first considers only the meander, the second with the pier inside a straight channel, and the last considers the meander with the pier. The $k - \varepsilon$ turbulence model proved reliable in predicting the flow field even if, according to the literature, it can potentially suppress the formation of the outer-bank cell.

Results show that the upstream meander directs the core of high velocities toward the outer bank. Thus, at the pier's location, a higher flow rate is imposed on the right span of the bridge, which is expected to increase the erosion potential. On the right side, the velocity increases up to 50%, whereas on the left side, a 20% increase is seen.

The size and shape of the pier likely, play a direct role in the bed shear stress. Over the right span, the pier has an elongated shape, leaving a narrow area for deflected flow as it circles the pier. As such, close to the bed, the flow accelerates and is pushed outwards, with an intensity

comparable to the mean streamwise velocity.

The inner bank is prone to sediment accumulation, especially at the separation zone forms, as the width of the meander increases at the straight upstream reach. Furthermore, the results suggest that, as they go around the pier, suspended sediments transported close to the surface will be directed down and toward the recirculation zone formed by the vortex pair downstream of the pier. As observed in field surveys and laboratory experiments, this region is prone to sediment accumulation. The horseshoe vortex detected at the upstream face of the pier is also expected to contribute to bed erosion.

Results of the turbulence kinetic energy (TKE) show decreased values when compared to the straight channel reach case. This can be attributed to the bulk of the flow being directed toward the outer bank in the presence of the meander. However, TKE exhibits peak values close to the pier, especially over the right span and closer to the bed. Looking at the bed shear stress magnitude shows just how problematic the right span of the bridge is. Here, shear stress values increase up to 5-fold, whereas a 2-fold increase is seen in the region close to the pier. The shape of the high-shear stress areas obtained in the simulations is consistent with the shape of the scour hole observed in experimental works.

As for the secondary currents, no significant intensity differences were found between the case with the pier and the one without, which suggests that the upstream influence of the pier is limited to the region close to its location. Along the bend, the main circulation cell is well-established and spans most of the channel width. The circulation currents are strongest at Section B ($115°$), with values up to 12% of the mean streamwise velocity. Past this section, its intensity starts to decrease progressively, and from the bend exit, it starts to decay sharply until it is replaced by a weak flux directed exclusively to the inner bank.

In a closing tone, it should be said that despite numerical tools' high level of detail, they are not without limitations. The main one is computational resources. Indeed, when coupled with experimental and field works, numerical tools allow for an in-depth approach, especially in high-complexity cases such as this one.

6.2 Suggestions for Future Works

Following the work carried out in the present dissertation, a few suggestions can be made that would allow a better insight into the flow hydrodynamics near the Zaragoza Bridge Pavilion. A great deal of knowledge could be obtained from the following:

- Using the Reynolds Stress Model (RSM) turbulence model, as it would account for turbulence anisotropy and, possibly, better represent the secondary flow mechanisms, namely, the detection of the outer bank cell;

- Implement the Discrete Phase Model (DPM) to simulate sediment transport in the meander and compare the results with the field data.

- Conduct simulations with a deformable bed, allowing the comparison of the surveyed scour and the one obtained in the simulations;

- The use of a multiphase flow;

- Numerically analyse what measurements could be taken to decrease scouring rates in the vicinity of the pier. For example, a bubble curtain surrounding the pier could be used to reduce the strength of the downflow at the upstream face of the pier.

References

[1] Google LLC. (2021). [Online]. Available: https://maps.google.com xv, 2, 39

[2] J. P. Martín-Vide, C. M. S. Fael, F. Núñez-Gonzáez, C. Ferrer-Boix, C. A. V. Santos, A. Prats-Puntí, and V. Chavarrias, "A large bridge pier in an alluvial channel: Local scour versus morphological effects and the role of physical models," *Journal of Hydraulic Engineering*, vol. 148, no. 8, aug 2022. 2, 10, 14, 15, 16, 38, 48, 49, 52, 55, 58

[3] J. P. Martín-Vide, "Estudio hidráulico en modelo físico de la protección del pabellón-puente de la expo 2008," Universitat Politècnica de Catalunya and Universidade da Beira Interior, Tech. Rep., 2008. 3, 14, 38, 49

[4] Zaha Hadid Architects. (2008) Bridge Pavilion, Zaragoza. [Online]. Available: https://arquitecturaviva.com/works/bridge-pavilion-in-zaragoza-6 3

[5] K. Blanckaert, "Hydrodynamic processes in sharp meander bends and their morphological implications," *Journal of Geophysical Research: Earth Surface*, vol. 116, no. F1, pp. n/a–n/a, jan 2011. 5, 7, 8

[6] C. T. Yang and C. C. S. Song, "Theory of minimum rate of energy dissipation," *Journal of the Hydraulics Division*, vol. 105, no. 7, pp. 769–784, jul 1979. 5

[7] K. Blanckaert and H. J. D. Vriend, "Secondary flow in sharp open-channel bends," *Journal of Fluid Mechanics*, vol. 498, pp. 353–380, jan 2004. xvii, 5, 6, 7, 8, 17, 47

[8] K. Blanckaert, G. Constantinescu, W. Uijttewaal, and Q. Chen, "Hydro- and morphodynamics in curved river reaches – recent results and directions for future research," *Advances in Geosciences*, vol. 37, pp. 19–25, dec 2013. 5, 9

[9] A. Khosronejad, C. D. Rennie, S. A. A. S. Neyshabouri, and R. D. Townsend, "3d numerical modeling of flow and sediment transport in laboratory channel bends," *Journal of Hydraulic Engineering*, vol. 133, no. 10, pp. 1123–1134, oct 2007. xvii, 5, 19, 38, 47

[10] J. Thomson, "Experimental demonstration in respect to the origin windings of rivers in alluvial plains, and to the mode flow of water round bends of pipes," *Proceedings of the Royal Society of London*, vol. 26, no. 179-184, pp. 356–357, dec 1878. 5

[11] S. Kashyap, G. Constantinescu, C. D. Rennie, G. Post, and R. Townsend, "Influence of channel aspect ratio and curvature on flow, secondary circulation, and bed shear stress in a rectangular channel bend," *Journal of Hydraulic Engineering*, vol. 138, no. 12, pp.

1045–1059, dec 2012. xvii, 5, 7, 8, 18, 38, 49, 50, 52

[12] G. C. Cheng and S. Farokhi, "On turbulent flows dominated by curvature effects," *Journal of Fluids Engineering*, vol. 114, no. 1, pp. 52–57, mar 1992. 6, 7

[13] K. C. Cheng, R.-C. Lin, and J.-W. Ou, "Fully developed laminar flow in curved rectangular channels," *Journal of Fluids Engineering*, vol. 98, no. 1, pp. 41–48, mar 1976. 7

[14] H. J. D. Vriend, "Velocity redistribution in curved rectangular channels," *Journal of Fluid Mechanics*, vol. 107, no. -1, p. 423, jun 1981. 7

[15] K. H. Winters, "A bifurcation study of laminar flow in a curved tube of rectangular cross-section," *Journal of Fluid Mechanics*, vol. 180, no. -1, p. 343, jul 1987. 7

[16] H. J. Vriend, "Steady flow in shallow channel bends," phdthesis, Technische Universiteit Delft, Jun. 1981. 7

[17] H. B. Christensen, G. K., and J. Fredsøe, "Secondary turbulent flow in an infinite bend," in *I.A.H.R. Symposium on River, Coastal and Estuarine Morphodynamics*. University of Genova, Department of Environmental Engineering, 1999. 7

[18] K. Blanckaert and W. H. Graf, "Momentum transport in sharp open-channel bends," *Journal of Hydraulic Engineering*, vol. 130, no. 3, pp. 186–198, mar 2004. 7, 8

[19] M. R. Leeder and P. H. Bridges, "Flow separation in meander bends," *Nature*, vol. 253, no. 5490, pp. 338–339, jan 1975. 8, 9

[20] B. L. Rhoads and A. N. Sukhodolov, "Field investigation of three-dimensional flow structure at stream confluences: 1. thermal mixing and time-averaged velocities," *Water Resources Research*, vol. 37, no. 9, pp. 2393–2410, sep 2001. 8

[21] R. J. Hardy, J. L. Best, T. I. Marjoribanks, D. R. Parsons, and N. J. Rosser, "Detection and analysis of coherent flow structures in a depth-limited flow over a gravel surface," in *Coherent Flow Structures at Earth's Surface*. John Wiley & Sons, Ltd, sep 2013, pp. 199–214. 8

[22] A. N. Sukhodolov, I. Schnauder, and W. S. J. Uijttewaal, "Dynamics of shallow lateral shear layers: Experimental study in a river with a sandy bed," *Water Resources Research*, vol. 46, no. 11, nov 2010. 8

[23] G. Constantinescu, M. Koken, and J. Zeng, "The structure of turbulent flow in an open channel bend of strong curvature with deformed bed: Insight provided by detached

eddy simulation," *Water Resources Research*, vol. 47, no. 5, may 2011. 9, 10, 25, 38

[24] B. F. Edwards and D. H. Smith, "River meandering dynamics," *Physical Review E*, vol. 65, no. 4, p. 046303, mar 2002. 10

[25] C. M. S. Fael, "Erosões localizadas junto de encontros de pontes e respectivas medidas de protecção," phdthesis, Universidade da Beira Interior, 2007. 11

[26] B. W. Melville and S. E. Coleman, *Bridge Scour*. Water Resources Pubns, 2000. 11, 13, 14

[27] A. Raudkivi, "Scour at bridge piers," in *Scouring*. CRC Press, jul 2020, pp. 61–98. 11, 14

[28] L. Couto and A. H. Cardoso, "Erosões localizadas junto de encontros e pilares de pontes. parte i - caracterização da situação de referência," *Recursos Hídricos*, vol. 22, no. 1, pp. 64,74, Jan. 2001. 11, 13

[29] H. Schlichting and K. Gersten, *Boundary-Layer Theory*. Springer, 2016. 12, 13

[30] F. M. White, *Fluid Mechanics*. McGraw-Hill, 2003. 12, 13, 23

[31] L. Prandtl, "Über flüssigkeitsbewegung bei sehr kleiner reibung," in *Verhandlg. III. Intern. Math. Kongr*, 1904. 12

[32] P. C. X. Ramos, "Modelação numérica do escoamento em torno de um pilar," Master's thesis, Universidade do Porto, Jun. 2012. 13

[33] A. Quintela, *Hidráulica*, 13th ed. Fundação Calouste Gulbenkian, 2014. 13

[34] *Bridge scour and stream instability countermeasures: Experience, selection and design guidance*, Federal Highway Administration, HEC-23. 3rd ed. Fort Collins, CO: FHWA, 2009. 14

[35] *Evaluating scour at bridges*, Federal Highway Administration, HEC-18. 5th ed. Fort Collins, CO: FHWA, 2012. 14

[36] Y. Yang, B. W. Melville, D. M. Sheppard, and A. Y. Shamseldin, "Clear-water local scour at skewed complex bridge piers," *Journal of Hydraulic Engineering*, vol. 144, no. 6, jun 2018. 14

[37] Y. Yang, B. W. Melville, G. H. Macky, and A. Y. Shamseldin, "Local scour at complex bridge piers in close proximity under clear-water and live-bed flow regime," *Water*, vol. 11, no. 8, p. 1530, jul 2019. 14

[38] M. G. Kleinhans, H. R. A. Jagers, E. Mosselman, and C. J. Sloff, "Bifurcation dynamics and avulsion duration in meandering rivers by one-dimensional and three-dimensional models," *Water Resources Research*, vol. 44, no. 8, aug 2008. 15

[39] D. C. Wilcox, *Turbulence modeling for CFD*. DCW Industries, Inc, 1993. 22, 24

[40] E. Lightfoot, R. Bird, and W. Stewart, *Transport Phenomena*. J. Wiley, 2002. 23

[41] *ANSYS Fluent Theory Guide (Release 19.3)*, ANSYS, Inc., 2019. 24, 25, 27, 28, 29, 30, 31, 32, 33, 34, 35, 40, 44

[42] W. van Balen, K. Blanckaert, and W. S. J. Uijttewaal, "Analysis of the role of turbulence in curved open-channel flow at different water depths by means of experiments, LES and RANS," *Journal of Turbulence*, vol. 11, p. N12, jan 2010. 25

[43] B. Launder and D. Spalding, "The numerical computation of turbulent flows," *Computer Methods in Applied Mechanics and Engineering*, vol. 3, no. 2, pp. 269–289, mar 1974. 25, 29

[44] *Pointwise User Manual*, Cadence Design Systems, Inc., 2011. 35, 40, 41

[45] J. J. Mcguirk and W. Rodi, "A depth-averaged mathematical model for the near field of side discharges into open-channel flow," *Journal of Fluid Mechanics*, vol. 86, no. 4, pp. 761–781, jun 1978. 38

[46] H. Kobus, *Hydraulic Modeling*. German Association for Water Resources and Land Improvement, 1980. 40

[47] R. Martins, Ed., *Recent Advances in Hydraulic Physical Modelling*. Springer Netherlands, 1989. 40

[48] C. Santos, C. Fael, and J. Martín-Vide, "Numerical analysis of the ebro river meander flow field, upstream to the pavilion-bridge," in *6th IAHR Europe Congress*, 2021, pp. 133,134. 47

[49] Z. Sylvester, P. Durkin, and J. A. Covault, "High curvatures drive river meandering," *Geology*, vol. 47, no. 3, pp. 263–266, feb 2019. 47

[50] K. Blanckaert and H. J. de Vriend, "Meander dynamics: A nonlinear model without curvature restrictions for flow in open-channel bends," *Journal of Geophysical Research*, vol. 115, no. F4, oct 2010. 50

[51] J. Zeng, G. Constantinescu, and L. Weber, "A 3d non-hydrostatic model to predict flow and sediment transport in loose-bed channel bends," *Journal of Hydraulic Research*,

vol. 46, no. 3, pp. 356–372, may 2008. 50

[52] M. Koken, G. Constantinescu, and K. Blanckaert, “Hydrodynamic processes, sediment erosion mechanisms, and reynolds-number-induced scale effects in an open channel bend of strong curvature with flat bathymetry,” *Journal of Geophysical Research: Earth Surface*, vol. 118, no. 4, pp. 2308–2324, nov 2013. 52

[53] J. P. Martín-Vide, C. M. S. Fael, F. Núñez-González, C. Ferrer-Boix, F. Carrera, and F.-J. Seyas, “La audacia del pabellón puente en el río ebro (expo 2008): consecuencia en erosión fluvial y exigencias de protección y auscultación,” *Revista de Obras Públicas*, vol. 156, no. 3497, pp. 53,68, Mar. 2009. 52, 53, 55, 58

Appendix A

Published Works

Case Study

A Large Bridge Pier in an Alluvial Channel: Local Scour versus Morphological Effects and the Role of Physical Models

Juan P. Martín-Vide[1]; Cristina M. S. Fael[2]; Francisco Núñez-González[3]; Carles Ferrer-Boix[4]; César A. V. Santos[5]; Arnau Prats-Puntí[6]; and Victor Chavarrias[7]

Abstract: The large pier of an emblematic bridge built in 2008 in the Ebro River (Zaragoza, Spain) obstructs the flow in high floods. Clear-water scour experiments in a scale model were conducted to anticipate maximum local scour depths and design riprap protections. These proved to be effective during a large flood event in 2015, but bed aggradation under the left bridge span and deep scour under the right one, not mirroring the bed deformation observed in the model, raised concerns about the bridge safety. The effects of the protected pier on the changes in the aftermath of the 2015 flood are discussed. It is shown that a large meander upstream generated an imbalance in the spanwise bedload distribution, leading to sedimentation on the left and contraction scour on the right. The paper argues for the need to take into account the effects of large piers on river morphology at the bridge planning phase. The case study shows that using a clear-water model to design the riprap protection is adequate, but more importantly, that the fluvial processes during a flood could only be studied with a live-bed model with geometrical detail of the full river reach, namely, the upstream meander. **DOI: 10.1061/(ASCE)HY.1943-7900.0001993.**

Author keywords: Local scour; Large pier; Physical model; Model-prototype comparison; Scour and fill; Live-bed tests; Clear-water tests; Riprap; Secondary currents; Bifurcation.

Introduction

It is widely known that many river bridge failures are due to foundation scouring, especially at areas of flooding. In the case of an unusual bridge pier, it is recommended to resort to physical modeling in order to assess scouring risks and provide countermeasures to increase bridge safety (FHWA 2009, 2012). Although the practice of scale models for river problems is well established (ASCE 2000), it is not free of difficulties. Firstly, most of the time it is not possible to scale down the riverbed material to the same scale of the bridge (the geometrical scale) due to their disparate sizes. Furthermore, mobile bed models with sediment transport, as in most alluvial rivers, are difficult to carry out, to set their appropriate boundary conditions (e.g., amount and crosswise distribution of sediment feed), and to interpret their results. That is why the aforementioned manuals recommend turning to clear-water models (with no sediment feed).

Thanks to the amount of research in the twentieth century (summarized in Melville and Coleman 2000), we know that the long-term local scour depth at a bridge pier is maximum when flow velocity equals critical velocity for sediment entrainment (the threshold). This fact led to the common practice of running clear-water models under the flow velocity for the threshold conditions of sediment entrainment, by selecting an appropriate particle size in the model bed, thus maximizing local scour and providing countermeasures on the safe side.

Through new experiments, our understanding of (1) the scale effects at bridge pier scour (Link et al. 2019), (2) the effects of vorticity (Ettema et al. 2006), and (3) those caused by large flow intensities attained in experiments with lightweight material (Ettmer et al. 2015) has improved. Two more research topics are large piers compared to bed material size (Sheppard et al. 2004) and the combination of scouring mechanisms in the so-called complex piers, i.e., piers composed of several piles for deep foundation and a pile cap, apart from the pier itself (Moreno et al. 2016a, b). In these two latter cases, a discrepancy between experimental results in clear-water and live-bed (sediment transport) conditions has been observed (Yang et al. 2018, 2019), questioning clear-water tests at threshold conditions in bridge models. However, case studies that

[1]Professor, Dept. of Civil and Environmental Engineering, Technical Univ. of Catalonia, Jordi Girona 1-3, D1, Barcelona 08034 08034, Spain (corresponding author). ORCID: https://orcid.org/0000-0002-3914-615X. Email: juan.pedro.martin@upc.edu

[2]Assistant Professor, Dept. of Civil Engineering and Architecture, Universidade da Beira Interior, Centre of Materials and Building Technologies (CMADE-UBI), Rua Marquês d'Ávila e Bolama, Covilhã 6201-001, Portugal. ORCID: https://orcid.org/0000-0002-6943-6957. Email: cfael@ubi.pt

[3]Research Associate, Leichtweiβ-Institute for Hydraulic Engineering, Technical Univ. of Braunschweig, Beethovenstraße 51a, Braunschweig D-38106, Germany. Email: f.nunez-gonzalez@tu-braunschweig.de

[4]Assistant Professor, Dept. of Graphic and Design Engineering, Serra-Húnter fellow, Eduard Maristany, 16, Barcelona 08019, Spain. Email: carles.ferrer@upc.edu

[5]Master's Student, Universidade da Beira Interior, Centre of Materials and Building Technologies (CMADE-UBI), Rua Marquês d'Ávila e Bolama, Covilhã 6201-001, Portugal. ORCID: https://orcid.org/0000-0001-6631-8378. Email: cesarsantos50@icloud.com

[6]Ph.D. Student, Dept. of Civil and Environmental Engineering, Technical Univ. of Catalonia, Jordi Girona 1-3, D1, Barcelona 08034, Spain. Email: arnau.prats@upc.edu

[7]Researcher, Deltares, Boussinesqweg 1, 2629 HV Delft, The Netherlands. ORCID: https://orcid.org/0000-0003-3218-6391. Email: victor.chavarrias@deltares.nl

Note. This manuscript was submitted on April 3, 2021; approved on March 16, 2022; published online on June 14, 2022. Discussion period open until November 14, 2022; separate discussions must be submitted for individual papers. This paper is part of the ***Journal of Hydraulic Engineering***, © ASCE, ISSN 0733-9429.

compare scale models with their prototype behavior are lacking in the literature, with the exception of some forensic studies of bridge failures carried out with field and laboratory work (ASCE 1999).

The present case study deals with an extremely large and complex bridge pier. Because its shape and size were challenging, we resorted to a physical model. Concerns about local scour appeared only when the bridge was already in construction and had to be opened in a very short time. Typically, the clear-water model emphasized bridge safety by providing protection against local scour.

However, important morphological effects around the bridge appeared in surveys with the bridge already in service. Comparison of nature (surveys) and the model showed in retrospect the flaw of disregarding the impact of the pier on the river morphology at the planning phase, apart from protecting it against local scour. This is the point this case study tries to make.

Study Site and Bridge Case Study

An international exhibition was held in June 2008 on the plains of the largest Spanish River Ebro, right besides Zaragoza, where it drains a basin of ~40,000 km^2 with a mean flow rate of 250 m^3/s, a water depth at annual flood of ~6–7 m, and mean bed slope of $\sim 2 \times 10^{-4}$ (subcritical flow). A covered bridge was commissioned for that exhibition, becoming a city landmark (Fig. 1). The designer placed two abutments beyond the main channel banks and one large pier on a small bar within the alluvial channel close to the left bank. The bar elevation is 3.6 m above the right and left surrounding river arms (it becomes an island at low flow).

The bridge is larger than usual because the pier and the pile cap are coated by a goblet-like architectural metallic covering to smoothly connect the foundation to the bridge deck (Fig. 1). This produces a hindrance to the flow because it obstructs 1/3 of the width (80 m out of 240 m) at the 500-year flood water surface elevation (bank full plus dikes, discharge 5,222 m^3/s, water depth $\approx$ 10 m) and 1/6 of the width at the bed elevation (28 m out of 170 m). The obstruction tapers downward so that more scour is expected than in prismatic piers (Breusers and Raudkivi 1991). In addition, the bridge stands skewed with respect to the streamwise river flow direction.

The pier foundation consists of 10 piles with a diameter of 2 m, which are driven through the alluvium even deeper than 60 m. The load-bearing capacity of the foundation depends on the friction with the surrounding alluvial material. If local scour deprives of friction more than 6 m of depth, the bridge foundation will no longer be safe. In contrast, an estimation of the local scour depth with HEC-18 (FHWA 2012) for the 500-year flood, by averaging the goblet-like width, is 22.2 m.

Fig. 1. View from the downstream left bank looking upstream under a flow of 1,500 m^3/s on June 4, 2008; see the goblet-like covering.

Physical Model for Local Scour Protection

The physical model was aimed at knowing the depth and extent of the local scour so that a riprap apron could be provided as a countermeasure. It was designed at an undistorted 62.5 scale to preserve flow patterns and bed deformation produced by the pier, and fixed bed except for a recess to install the pier and piles. Different uniform sands in the recess box were tested without the bridge to select a grain size about to be entrained by the design discharge. For the practical technique to select the right sand see Fael (2007). The clear-water Froude model used a 4-m-wide, 28-m-long, and 1-m-high straight flume with the halfway recess 3 m long, 0.65 m deep, and its full width, located at Universidade da Beira Interior (UBI) (Fael 2007).

The Ebro River bed is composed of a median-to-coarse gravel, with median size $D_{50} = 18$ mm and lognormal standard deviation $\sigma_D = \sqrt{[D_{84}/D_{16}]} = 3.83$, while the sand selected for the model was $D_{50} = 1.28$ mm and $\sigma_D = 1.47$. The gravel bed would scale down to a 0.29-mm fine sand in the model, where below 0.7 mm would be forming ripples (Dey 2014), producing a scale effect. Replaced by this 1.28-mm coarse sand, there is a grainsize distortion of 4.5, i.e., the scale for D_{50} is 14 instead of 62.5. This distortion produces negligible scale effects (Link et al. 2019). If the ratio of pier diameter to grain size is >50 (which are 54 m/18 mm = 3,000 in nature, decreasing to 0.86 m/1.28 mm = 670 in the model), the scour depth is independent of sediment size (Raudkivi 1990). If the same ratio is >100, the scour depth increases when this ratio decreases (Sheppard et al. 2004). Therefore, the scour in the model is exaggerated due to the D_{50} distortion (exaggeration). This holds at least for simple piers. At the model stage that looks for the maximum scour depth to design a protection, this exaggeration stands on the safe side. Similarly, a lower standard deviation σ_D stands also on the safe side, because armoring cannot occur in the model scour hole while still being able to happen in nature (Raudkivi 1990). Similarity conditions were also applied to the riprap, including conditions for the filter between the riprap and the alluvium.

The straight flume forced a parallel approach flow to the scale model (the skewed bridge) and downstream, which was not deemed any drawback at the time (see Fig. 2). It was argued that the road bridge located 400 m upstream and spanning 250 m from one abutment to the other ensured a parallel approach flow.

Fig. 2. Regional setting for the bridge in the Ebro River. Note the deep meander upstream (analysis resumed in section on "Ananlytical Approaches"). The road bridge was also built in 2008. [Reprinted Sistema Cartografico Nacional (2022), under Creative Commons-BY-4.0 license (https://creativecommons.org/licenses/by/4.0/).]

The approach reach was simplified to a trapezoidal cross section (Fig. 7, later). In doing so, the Froude number remained equal to 0.33, in both model and prototype, in which mean water depth and mean velocity for the design discharge are 9.7 m and 3.2 m/s, respectively.

After a scour test lasting 48 h (model time), with a steady design discharge of 5,222 m^3/s in the river, the maximum scour depth deprived 20.3 m of the piles' depth (Fig. 3) (17.5 m from the bottom in the test). Mathematical estimates of the equilibrium scour if time approaches infinity increase this by ~8%, depending on the time evolution equation fitted to our experimental data. The right bridge span in the recess remained mostly unchanged (no general scour), while the left one exhibited a huge deformation. This was made of two hollows at the left and right side of the pier, with slightly divergent thalwegs, yet their bisector line was roughly parallel to the main flow. The hollows issued together from the piling area but separated downstream by a small crest progressing further downstream, beyond the recess, like a mound. The left hollow was larger. The total scoured surface area was 10,150 m^2 and the total volume 43,500 m^3 (prototype).

Tests were conducted afterward to design a riprap apron (a blanket) as a countermeasure. The criterion for riprap success was that the apron width lost should be less than 50% of the design width (Fael 2007). The optimal particle weight resulted in 600 kg, while the apron extent around the pier resulted in a fringe 9 m wide on both the upstream and downstream sides and 21 m wide on the sides close to the left bank and close to channel center. The toe of the left bank was also protected with the same riprap all the way down to the recess edge. The final test to check the apron stability used the river topography and not the trapezoidal cross section anymore: two river arms, left and right, with the bar top at the pile cap elevation.

The 33-h test produces a new large bed deformation (Fig. 4). The result of protecting the pier is to prevent any scour around it (neither at the rear stagnation area). The pair of left and right hollows remain yet moved to their respective sides. Their scour

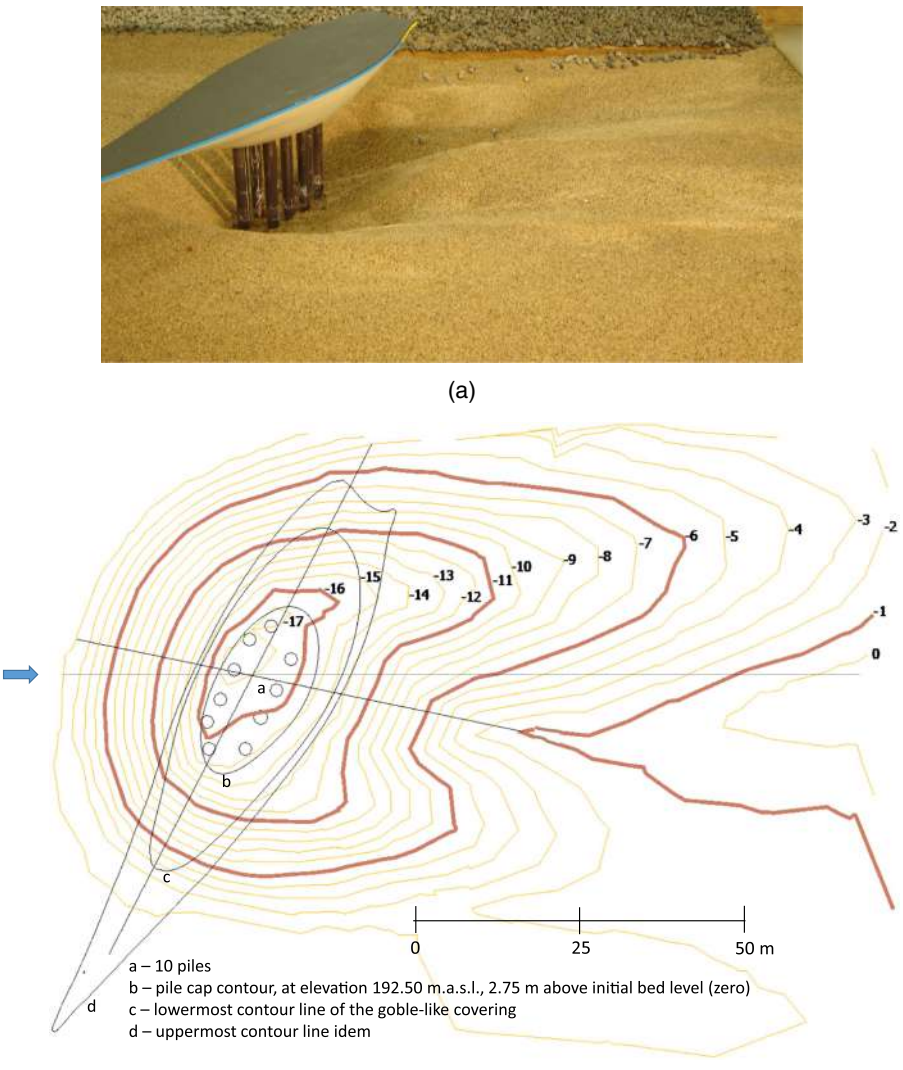

Fig. 3. (a) Photograph of the model after the test, flow from left to right; and (b) survey of the scour hole in the recess box; contour levels refer to the original bed [zero = 189.75 m above sea level (a.s.l.)]; all dimensions for the prototype. The 10 piles, used for cross-reference to other figures, the pile cap, and the uppermost and lowermost contour lines of the goblet-like covering are drawn. The three axes (flow direction, pier axis, and bisector ridge between hollows) are added to help with interpretation.

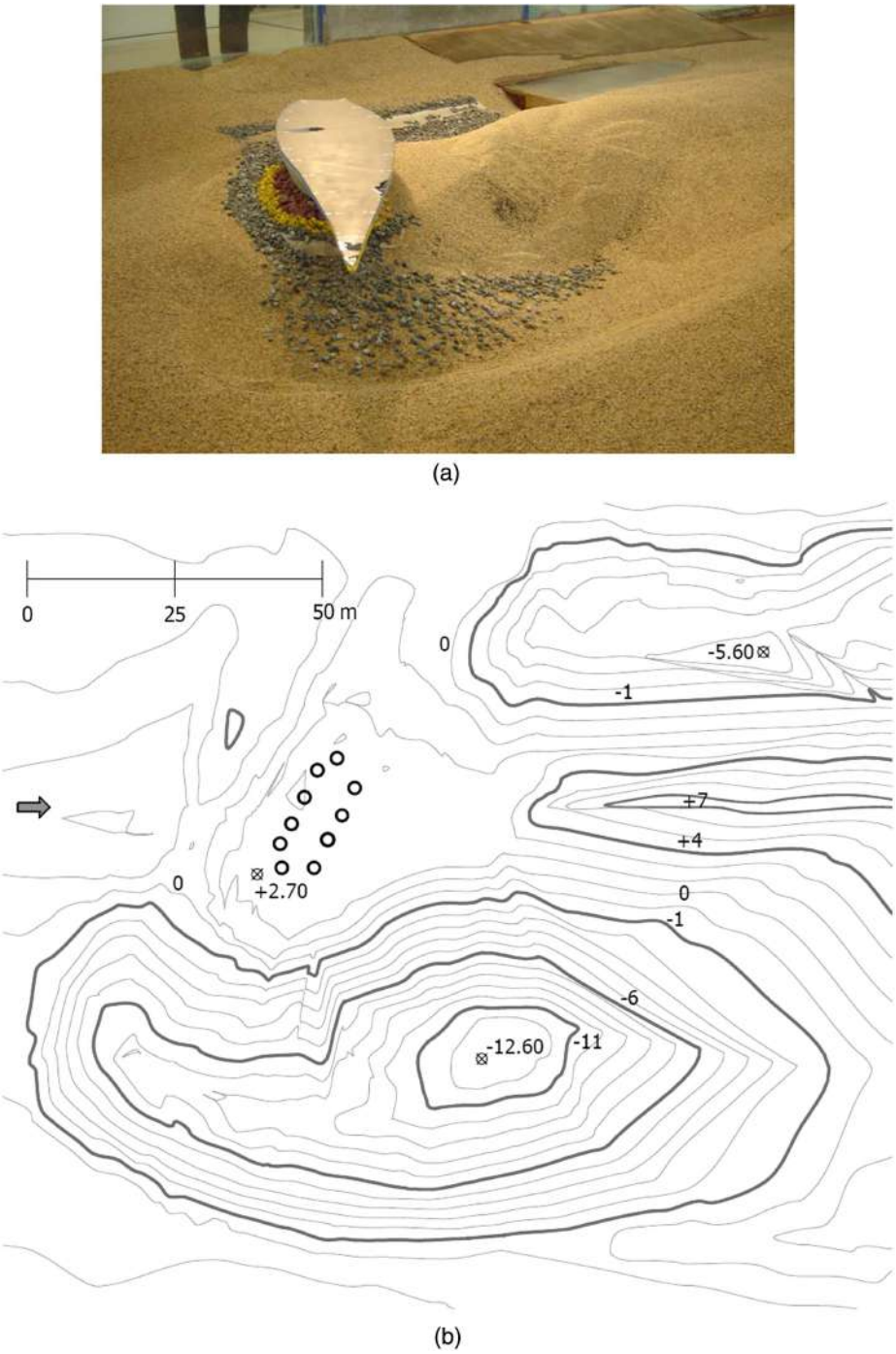

Fig. 4. (a) Photograph of the model with the designed riprap blanket after the test. Flow from left to right. Gray particles making 50% of the total blanket width are the only lost, rolling down to the holes (design criterion for riprap). (b) Bed survey of this test, contour levels refer to zero = 189.75 m a.s.l as in Fig. 3, despite an initial bed at +2.75 m in the bar, reaching the pile cap; all dimensions for the prototype. Piles are drawn for cross-reference with Figs. 3–6.

depths are still large. The right one invades the right bridge span and develops a 15.3-m-deep scour hole measured from the bar top (−12.60 m from zero) with a scoured area of 6,800 m^2 and a scoured volume of 33,000 m^3 (measured from zero). Some riprap particles roll down the slopes of the right hole, which are even steeper than without protection. The left hole reaches −5.60 m and becomes more densely lined with riprap particles, mostly coming from the left bank blanket. The edge of the recess gets a little uncovered, on this left side only. Despite particle loss by rolling down, the blanket withstands according to our criterion. The crest separating the two hollows reaches 7.5 m above zero, much taller than what we obtained in the scour test, and it lengthens beyond the recess as a much bigger mound. All this material comes from the holes. A set of dunes develops on the mound slope, visible in Fig. 4(a), showing the main direction of particles scoured out of the right hole and climbing up the mound.

In conclusion, the scouring due to the large pier seems to have been transferred toward the sides (the channel center area especially). The bed relief is deemed to be part of a delicate system molded by the flow in the sense that any digging or filling of one feature (mound, holes, etc.) would produce a deformation elsewhere in the system.

Behavior of the Bridge and Channel Area in Nature

A new concern arose after a major flood on March 2, 2015, which neither dismantled the riprap nor scoured the pier. Major morphological changes around the bridge were reported when the flood receded (Fig. 5). The approach channel on the left that includes

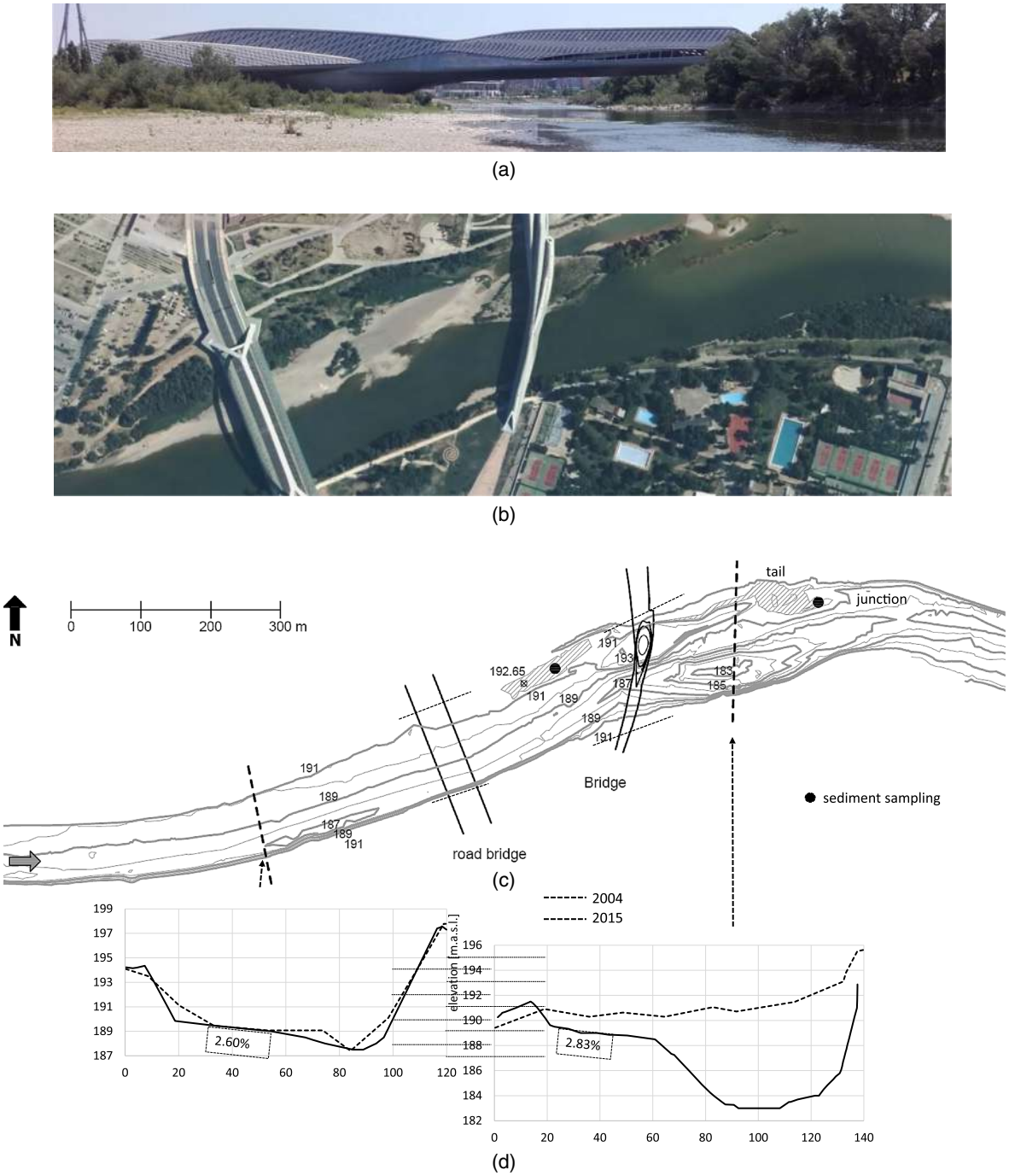

Fig. 5. (a) Bridge in May 2017 (in low flow), seen from the channel at the road bridge upstream; see the left arm filled with sediment, already with vegetation (image by authors); (b) image of May 2015 after the March 2015 flood; see the upstream aggradation attached to the small bar, streamlined to place the bridge pier [reprinted Sistema Cartografico Nacional (2022), under Creative Commons-BY-4.0 license (https://creativecommons.org/licenses/by/4.0/)]; (c) survey around the bridge in June 2015 (absolute elevations a.s.l.); the shaded areas are the most conspicuous filled zones (the one upstream is not fully surveyed, the one downstream is lower); see sampling points for grain size tests; the fine dashed lines at banks are used in the discussion; and (d) two cross sections dated 2004 (no bridge) and 2015 (after the flood) for comparison.

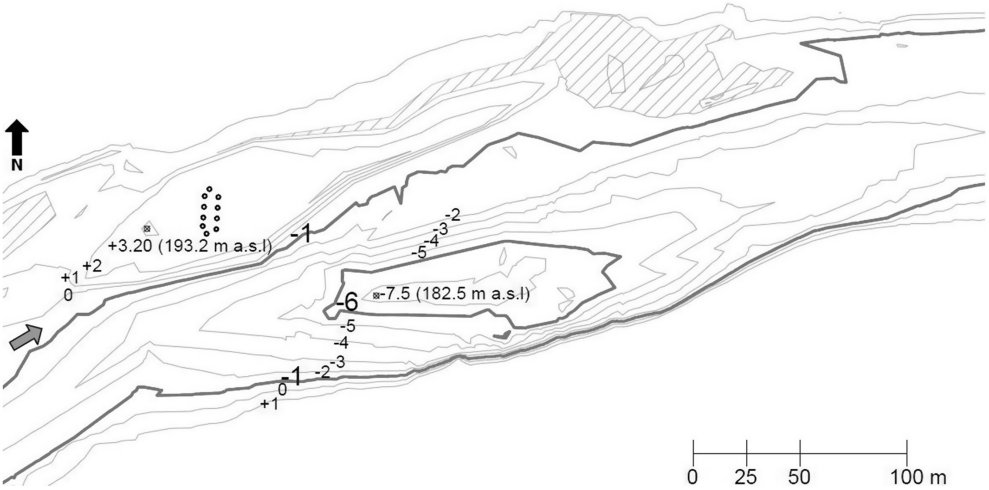

Fig. 6. Zoom of the survey around the bridge in Fig. 5. For the sake of comparison, positive or negative contour lines refer to the closest elevation to zero in Figs. 3 and 4 (189.75), which herein is 190.0. Piles are drawn to cross-reference to previous figures.

Table 1. Floods larger than 1,500 m^3/s in the period 2008–2015

Date	Peak discharge (m^3/s)	Number of days discharge >1,500 m^3/s around date
1/23/2013	1,755	3
3/7/2014	1,554	1
2/4/2015	1,800	2
3/2/2015	2,448	8

the left bridge span and its tailwater area were unevenly filled with alluvial material. A long mound (~350 m) attached to the left bank emerged with a shape similar to the original bar and with a top elevation 0.15 m above the bar top. Most of the 3.6-m-deep river arm at the left span therefore became filled and almost blocked for subsequent low flows. The original bar expanded ~75 m in the streamwise direction [shaded area in Fig. 5(c)] like a growing tail. This was lower than the mound upstream but took up the junction area of the two arms, where the fill was ~1.10 m thick. In turn, the crest at the rear of the pier rose 0.7 m only above the bar top. Sediment samples from the center of the new mound upstream and the junction gave sizes $D_{50} = 6.6$ and 5.6 mm, respectively, finer than those known so far (with deviations $\sigma_D = 4.1$ and 6.7, poorly sorted). In addition, a bathymetrical survey in June 2015, when compared to a survey prior to 2008, discovered an 8.5-m-deep scour hole downstream of the right span (Fig. 6). It extended crosswise to half the full bed width (~95 m) and all the way down to the junction, at approximately 240 m of the bridge (Fig. 6). The scoured volume between the two surveys was 65,000 m^3.

Although the 2015 flood was its major leap, aerial photographs showed that aggradation on the left approaching channel had been occurring since 2012. Since the bridge opening in June 2008, which coincided with a 1,500-m^3/s flood, Table 1 gives the events that exceeded that particular discharge by the time of the last survey (June 2015). Thus, the March 2015 flood must have been responsible for most of the reported change. Any floods in nature and in our scale model are not commensurable (in flow and transport). If they were, the discharge in the model would be higher and last longer (Froude scales) than this flood.

The sketch of Fig. 7 is a summary of the surveys of Figs. 3–6.

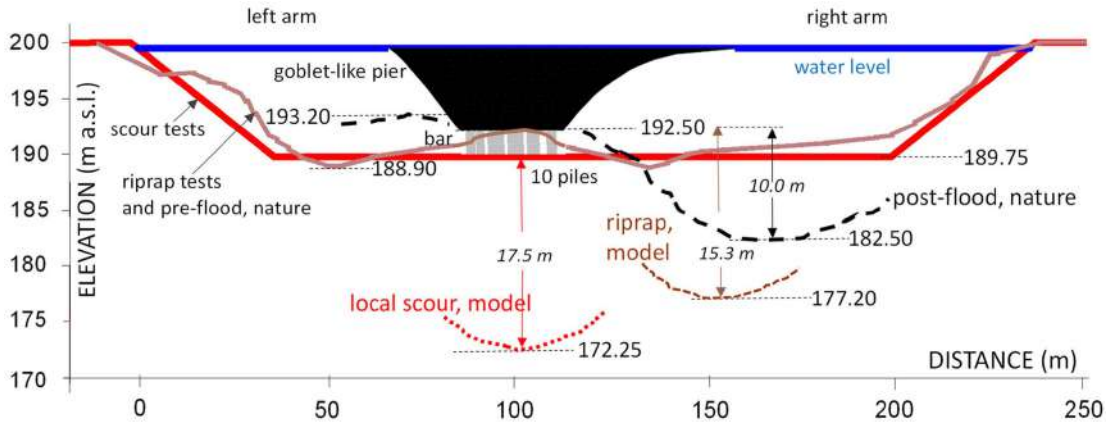

Fig. 7. Summary of selected data of Figs. 3–6. Note figure distortion. The pier is drawn projected to the cross section (trapezoidal in local scour test; with relief and bar in riprap tests). See zeros of reference (189.75 and 192.50 right at the piling top, respectively). See the scour depths and the extreme scour hole elevations.

Discussion

The scour and fill in nature are disturbances caused by the bridge to the otherwise stable bed. Similarly, the bridge in the model disturbs the otherwise flat, largely motionless sand in the recess. On the other hand, the phenomena in nature and in the model are very different, because of some real processes that are absent in the laboratory, mainly bed load transport and the approach flow structure. In comparison, the departure from similarity that occurred by exaggerating scour depth due to the size and sorting of the selected sand is a minor issue. If nature and our model were commensurable, scour depths with riprap (15.3 m model >10.0 m nature) would rather reflect a higher discharge and a longer duration in the model. It would not be worth trying to rank the influence of these factors (size, sorting, peak flow, time) given the limited information at hand (one test and one flood).

Note that the river channel is essentially stable upstream of the bridge. The cross section close to the meander outlet (Fig. 5) had not changed from 2004 until 2015, after the flood. Incidentally, the channel shape there (thalweg tipped to the outer bank, 2.6% transverse bed slope) reveals a permanent effect of the meander curvature (point resumed in the next section). Therefore, the bridge region is a locally disturbed area in a stable river, the fill at the left is the local aggradation, and the scour at the right is the local degradation.

The mound created by the 2015 flood can be regarded as a point bar at the meander outlet, similar to other point bars visible in mid-twentieth-century aerial photographs. Those bars were dynamic in the sense of capturing and issuing bed particles yet changing little in size. The small bar bearing the pier is a remnant of such bars, which do not form anymore since 2008.

Upstream migrating aggradation in bridges is indicative of instability caused by local reduction of sediment transport capacity (Johnson et al. 2001). A raised backwater may also contribute to aggradation. The bridge effect in the observed aggradation may be related to the large pier acting as a kind of bifurcation, i.e., flow and sediment load had to split in two. If so, the load directed to the left arm (its supply) must have exceeded its transport capacity (by flow going to the left) simply because the arm got aggraded. Conversely, the load directed to the right was in shortage for the transport capacity of flow to the right because the arm got degraded. The reasons why sediment load and flow were not evenly distributed across the left and right arms are tentatively explained in the next section.

The lack of sand feeding prevented this mechanism in the model. The flow in the model that split in two was reflected in the size of the hollows. The left one was much smaller with protection than without (Figs. 3 and 4). Besides, this was overwhelmed in nature for sure by the aggrading trend of the left arm. It seems that the aggradation and the degradation trends sustain each other, as the left aggradation diverts flow to the right arm, sustaining scouring in it, while the increased conveyance there reduces flow (and velocity) on the left arm, thus sustaining filling in it. However, the filling of the junction area downstream may also clog the left arm outlet in a sort of cul-de-sac, raising backwater and so promoting aggradation.

The completion of the left arm aggradation would eventually reduce the bed width from 170 m (left + right arms) to 95 m (right arm) all the way down to the junction (along 240 m). Johnson et al. (2001) observed that aggradation at one span can lead to contraction scour at the remaining spans. In fact, the scour of the right arm in nature looks like a contraction scour rather than a local scour, because of two features: (1) the hole is almost as long as the contraction, much longer than the model hole, with the deepest point farther away from the pier, and (2) the total scoured volume is 65,000 m^3 (nature) > 33,000 m^3 (model), suggesting a broader process than just the local scour transferred to the side. Based on clear-water tests, the formula for long-term contraction scour (Vanoni 1975) for a 170- to 95-m width reduction and a mean depth of 9.7 m produces $9.7 \times [(170/95)^{2/3} — 1] = 4.6$ m < 10.0 m (nature). Then, the contraction seems to have not fully developed or not to be the sole scour mechanism. A transferred local scour hole may have dominated at the beginning of the flood. Then, as the left arm was getting filled, this hole may have lengthened and deepened due to the flow increase on the right arm and the associated contraction scour. This process may be called self-contraction scour.

The mound built up on the bar ridge by the scoured material was 0.7 m high in nature, very far from 6 to 7.5 m in the model. This suggests that the ability to take away particles in nature (but only to pile them up locally in a mound of the model) disturbs any similarity of the large bed forms produced by the bridge. Sand at the threshold of entrainment under the design discharge maximizes local scour but restricts mobility, due to its exaggerated size, in other places such as the mounds (see also Oliveto and Hager 2014).

Analytical Approaches: Secondary Flow and Bifurcation

We outline an explanation for the bridge scour and fill based on a simple analysis within the practitioner's reach. First, consider a river bifurcation triggered by a large obstacle on an alluvial channel. Bifurcations are known to attain a highly asymmetrical division of discharge and sediment after time. The presence of a crossflow component (v, inverse in sign at surface and bottom) perpendicular to the main flow (u), so that the velocity vector deviates an angle $\alpha = \text{arctg}\,[v/u]$, causes an unbalanced division of bed material load (Fig. 8). The bedload angle may be greater than the flow angle α at the bed (Kleinhans et al. 2008).

The analysis aims at ascertaining whether the upstream meander (see Fig. 2) may introduce some crossflow in the reach between the road bridge and our bridge. If so, bifurcation dynamics can explain an imbalance in bedload, probably leading to the bridge scour and fill. To this aim, two computational fluid dynamics (CFD) models have been applied to the meander (see Supplemental Materials). The first one was run using Delft3D flexible mesh (Deltares 2021) in three-dimensional (3D) mode featuring 10 equally spaced layers in the vertical direction. Flow is steady over a trapezoidal geometry in a fixed bed. Long and cross bed slopes, roughness, and plan centerline are selected according to nature. The main (u) and crossflow (v) components at the meander outlet, i.e., the road bridge, are depicted in Fig. 9 for 2,000 m^3/s. As expected, velocities u are significantly higher (>3.5 m/s) on the right (outer) than on the left (2.5 m/s, inner region). Velocities v are small (below 4 cm/s) but not null, and are directed toward the inner region in most of cross-sectional cells, especially near the bed. Two more outputs of this model are (1) crossflow velocity (v) at free surface throughout the meander centerline, to be used later, and (2) the long and cross-free surface slopes, to be imposed to the second model (that uses the same plan) and that are the cross section and long and cross bed slopes of the first model.

The second model was run using ANSYS Fluent, fully 3D with a single phase (water only). The upper boundary of the flow domain is a rigid lid (slip condition, i.e., no friction acting on it). This assumption results in accurate predictions of flow field if the surface superelevation is less than 10% of water depth and if the Froude number is less than 0.5 (ours is 0.3) (Constantinescu

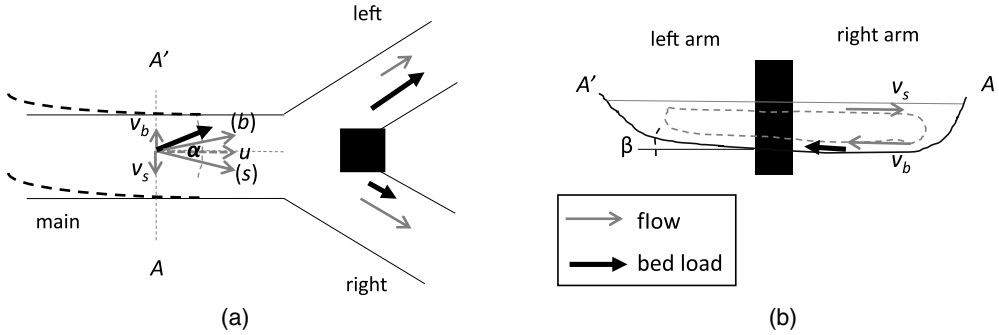

Fig. 8. (a) Scheme of a bifurcation in plan; velocity components $(v,\ u)$ form angle α, different at the surface (s) and bed (b); and (b) scheme of cross section A-A', see slope β.

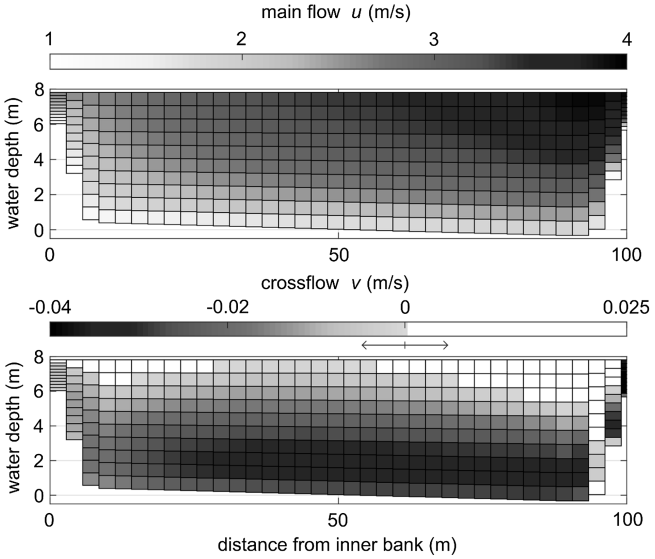

Fig. 9. Results of Delft3D-Flow flexible mesh at the meander outlet (road bridge): main flow u and crossflow v in meters per second. Bank slopes are a disruption in the discretization. Uniform eddy diffusivity is 0.1 m^2/s in horizontal and 5×10^{-5} m^2/s in vertical.

et al. 2011). Fig. 10 is a selection of cross velocities (v) at three cross sections: (1) close to the meander apex to check for high secondary flow; (2) close to the meander outlet; and (3) at the outlet. Fig. 10 shows how the essentially cross-circulatory velocities at 1 turn into a net flow toward the inner region at 3.

We will now test the simplest description of the growth and decay of velocity v, evaluated at the water surface along the channel centerline, which reads (Chang 1984, 1988; Odgaard 1986a, b, all following Rozovskii 1957)

$$u\frac{\partial v}{\partial s} = \frac{u^2}{r} - gS_r + \frac{\partial}{\partial z}\left(\varepsilon\frac{\partial v}{\partial z}\right) \tag{1}$$

under the following assumptions: (1) $u > v, w$; (2) width/depth ratio >5; (3) r, radius of curvature ≫ width; (4) linear vertical distribution of v; (5) parabolic vertical distribution of eddy viscosity (ε); and (6) turbulent shear stress related to the friction factor. The last terms in Eq. (1) are radial water surface slope (S_r) and turbulent shear.

Fig. 11 plots real data of cross bed slope, $tg\,(\beta)$ (see Fig. 8 for β), at seven meander river cross sections dated 1996 (Locations 1–7). This $tg\,(\beta)$ is a surrogate of the crossflow v. It reaches a maximum of ~6.5% at halfway and of ~2% close to the outlet (similar to 2.6% in 2004, Fig. 5). Two simulations are compared to $tg\,(\beta)$ in Fig. 11: (1) velocities v that were obtained by the first model, and (2) the same v, by the straightforward solution of Eq. (1) by Chang (1988), in which a reference flow is taken at the meander halfway (Fig. 2) and the plan curvature $(c = 1/r)$ is discretized along the arc (s) from 0 to 2,500 m (also plotted in Fig. 11). The Chang solution betrays very closely the pulses of the planform curvature. In contrast, wherever planform curvature is almost null (e.g., at $s =$ 1,300–1,500 m), v decays exponentially. Peak values of c raise v by overcoming a permanent underlying decay trend. The first model agrees better with $tg\,(\beta)$ than the solution of Eq. (1). The two simulations remarkably agree in maximum cross velocities $v \approx$ 0.46–0.54 m/s but differ significantly in the value of v at the meander outlet [Eq. (1) exaggerates it]. However, this difference depends on the first model diffusivity.

The fate of the crossflow downstream of the meander outlet is to decay exponentially, but requires some distance. Fig. 9 demonstrates that v is small but still substantial at the road bridge, some 400 m upstream of the bridge. According to Fig. 11, the first model velocities are $v = 0.030$ m/s and $u = 2.1$ m/s at this position, i.e., a deviation $v/u = 0.014$ or an angle $\alpha \approx 1°$ [with Eq. (1) it is $\approx 5°$].

Another hint for the crossflow and the bifurcation as the mechanisms causing the fill of the left area is the grain size at the mound and the junction at elevations well above the original bed (sampling points in Fig. 5), which are finer than the bulk of the riverbed alluvial material. Flow may lift particles from the bed that the crossflow component deviates to the side. The finer the particles, the more likely their entrainment.

Apart from backwater effects and secondary flow approaching the bifurcation, a third reason for the imbalance is a slight divergence of the left bank from the right one in the region between bridges. A careful check of the top of the banks for ~2,000 m^3/s shows a 2° outward angle of the left boundary while the right one is tangential to the meander right bank [Figs. 5(b and c)]. ANSYS Fluent is applied to this new, slightly widening geometry. Vertical distributions of v at the centerline are compared in Fig. 12 with those plotted in Fig. 10. While they are equal at Section 1 (close to the apex), the net cross flow toward the inner bank is more intense in the widening case in both Sections 2 and 3, than in the constant width case. This would exacerbate the imbalance effect at the bifurcation.

It must be emphasized that the use of CFD in this section is ancillary to the discussion.

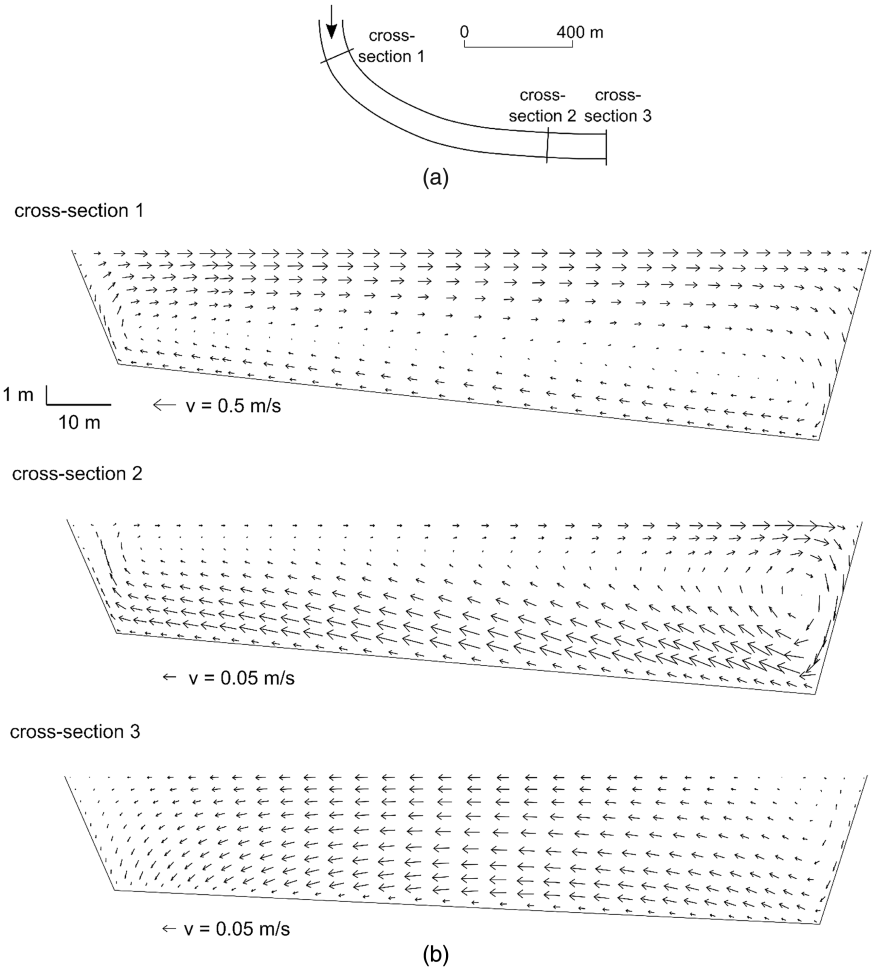

Fig. 10. Results of ANSYS Fluent: (a) downstream half meander; and (b) cross velocities v at Sections 1–3 of the downstream half meander. Note the different graphic scales.

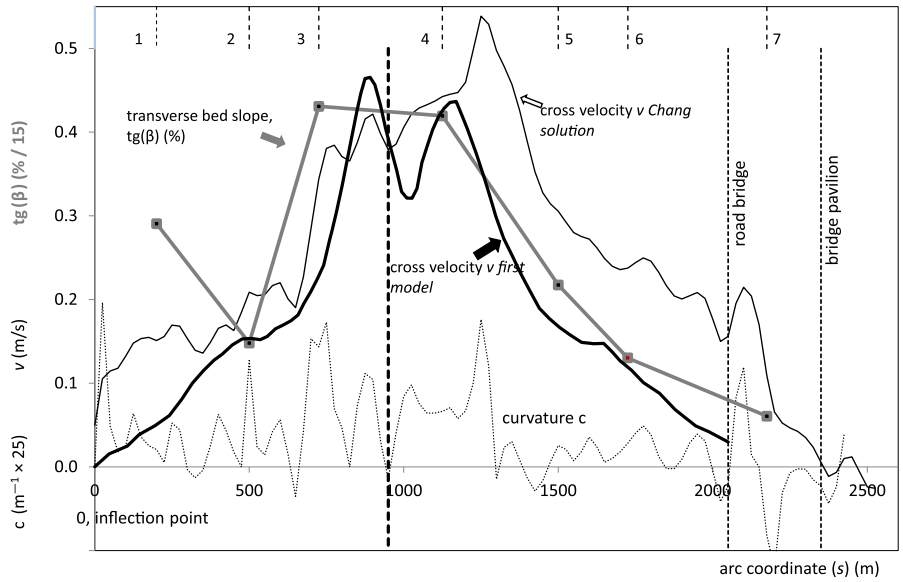

Fig. 11. Graph of computed cross velocity (v) in two ways: following Eq. (1) and first model. These computations are compared with cross bed slopes $tg\,(\beta)$ at seven cross sections. Measured plan curvature is added. Resolution of plan intervals and computations with Eq. (1) is 25 m (more than 100 points). Note that particular scales hold for c and $tg\,(\beta)$ for ease of interpretation.

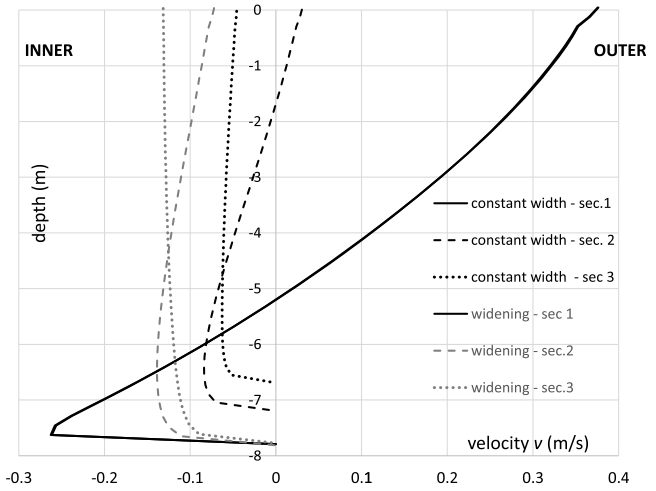

Fig. 12. Comparison of two applications of ANSYS Fluent for constant width (Fig. 10) and a 2°-angle separation of the left bank: vertical distributions of v at the centerline. Cross sections 1–3 are as in Fig. 10.

Conclusions and Perspectives

The physical model to investigate the local scour and provide a riprap protection to the bridge excluded the role of sediment transport, as customary. According to literature, this role was negligible. Therefore, it was implicit that any bed deformation eventually caused by sediment transport was also negligible. This kind of idealized models that are very well suited to design bridge protections do not fully match their prototypes (rigorously speaking), because flow and transport conditions in rivers are not commensurable with those in the respective models.

This drawback is not important when the pier is small compared to the channel size, but our bridge has proven to be too large for that. The March 2015 flood revealed that the bridge caused a large bed deformation, filling the left area and scouring the right one. Therefore, the scouring potential of a subsequent flood has changed since March 2015, because new flow conditions will prevail and so the effectiveness of the installed riprap protection has changed as well (for better or for worse). We do not know to what extent the bridge is currently safe, which is paradoxical since bridge safety was the main concern from the very beginning.

The model showed that effective protection of the pier moved the local scour aside from it. This may have provided clues to anticipate the postflood morphology, despite the fact that bed deformation (holes and mounds, depending on each other) does not keep similarity with nature. The intentional use of a conventional grain size in the model (larger than due), in order to maximize local scour, restricts grain mobility and promotes the mound growth (more than due), instead of ejecting grains away. The success of the riprap blanket (apron) in the model depended on its hole, but very different hole dimensions prevail in nature.

Our analysis has shown that the large scour and fill is due to an imbalance in sediment load versus flow rate (capacity load) with opposite signs in the left and right arms. As a consequence, a contraction scour on the right arm was superimposed to the local scour aside from the pier. The two scour mechanisms mutually interact.

The large bed deformation is intrinsic to the obstacle as long as it acts as a flow bifurcation on one side, and intrinsic to the deep meander upstream as long as it introduces some crossflow when approaching the bridge. As a chain of two links, crossflow is necessary first, because the imbalance would not occur under a perfectly parallel flow. In turn, a bifurcation that amplifies any preference for either left or right arm would only grow if there is some bed material transport able to fill or scour. Then, it is suspected that the lack of sediment transport is more important than the lack of flow parallelism in not activating the chain (cross flow and bifurcation) producing the bed deformation in the model.

Therefore, the model could have simulated the flow coming from a meander by establishing accordingly the approach conditions. However, we suspect that this effort was probably in vain, if at the same time it was kept running in clear-water, as customary and efficiently enough to study maximum local scour. After correcting the upstream boundary condition, a crossflow with $\alpha = 1°–5°$ would have produced little change in the local scour and riprap protection (the pier is already skewed to the flow $\gg 1° - 5°$).

It is suggested for future research to check the lack of bed material load in a physical model explaining the discrepancies between model and nature in the case of a large obstacle in an alluvial channel.

Although the similarity between a live-bed model and its prototype is not free of intricacies, it will be worth turning to this kind of model for this research topic of a large obstacle in an alluvial system as a whole. A similar conclusion has been drawn for skewed complex bridge piers (Yang et al. 2018) and for complex piers in close proximity (Yang et al. 2019), where the bed deformation may change with or without sediment transport. Limitations of clear-water scale models in these cases should be kept in mind, but they should not be excluded, of course. A combination of the two would take advantage of obtaining the local scour on the safe side in clear-water models (maybe of larger size and over a small domain) and help to understand a set of processes such as the interaction between mounds and holes in live-bed models (smaller size, larger domain including a longer river reach upstream).

The final rationale is that the bridge safety may depend on the bed deformation as much as on the local scour, and our duty is to consider all the risks involved. Then, in special cases, such as large piers producing morphological changes in this case study, clear-water conditions would be justifiable but not sufficient.

On the post-2015 channel geometry, the mean discharge (250 m^3/s) flows only through the right arm. In case of a peak of 2,448 m^3/s (like the 2015 flood), the discharge would split in 24% to the left and 76% to the right (44% and 56% before 2015). In August 2018, a volume of 19,500 m^3 was removed from the left arm (depth of digging >2.5 m at some spots, surface of 22,000 m^2) and dumped into the right scour hole (scoured volume by the 2015 flood: 65,000 m^3). Apart from enabling the left arm to flow, this action is partially reestablishing the conditions in which the physical model provided a safe protection against local scour in the bridge.

Data Availability Statement

The model and prototype data (surveys) are available from the corresponding author upon reasonable request.

Acknowledgments

Thanks to the insightful, helpful comments by the Associate Editor. Thanks to the Ebro Water Authority (Marisa Moreno and Miriam Pardos) and Zaragoza Municipality (Luis Manso) for providing hydrological data and field surveys. We also thank the financial support of the FEDER-COMPETE2020 (POCI) and Portuguese

funds (Foundation for Science and Technology, IP) through project PTDC/ECI-EGS/29835/2017—POCI-01-0145-FEDER-029835.

Notation

The following symbols are used in this paper:

c = curvature of channel centerline ($=r^{-1}$);
D_m = median diameter of bed particles;
D_x = grain size of bed particles for which x% in weight is finer;
r = radius of curvature of channel centerline ($=c^{-1}$);
S_r = water surface slope along the radial coordinate;
s, z = coordinates along the channel centerline (arc coordinate) and along the vertical;
u, v, w = main flow, crossflow, and vertical flow components of velocity vector;
α = arctg $[v/u]$ = angle of deviation of velocity with respect to mainstream direction;
β = angle of the transversal bed slope in a cross section; and
$\sigma_D = \sqrt{[D_{84}/D_{16}]}$ = lognormal standard deviation of bed grain size distribution.

Supplemental Materials

Figs. S1–S3 and Tables S1 and S2 are available online in the ASCE Library (www.ascelibrary.org).

References

ASCE. 1999. *Stream stability and scour at highway bridges*. Reston, VA: ASCE.

ASCE. 2000. *Hydraulic modelling. Concepts and practice*. Reston, VA: ASCE.

Breusers, N. N. C., and A. J. Raudkivi. 1991. *Scouring. Hydraulic structures*. Rotterdam, Netherlands: A.A. Balkema.

Chang, H. H. 1984. "Regular meander path model." *J. Hydraul. Eng.* 110 (10): 1398–1411. https://doi.org/10.1061/(ASCE)0733-9429(1984)110:10(1398).

Chang, H. H. 1988. *Fluvial processes in river engineering*. New York: Wiley.

Constantinescu, G., M. Koken, and J. Zeng. 2011. "The structure of turbulent flow in an open channel bend of strong curvature with deformed bed: Insight provided by detached eddy simulation." *Water Resour. Res.* 47 (5): 1–17. https://doi.org/10.1029/2010WR010114.

Deltares. 2021. "Delft3D flexible Mesh suite 1D/2D/3D Modelling suite for integral water solutions user Manual D-Flow Flexible Mesh." Accessed May 18, 2022. https://content.oss.deltares.nl/delft3d/manuals/D-Flow_FM_User_Manual.pdf.

Dey, S. 2014. *Fluvial hydrodynamics*. Berlin: Springer.

Ettema, R., G. Kirkil, and M. Muste. 2006. "Similitude of large scale turbulence in experiments on local scour at cylinders." *J. Hydraul. Eng.* 132 (1): 33–40. https://doi.org/10.1061/(ASCE)0733-9429(2006)132:1(33).

Ettmer, B., F. Orth, and O. Link. 2015. "Live-bed scour at bridge piers in a lightweight polystyrene bed." *J. Hydraul. Eng.* 141 (9): 04015017. https://doi.org/10.1061/(ASCE)HY.1943-7900.0001025.

Fael, C. M. S. 2007. "Erosões localizadas junto de encontros de pontes e respectivas medidas de proteccção (Local sour at bridge abutments and their protection)." Ph.D. thesis, Dept. of Civil Engineering and Architecture, Universidade da Beira Interior.

FHWA (Federal Highway Administration). 2009. *Bridge scour and stream instability countermeasures: Experience, selection and design guidance, HEC-23*. 3rd ed. Fort Collins, CO: FHWA.

FHWA (Federal Highway Administration). 2012. *Evaluating scour at bridges, HEC-18*. 5th ed. Fort Collins, CO: FHWA.

Johnson, P. A., R. D. Hey, M. W. Horst, and A. J. Hess. 2001. "Aggradation at bridges." *J. Hydraul. Eng.* 127 (2): 154–157. https://doi.org/10.1061/(ASCE)0733-9429(2001)127:2(154).

Kleinhans, M. G., H. R. A. Jagers, E. Mosselman, and C. F. Sloff. 2008. "Bifurcation dynamics and avulsion duration in meandering rivers by one-dimensional and three-dimensional models." *Water Resour. Res.* 44 (8): W08454. https://doi.org/10.1029/2007WR005912.

Link, O., S. Henríquez, and B. Ettmer. 2019. "Physical scale modelling of scour around bridge piers." *J. Hydraul. Res.* 57 (2): 227–237. https://doi.org/10.1080/00221686.2018.1475428.

Melville, B. W., and S. E. Coleman. 2000. *Bridge scour*. Fort Collins, CO: Water Resources Publ.

Moreno, M., R. Maia, and L. Couto. 2016a. "Prediction of equilibrium local scour depth at complex bridge piers." *J. Hydraul. Eng.* 142 (11): 04016045. https://doi.org/10.1061/(ASCE)HY.1943-7900.0001153.

Moreno, M., R. Maia, L. Couto, and A. Cardoso. 2016b. "Subtraction approach to experimentally assess the contribution of the complex pier components to the local scour depth." *J. Hydraul. Eng.* 143 (4): 06016030. https://doi.org/10.1061/(ASCE)HY.1943-7900.0001270.

Odgaard, J. 1986a. "Meander flow model. I. Development." *J. Hydraul. Eng.* 112 (12): 1117–1135. https://doi.org/10.1061/(ASCE)0733-9429(1986)112:12(1117.

Odgaard, J. 1986b. "Meander flow model. II. Applications." *J. Hydraul. Eng.* 112 (12): 1137–1149. https://doi.org/10.1061/(ASCE)0733-9429(1986)112:12(1137.

Oliveto, G., and W. H. Hager. 2014. "Morphological evolution of dune-like bed forms generated by bridge scour." *J. Hydraul. Eng.* 140 (5): 06014009. https://doi.org/10.1061/(ASCE)HY.1943-7900.0000853.

Raudkivi, A. J. 1990. *Loose boundary hydraulics*. 3rd ed. Oxford: Pergamon Press.

Rozovskii, I. L. 1957. *Flow of water in bends of open channels*. Translation by Y. Prushansky and S. Monson. Jerusalem, Israel: Israel Program for Scientific Translations.

Sheppard, D. M., M. Odeh, and T. Glasser. 2004. "Large scale clear-water pier scour experiments." *J. Hydraul. Eng.* 130 (10): 957–963. https://doi.org/10.1061/(ASCE)0733-9429(2004)130:10(957).

Sistema Cartografico Nacional. 2022. "PNOHISTORICAL 2004–2019." Accessed May 3, 2022. https://www.scne.es/productos.php#PNOAHISTORICO|2004-2019.

Vanoni, V. 1975. *Sedimentation engineering*. New York: ASCE.

Yang, Y., B. W. Melville, G. H. Macky, and A. Y. Shamseldin. 2019. "Local scour at complex bridge piers in close proximity under clear-water and live-bed flow regime." *Water* 11 (8): 1530. https://doi.org/10.3390/w11081530.

Yang, Y., B. W. Melville, D. M. Sheppard, and A. Y. Shamseldin. 2018. "Clear-water local scour at skewed complex bridge piers." *J. Hydraul. Eng.* 144 (6): 04018019. https://doi.org/10.1061/(ASCE)HY.1943-7900.0001458.

Numerical Analysis of the Ebro River Meander Flow Field, Upstream to the Pavilion-Bridge

César SANTOS[1], Cristina FAEL[2], Juan P. MARTIN-VIDE[3]

[1,2] Centre of Materials and Building Technologies (C-MADE), Universidade da Beira Interior, Portugal
email: a34474@ubi.pt
email: cmsf@ubi.pt

[3] Universitat Politècnica de Catalunya, Spain
email: juan.pedro.martin@upc.edu

ABSTRACT

Understanding the hydro-geomorphological processes of rivers has always been a central issue in river hydraulics researches. Not only is the comprehension of these mechanisms academically interesting, but it is also of great practical importance. It is widely known that rivers are dynamic systems and when exposed to natural dynamic hydrologic conditions, they readjust themselves with respect to dimension, profile and pattern to reach an equilibrium state, by an ongoing natural process of erosion and deposition. As for the river banks, it is known that they are subject to erosion, particularly in sharp-bend meanders, owing to the high bed shear stresses at the outer bank. These mechanisms lead to the formation of deposition and scour zones, which may negatively impact structures like bridge piers and abutments (Blanckaert et al., 2013). As a result, one of the most critical tasks in river engineering is the prediction of momentum and sediment transport in curved channels. In bends, the combination of centrifugal forces and pressure gradients results in transverse circulations. This three-dimensional helical flow plays an important influence on flow behaviour and river morphology (Blanckaert & de Vriend 2004; Khosronejad et al. 2007). Other parameters such as curvature ratio and aspect ratio significantly affect the hydrodynamics and morphodynamics of the meander, as they can influence the intensity of the transverse circulation cells (Kashyap et al., 2012).

1. Methodology

In the current work, the Ebro River, upstream to the Pavilion-Bridge, Zaragoza – Spain, meander flow field is numerically studied, with particular interest in the maximum flow rate (2500 $m^3\ s^{-1}$), which is the most unfavourable condition in terms of erosion. In this circumstance, the hydraulic diameter and the mean velocity at the inlet section are 15.7 m and 2.54 m s^{-1}, respectively, which corresponds to a Reynolds number, Re, $\approx 4.5 \times 10^7$ and a Froude number of 0.2. The river section under study is ≈ 5100 m in length, with an average of 250 m of width and a water depth at the thalweg ranging from 9 m at the inlet to 8 m at the outlet. The topographic data (1-meter contours) was analysed in AutoCAD and subsequently transferred to the meshing software, in this case, Pointwise. Particular attention was paid to the mesh generation process, as parameters such as centroid skewness, volume skewness and aspect ratio of the cells are imperative for the quality of the mesh and, consequently, the quality of the results obtained. Also, it is worth mentioning that, owing to the extreme complexity of the meander geometry, the only possible mesh generation was an unstructured one, with tetrahedral elements. This process yielded a mesh with approximately 2.5 million cells. The mesh was then transferred to ANSYS Fluent that recurs to the finite volume method to solve the incompressible continuity and momentum (Euler) equations, simultaneously, which in a Cartesian tensor form are written, respectively, as:

$$\frac{\partial u_i}{\partial x_i} = 0 \tag{1}$$

and

$$\frac{\partial u_i\, u_j}{\partial x_j} = -\frac{1}{\rho}\frac{\partial p}{\partial x_i} + g \tag{2}$$

where u, p, x, ρ and g are, respectively, velocity vector, static pressure, spatial coordinates, fluid density and gravitational acceleration vector. Given the Reynolds number, it is not unreasonable to assume an inviscid

solution, seeing that the $(1/Re)\nabla \vec{\tau}$ term of the non-dimensionalized Navier-Stokes equation tends to zero when the Reynolds number is drawn to very high values (White, 2003; Bird et al., 2002). As for the solution methods, the gradients were estimated using Least Squares Cell-Based scheme and the pressure interpolation, recurring to the Second Order method. The momentum was estimated using the Second Order Upwind and the transient formulation recurred to the First Order Implicit.

2. Results

The preliminary results obtained, from a computation of 3600 timesteps of 1 second each, are in concurrence with the ones obtained in Blanckaert & de Vriend (2004) and Khosronejad et al. (2007), as pressure gradients can be observed in Fig. 1 (right), higher on the outer bank and lower on the inner bank, which results in transverse circulations. Also, Fig. 1 (left) shows a high velocity zone at the outer bank (1), which can significantly influence bank and bed erosion, since at these locations higher shear stresses are present due to high transverse velocity gradients. One could expect that this zone would occur at around 50% of the computational domain or even prior, but, owing to the large width and curvature ratio of the meander, this zone is shifted downstream, since fluid particles take longer to reach the outer bank. Of particularly great interest is the constriction zone (2) seen in Fig. 1. As expected, it is a high velocity zone and, as the section expands again, there are two stagnation zones, but another one can also be detected upstream to the constraint, being the latter a more stable circulation zone. At the downstream side, low pressure cores (3) can be seen in Fig. 1 (right), which coincides with the vortices observed at said location. These stagnation zones are highly prone to sediment deposition. At the beginning of the right-hand curve (3), owing to the high velocity that precedes it, a separation zone is formed, which is also a zone prone to sediment deposition. Given that an inviscid approach was assumed, it is expected that the real velocity values are slightly lower than the ones obtained. Nonetheless they are reliable and useful in predicting the flow behaviour, especially in cases of Reynolds number of such a high order. Also, it is worth mentioning that the present results focus on the mean flow properties, since these are preponderant to characterize the mechanisms of erosion. As previously stated, the computation was carried out over 1 hour (flowtime), since it was the duration required to capture the periodic phenomena occurring during the simulation and, therefore, to obtain an accurate mean estimation of the flow parameters.

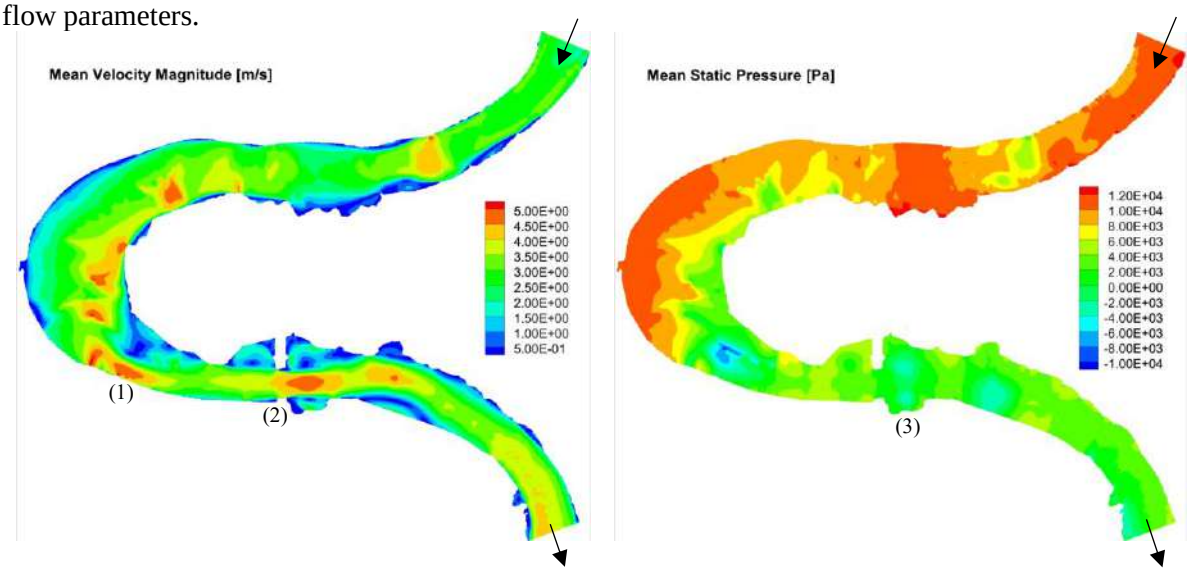

Fig. 1. Mean velocity magnitude (left) and mean relative static pressure (right) contours at the river bed.

Acknowledgements

This work was supported with Portuguese national funds by FCT - Foundation for Science and Technology within the UID/ECI/04082/2013 project.

References

Bird RB, Stewart WE, Lightfoot EN (2002) Transport Phenomena, J. Wiley, 126 pp.
Blanckaert K, Constantinescu G (2013) Hydro- and morphodynamics in curved river reaches – recent results and directions for future research, Advances in Geosciences, 37, 19-25.
Blanckaert K, de Vriend H (2004) Secondary flow in sharp open-channel bends, Journal of fluid mechanics, 498, 353-380.
Kashyap S, Constantinescu G, Rennie C, Post G, Townsend R (2012) Influence of channel aspect ratio and curvature on flow, secondary circulation, and bed shear stress in a rectangular channel bend, Journal of Hydraulic Engineering, 128, 1045-1059.
Khosronejad A, Rennie C, Salehi Neyshabouri SAA, Townsend R (2007) 3d numerical modelling of flow and sediment transport in laboratory channel bends, Journal of Hydraulic Engineering-asce – Journal of Hydraulic Engineering-ASCE, 133, 1123-1134.
White FM (2003) Fluid Mechanics, McGraw-Hill, 555 pp.